5-2014

Structural analysis of the Tablerock thrust sheet, Grandfather Mountain window, northwestern North Carolina: Emplacement kinematics of a large horse in a major thrust system

Ann Elizabeth Walker
University of Tennessee - Knoxville, walkerae@utk.edu

To the Graduate Council:

I am submitting herewith a thesis written by Ann Elizabeth Walker entitled "Structural analysis of the Tablerock thrust sheet, Grandfather Mountain window, northwestern North Carolina: Emplacement kinematics of a large horse in a major thrust system." I have examined the final electronic copy of this thesis for form and content and recommend that it be accepted in partial fulfillment of the requirements for the degree of Master of Science, with a major in Geology.

Robert D. Hatcher Jr., Major Professor

We have read this thesis and recommend its acceptance:

Christopher M. Fedo, Micah J. Jessup

Accepted for the Council:
Carolyn R. Hodges

Vice Provost and Dean of the Graduate School

(Original signatures are on file with official student records.)

Structural analysis of the Tablerock thrust sheet, Grandfather Mountain window, northwestern North Carolina: Emplacement kinematics of a large horse in a major thrust system

A Thesis Presented for the

Master of Science

Degree

The University of Tennessee, Knoxville

Ann Elizabeth Walker

May 2014

This work is dedicated to Dr. Lawrence H. Tanner, Dr. David L. Smith, and Jessica L. Curry.
For your mentorship, Íslenskir hestar, and reminding me who I am.

To my husband, Dan—for *makoto no kokoro*.
Because others see a rock, a rope, and another rock,
but really there is only *tama*.

And to the memory of my dear friend, H.P.
who watched over me through it all.

ACKNOWLEDGEMENTS

This research was supported by funding from the Department of Earth and Planetary Sciences, the Science Alliance Center of Excellence, the Structural Geology and Tectonics Research Group, and the Geological Society of America. Invaluable technical and administrative support was provided by Melody Branch, Nancy Meadows, Teresa Parrott, Angie Staley, Sarah Stone, and Andrew Wunderlich. Instructive comments and reviews from my thesis committee—Dr. Robert D. Hatcher, Jr., Dr. Christopher M. Fedo, and Dr. Micah J. Jessup—were integral in the development, evolution, and completion of this work, and their contributions have been greatly appreciated. Mr. Jack Boone, Explosive Supply Co. (Woodlawn quarry); Mike, Appalachian Stone Co.; and Mr. Tom Andrews, Blue Ridge Quarries, Inc. generously provided me with access to the spectacular structures exposed in their quarries. Dr. Charles Trupe, Georgia Southern University; Dr. Whitney Behr, University of Texas–Austin; Mr. Jeff Bailey, Tengasco, Inc.; and Dr. Brian Horn, ION Geophysical were equally as generous in sharing their expertise, experience, advice, and opportunities.

Many thanks to the Grandfather Mountain District Rangers; National Park Service campground at Linville Falls; and Mike, Lynn, and Blue Thrift of the Skyline Village Inn & Cavern Tavern—for extra firewood when it snowed; a refuge from the hot Carolina rainy season; and pancakes for breakfast.

Thanks also to my fellow graduate students—especially Mary Biswal, Latisha Brengman, Arya Udry, Kathleen Warrell, and all of my comrades in structure, tectonics, and weekend field trips. To Katherine McDonough; Jim and Lindsay McDonough; Ms. Teenie Hayworth; Michele and Gary Genova, and everyone at Karns Elementary; Brandon and Carolyn West; Jake Morrow; and Andrew Wunderlich—for open-heartedly folding us into your lives, families, homes, opera outings, bon fires, and Friday nights. We miss you. And to new friends, Mumu Dee, Gülçe Dinç, Antara Goswami, and Maggie Pueringer—who instantly made Houston the best place around. Very special thanks to Dr. Sally Horn and Dr. Kula Misra, whose support and encouragement meant more than they probably know. And to Dr. Robert Hatcher, who gave me a shelter that became a home.

Finally, to my best friend, Jess Holzer; my sisters, parents, and family; Mark and Mary Cay Phelps; Aunt Sandra and Uncle Milt; Aunt Lois and Uncle Joe; Joe Holzer and Lynne Odell-Holzer; my very patient friends, Geoff Piper and Jason Sack; Dr. Douglas E. Wojcik and everyone at LVAH; and to the memory of my grandfather, Harry C. Terry—Thank you for visiting when I was too busy and penniless, for putting up with my long absences, and for your encouragement through the years. You are the examples by which I live, and this endeavor belongs to each of you.

ABSTRACT

The Tablerock thrust sheet is exposed along the southwestern margin of Grandfather Mountain window in northwestern North Carolina, where it separates basement and cover rocks inside the window from basement thrust sheets of the overriding Blue Ridge-Piedmont megathrust sheet. It is a complex of footwall-derived horses of rifted-margin metasedimentary rocks, including Neoproterozoic to Early Cambrian Chilhowee Group quartzite and phyllite, and Shady Dolomite. Penetrative deformation throughout the Tablerock thrust sheet is defined by an extensively transposed foliation, and strong colinearity between well developed transport lineations and SE/NW-trending tight, isoclinal, and sheath folds. Centimeter- to meter-scale sheath folds are common throughout the interior of the thrust sheet, and not just within fault zones. NE-trending/NW-vergent crenulations and mesoscale open folds overprint these fabric elements, and represent one to two later phases of deformation. The strong colinearity between transport lineations and the hinges of tight to isoclinal folds, prevalence of mesoscale sheath folds, and outcrop patterns on Bryant and Reed's 1970 map suggest SE/NW-trending megascopic folds at Linville Falls waterfall, Woodlawn quarry, and in the Linville Gorge Wilderness Area are map-scale sheath folds. Deformation temperatures estimated from metamorphic mineral assemblages, quartz lattice-preferred orientations, dynamic recrystallization microstructures, feldspar deformation microstructures, and the opening angles of quartz [c]-axis fabrics indicate the Tablerock thrust sheet reached 550–595 °C during lower–middle amphibolite facies conditions, and was later overprinted by upper greenschist to lower amphibolite facies conditions at 465–550 °C. These estimates are at least 120 °C higher than all previously reported temperatures, and are consistent with a model in which the Tablerock thrust sheet was significantly deformed during coupled transport with the Blue Ridge-Piedmont megathrust sheet prior to being emplaced at its present location.

TABLE OF CONTENTS

LIST OF TABLES

LIST OF FIGURES

LIST OF SYMBOLS

[0001]	Crystallographic direction of [c]-axes (i.e. pole to the (0001) basal plane)
$<10\bar{1}0>$	Crystallographic directions parallel to the poles to $\{10\bar{1}0\}$ hexagonal prisms
$<11\bar{2}0>$	Crystallographic directions parallel to $\{11\bar{2}0\}$ rhomb prisms
<a>	Crystallographic directions parallel to the [a]-axes
β	Acute angle between the dominant foliation and the shear (flow) plane
[c]	Crystallographic [c]-axis; pole to the (0001) basal plane
δ	Angle between the dominant foliation and the S_2 oblique grain-shape foliation
ė	Strain rate
X°	Angular displacement, degree units
°C	Degrees Celsius
F_1	D_1 mesoscale folds
F_2	D_2 mesoscale folds
F_3	D_3 mesoscale folds
L_1	D_1 mineral lineations
Lc	Trend of crenulation hinge lines
S_0	D_0 macroscopic foliation *(original bedding)*
S_1	D_1 macroscopic foliation
S_2	D_{1-2} microscopic foliation *(oblique grain-shape foliations)*

LIST OF ABBREVIATIONS

ap_1	Extensional flow apophysis (i.e. the shear or flow plane)
BLG	Bulging recrystallization
Bt	Biotite
Chl	Chlorite
DRX	Dynamic recrystallization
EBSD	Electron backscatter diffraction
E-SEM	Environmental scanning electron microscope
Ga	Giga-annum *("billion years before present")*
GBR	Grain boundary migration recrystallization
γGBM	Surface energy-driven grain boundary migration
ρGBM	Strain energy-driven grain boundary migration
GMF	Grandfather Mountain Formation
GMW	Grandfather Mountain window
Kfs	K-feldspar
kv	Kilovolt
LPO	Lattice-preferred orientation
Ma	Mega-annum *("million years before present")*
Msc	Muscovite
m.u.d.	Multiples of uniform distribution
o.a.	Opening angle
qtz	Quartz
rxtlz'd	Recrystallized
SGR	Subgrain rotation recrystallization
Sil	Sillimanite
TR	Tablerock
xtlz'd	Crystallized

CHAPTER 1 | INTRODUCTION

Transport-parallel mineral and stretching lineations are often coaxial with the trends of tight and isoclinal folds in high-strain, orogenic shear zones, and other settings characterized by heterogeneous deformation—including glaciers and sub-glacial sediments, volcanic flows, migrating salt, and sediment slumps (Bryant & Reed 1969; Escher & Watterson 1974; Nicolas 1987; Alsop 1992; Alsop & Holdsworth 2004a; Carreras et al. 2005; Cook et al. 2011; Morales et al. 2011). Natural and experimental studies (e.g. Bryant & Reed 1969; Escher & Watterson 1974; Alsop 1992; Mies 1993; Jiang & Williams 1999; Rosas et al. 2002; Alsop & Holdsworth 2004a, b; Carreras et al. 2005; Alsop & Carreras 2007; Kuiper et al. 2007; Xypolias 2010; Morales et al. 2011; Reber et al. 2013a; and others) suggested this alignment is most often produced by progressive, non-coaxial deformation, during which objects or surfaces oriented at high angles to the shear regime rotate towards the extensional apophysis of the flow (i.e. the shear plane of finite strain). Mesoscale sheath folds are also common in shear zones, and most models for their formation invoke similar mechanisms of rotation and amplification. In the Tablerock thrust sheet, exposed inside the Grandfather Mountain window of the southern Appalachian Blue Ridge, strong colinearity between well-developed transport lineations, SE/NW-trending tight to isoclinal folds (e.g. Bryant & Reed 1969, 1970; Boyer 1978; Trupe 1997; Walker & Hatcher 2012a), and mesoscale sheath folds (e.g. Walker & Hatcher 2012b) indicates at least part of the thrust sheet's deformation history was dominated by non-coaxial simple shear. However, previous studies of the Grandfather Mountain window and related Blue Ridge faults and thrust sheets (e.g. Bryant & Reed 1969, 1970; Butler 1973; Schwab 1977; Boyer 1978; D'Agostino et al. 1983; Boyer 1984; Fetter & Goldberg 1995; Adams & Su 1996; Trupe 1997; Trupe et al. 2004; and others) have not attempted to characterize the internal structure of the Tablerock thrust sheet; thus the mechanism(s) responsible for the NW-alignment of transport lineations and tight to isoclinal fold hinges remains enigmatic (Walker & Hatcher 2012a).

Recognizing the key role of non-coaxial deformation in both the development of sheath folds and lineation-parallel fold hinges, Hatcher et al. (2006) suggested kilometer-scale NW-trending tight folds near Linville Falls waterfall could be parasitic folds on map-scale sheath folds in the Tablerock thrust

sheet. Kilometer-scale fold-like structures with apparently SE/NW trends are also visible in satellite images of the eastern rim of Linville Gorge, and of the northeast part of the thrust sheet, near Jonas Ridge. If these structures are megascopic NW-trending folds, both they, and outcrop patterns mapped by Bryant and Reed (1970), may also be consistent with map-scale sheath folds (Walker & Hatcher 2012b). Type-F (fold-related) thrust sheets (e.g. Hatcher & Hooper 1992) and fold-nappes form megascopic sheath folds in the basal regions of many large thrust sheets, including those of the Cabo Ortegal complex, northwest Spain; Tambo nappe, central Swiss Alps; Dumbara syncline, Sri Lanka; and the Shimanto accretionary complex, Japan (Azcárrga et al. 2002, and references therein; Searle & Alsop 2007). Mesoscale sheath folds have been used to identify the existence and geometry of map-scale sheath folds in sparsely exposed parts of the Scottish and Norwegian Caledonides (Vollmer 1988; Alsop & Holdsworth 1999), the Strangeways orogen in central Australia (Goscombe 1991), and the Hercynian allochthons of the Iberian Peninsula (Azcárrga et al. 2002). If the Tablerock thrust sheet contains kilometer-scale sheath folds, the parallel alignment of SE/NW-trending tight to isoclinal folds, mesoscale sheath folds, and transport lineations could have developed during nappe-like emplacement along the base of the Blue Ridge-Piedmont megathrust sheet.

This study is an attempt to characterize the internal structure of the Tablerock thrust sheet and develop a kinematic model for the generation of lineation-parallel tight, isoclinal, and sheath folds using detailed field measurements and microstructural analysis.

1.1 Study area

The Tablerock thrust sheet is exposed along the southwestern margin of the Grandfather Mountain window in northwestern North Carolina, where it structurally separates basement and cover rocks inside the window from the basement thrust sheets and Tugaloo terrane of the overriding Blue Ridge-Piedmont crystalline megathrust sheet (Bryant & Reed 1970; Boyer 1978; Goldberg et al. 1986; Hatcher et al. 2007a). It is a footwall-derived horse containing rifted-margin metasedimentary rocks, including Neoproterozoic (?) to Early Cambrian Chilhowee Group quartzite and phyllite, and Shady Dolomite, and is the highest thrust-imbricate in the now unroofed antiformal stack duplex of the window (Bryant & Reed

1969, 1970; Boyer 1978). The Tablerock sheet is overlain by a kilometer-thick ductile shear zone that defines the base of the Blue Ridge-Piedmont megathrust sheet (the Linville Falls shear zone of Trupe 1997), and is locally overlain by horses of crystalline rock derived from the base of the Blue Ridge-Piedmont sheet. Penetrative deformation within the Tablerock sheet is defined by prominent, NW-trending mineral and stretching lineations, NE-trending/NW-vergent crenulations, and two mesoscale fold populations—one trending NE with close to open interlimb angles, the other trending NW with tight to isoclinal interlimb angles (Bryant & Reed 1969, 1970).

The Tablerock thrust sheet is comprised in ascending order of the lower quartzite unit, blue phyllite unit, upper quartzite unit, and Shady Dolomite; it extends north-northeast from Marion to Crossnore, NC, and crosses parts of the Ashford, Linville Falls, Little Switzerland, Marion West, Newland, and Oak Hill 7.5‘ quadrangles (Fig. 1.1). Land associated with the Tablerock thrust sheet is located within the North Carolina Pisgah National Forest (administered by the U.S. Forest Service), and crosses parts of the Blue Ridge Parkway (National Park Service), Linville Gorge Wilderness Area (U.S. Forest Service), and Southern Region (R-8) of the Grandfather Ranger District (U.S. Forest Service). Significant acreage in each of these jurisdictions is privately owned, including land crossing, or adjacent to official U.S. Forest Service and National Park Service trails, overlooks, and attractions.

Chilhowee Group rocks are well-exposed in roadcuts along US-221 between Marion and the community of Linville Falls, as well as in roadcuts along the Blue Ridge Parkway entrance to the Linville Falls parking area, in outcrops at National Park Service Upper Falls overlook (including the Linville Falls fault type locality), in several small klippen on and near Tablerock Mountain, and along the walls of Linville Gorge; Shady Dolomite is exposed in the Woodlawn quarry (Explosive Supply Co.), near Marion, NC, and in several small outcrops along state route NC-183 (Wilkins 1966; Bryant & Reed 1970; Byrd 1973; Boyer 1978; Trupe 1997; Walker & Hatcher 2012a). Structural data were collected at 123 field stations from March–August 2012; mesoscopic structures and fabric elements were measured with a Brunton™ pocket transit compass, and recorded on a Trimble GeoExplorer® Series GPS unit using ESRI ArcPad™ software. Stereographic fabric diagrams were created using OSXStereonet 2.2 (© Cardozo & Allmendinger 2012). Field maps were digitally compiled using ESRI ArcGIS® 10.2 and edited with Adobe

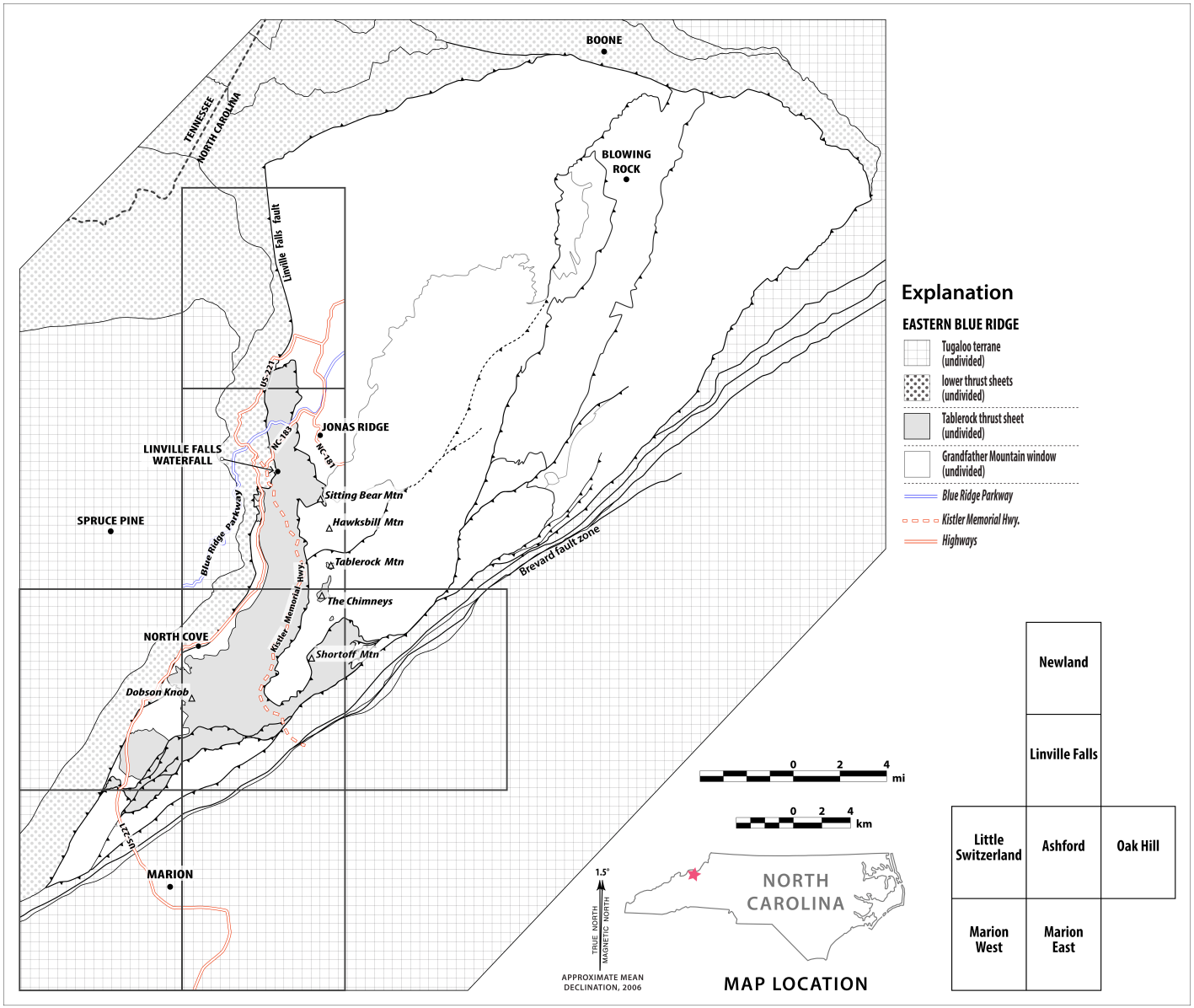

Figure 1.1: Index map of the Tablerock thrust sheet within Grandfather Mountain window. Rectangles represent the locations of 7.5' U.S. Geological Survey quadrangles. The star on the inset map of North Carolina indicates the location of the Grandfather Mountain window. After Bryant & Reed (1970).

Illustrator® CS6; all figures were also produced using Adobe Illustrator® CS6. Field samples were collected in accordance with National Park Service permit BLRI-2011-SCI-0027.

1.2 Mechanics of sheath fold formation

Sheath folds are highly non-cylindrical to conic structures that extend subparallel to the X-axis of finite strain, and have hinge lines that curve about an apex that opens < 90° (Fig. 1.2) (Skjernaa 1989; Alsop & Holdsworth 1999; Alsop & Carreras 2007; Marques et al. 2008; Reber et al. 2012). They occur most often in high-strain crustal and glacial shear zones, and during heterogeneous deformation associated with diapirism, salt migration, sediment slumping, and magmatic flows (Alsop & Holdsworth 2002; Alsop & Holdsworth 2004a; Cook et al. 2011). Natural and experimental studies suggest sheath folds form by passive amplification of pre-existing structures in pure shear, simple shear, and transpressional regimes (e.g. Cobbold & Quinquis 1980; Skjernaa 1989; Alsop 1992; Alsop & Holdsworth 2006; Mandal et al. 2009), and actively nucleate around perturbations in non-coaxial flow (e.g. Cobbold & Quinquis 1980; Marques & Cobbold 1995; Rosas et al. 2002; Exner & Dabrowski 2010; Reber et al. 2012; Reber et al. 2013a, b) (Table 1.1).

During simple shear deformation, buckling accommodates layer-parallel shortening until the inner arcs of fold hinge zones reach a critical tightness, after which strain accumulates by shear-related flattening (Carreras et al. 2005). The progressive, heterogeneous flow associated with simple shear rotates pre-existing (or recently formed) structures toward the X-direction of finite strain, promoting en echelon buckling and the development of curvilinear fold hinges (Fig. 1.3) (Alsop & Holdsworth 2004a; Alsop & Carreras 2007). With continued deformation, discrete return hinges may form between the

Table 1.1: Summarized mechanisms of sheath fold formation.

	SIMPLE SHEAR	PURE SHEAR	TRANSPRESSION
PASSIVE FORMATION	- Rotation and amplification of pre-existing structures.	- Flattening and amplification of pre-existing curvilinear folds.	- Constriction and amplification of pre-existing curvilinear folds.
ACTIVE FORMATION	- Nucleation and amplification; - Flow perturbations.	- Does not occur.	- Does not occur.

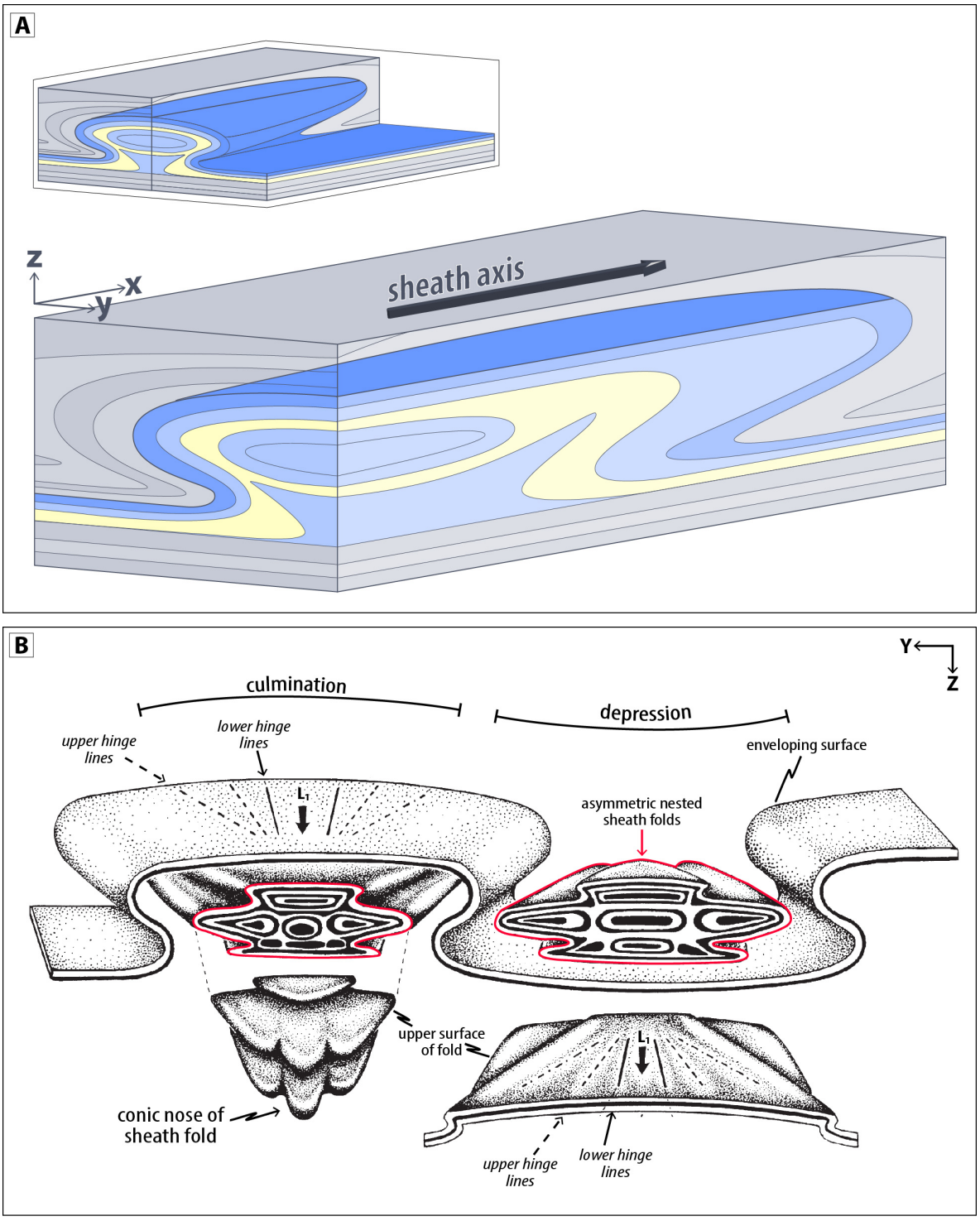

Figure 1.2: Schematic cross sections through the upper limb of an idealized sheath fold. Coordinate axes (x, y, z) are the principal directions of finite strain. Diagram (B) is after Alsop and Holdsworth (2004). (A) In general, the long axes of sheath folds approach the X-axis of finite strain. Notice that hinges of the outermost enveloping layers (grey) are more open than are hinges of internal layers. Inset diagram (upper left) shows the complete cone and its characteristic anvil-shaped cross section. (B) Internal structures and geometric relationships of sheath folds. Secondary culminations and depressions ("culmination/depression surfaces" of Alsop & Holdsworth 2004) envelope sheath folds. Strain gradients around culminations/depressions cause hinge lines to verge toward L_1, which produces asymmetric, nested clusters of sheath folds ("asymmetric tear-drop" folds of Alsop & Holdsworth 2004) in/near nose cones (e.g. Alsop & Holdsworth 2004).

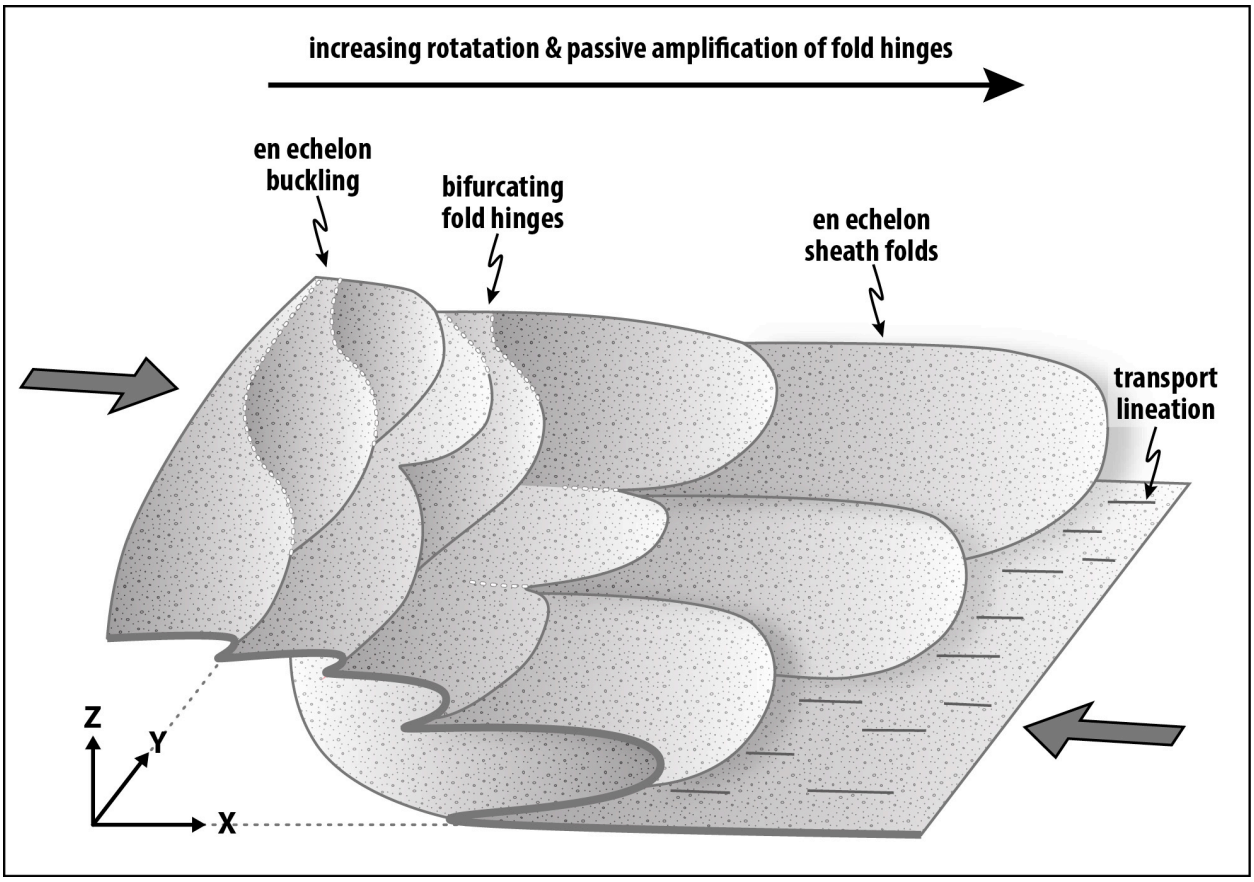

Figure 1.3: Sheath fold evolution during passive amplification. Coordinate axes (x, y, z) are the principal directions of finite strain; large arrows indicate bulk top-right shear. Progressive, non-coaxial deformation rotates pre-existing asperities toward the X-direction of finite strain, promoting the formation of curvilinear folds through en echelon buckling, followed by hinge bifurcation, and finally sheath folding. Note that en echelon sheath folds appear to verge toward the Y-direction of finite strain (into the page) as well as toward the shear direction. After Alsop and Carreras (2007).

overlapping echelon units (i.e. hinge bifurcation), while the curved hinge zones amplify to sheath fold geometries (Alsop & Holdsworth 2004a; Alsop & Carreras 2007). Buckle folds that nucleate at high angles to the shear plane develop highly thinned common limbs as their hinges rotate toward the extensional apophysis (ap_1) of the flow, while the limbs of buckle folds at low angles to the shear plane tend to thin or thicken subequally (Carreras et al. 2005; Alsop & Carreras 2007; Kuiper et al. 2007; Xypolias 2010; Morales et al. 2011; Reber et al. 2013a).

Turbulent flow around rigid inclusions and rheologically weak surfaces during bulk simple shear promotes the nucleation and amplification of sheath folds at the low-velocity tips of boudins, porphyroclasts, cracks, veins, faults, and other structural asperities (Cobbold & Quinquis 1980; Marques & Cobbold 1995; Rosas et al. 2002; Exner & Dabrowski 2010; Reber et al. 2012; Reber et al. 2013a, b).

Like flanking structures, sheath folds formed around rigid inclusions are mechanically passive features controlled primarily by prevailing strain levels (e.g. Cobbold & Quinquis 1980; Marques & Cobbold 1995; Rosas et al. 2002; Exner & Dabrowski 2010). Recent studies by Reber et al. (2012) and Reber et al. (2013a, b) demonstrate that sheath folds also form around rheologically weak surfaces or inclusions in mechanically layered materials, and therefore are not always purely passive structures.

Sheath folds may also form when pre-existing curvilinear folds are modified by constriction during transpression (e.g. Bailey et al. 2004), or constriction and flattening associated with pure shear (e.g. Ez 2000; Mandal et al. 2009). The occurrence of L and L>S tectonites, or the accommodation of more shortening in the Z direction than in the Y direction of finite strain suggest a given deformation included a constrictional component (Nicolas 1987; Azcárraga et al. 2002; Alsop & Holdsworth 2006; Alsop et al. 2007; Sullivan 2013). In folded rocks, L tectonites tend to localize within hinge zones, while L>S and L-S tectonites form in the limbs (Sullivan 2013). However, because most experimental constriction models produce dome-and-basin structures that do not develop into sheath folds with continued shortening, a robust parameter for the contribution of constriction during shear deformation and the formation of sheath folds has yet to be developed (Alsop & Holdsworth 2006). While bulk deformation may include pure shear or transpressional components, or localized zones of constriction and flattening, detailed studies by Alsop and Holdsworth (2006) and Alsop et al. (2007) indicate 98% of natural sheath folds formed during bulk simple shear or general shear deformation.

CHAPTER 2 | GEOLOGIC CONTEXT

2.1 Nomenclature

The Tablerock fault was named for its type locality at the Tablerock Mountain klippe (elevation 1122 m), just southeast of Hawksbill Mountain in the Linville Gorge Wilderness Area (Fig. 1.1). Some workers (e.g. Bryant & Reed 1962; Hatcher et al. 2006; and others) have used "Tablerock" and "Table Rock" interchangeably in past literature; the correct, compounded nomenclature should be used to eliminate confusion between the Tablerock thrust fault, sheet, and klippe, and the Table Rock Mountain (elevation 1219 m) located just across Linville Gorge at the junction of Avery, Mitchell, and McDowell Counties (northwest of Blue Ridge Parkway milepost 324).

2.2 Regional geologic setting

The Blue Ridge-Piedmont megathrust sheet in the central and southern Appalachians is one of the largest and best-preserved overthrust crystalline terranes currently known from collisional orogens world-wide. It contains 1.0–1.2 Ga basement gneisses overlain by syn- to post-rift clastic rocks of the Laurentian proximal rifted margin (i.e the western Blue Ridge), and the Neoproterozoic to Early Ordovician distal margin clastic and volcanoclastic rocks of the western Tugaloo terrane that accreted during the Taconic event (Hatcher 2010). Thick, ductile Alleghanian shear zones divide the Blue Ridge-Piedmont sheet internally into a series of secondary thrust sheets, including the Fries, Fork Ridge, and Linville Falls (Beech Mountain) thrust sheets (Bailey et al. 2004; Trupe et al. 2004; Hatcher et al. 2006).

During the final assembly of Pangea, the Blue Ridge-Piedmont megathrust sheet detached along a brittle-ductile transition localized in Grenvillian basement rocks, and was thrust more than 300 km northwest over the Laurentian margin (Hatcher & Hooper 1992; Hatcher et al. 2007a, 2007b). The last stage of this movement was accommodated by subthrust duplexing in sedimentary platform rocks of the footwall, and produced antiformal stack duplexes that domed the overriding crystalline terrane (Boyer 1978; Hatcher 1991; Hatcher 2004a). The Grandfather Mountain window, adjacent Mountain City and

Limestone Cove windows, and nearby Hot Springs and Sauratown Mountains windows are the unroofed sections of antiformal stack duplexes beneath domes breached by erosion (Fig. 2.1).

The Grandfather Mountain window is the largest window through the Blue Ridge-Piedmont sheet, and one of the largest in North America; it is situated just east of the Tennessee–North Carolina border in northwestern North Carolina, where it occupies approximately 1200 km^2 of Blue Ridge terrane in the southern Appalachian orogen (Fig. 2.2). Boyer (1978) interpreted that imbricate thrusts inside the window sole into the master detachment along which the Blue Ridge-Piedmont megathrust sheet was transported. Within the study area, the base of the Blue Ridge-Piedmont sheet is defined by the Linville Falls shear zone (i.e. the Linville Falls fault, *sensu lato*), which frames the window and is believed to rejoin the master detachment to the northwest (Fig. 2.2; Fig. 2.3).

2.3 General geology of the Grandfather Mountain window

Inside the Grandfather Mountain window 5–9 km of rift-related sedimentary and volcanoclastic rocks of the Grandfather Mountain Formation nonconformably overlie 1.15 Ga Blowing Rock and Wilson Creek basement gneisses and 0.76 Ga Brown Mountain Granite (Boyer 1978; Neton 1992; Fetter & Goldberg 1995). The Grandfather Mountain Formation, along with the correlative Mount Rogers Formation of southern Virginia and northeastern Tennessee, and the Beech Granite and Bakersville Gabbro of the Crossnore plutonic suite were produced by an early, incomplete phase of intracratonic rifting of Rodinia ~735 Ma (Hatcher 1978; Neton 1992; Aleinikoff et al. 1995; Fetter & Goldberg 1995; Hatcher et al. 2007a). Rocks of the Grandfather Mountain Formation contain interlayered beds and lenses of feldspathic quartzite, metasiltstone, and metagraywacke; pebble and cobble conglomerate; mafic and felsic tuffs; rhyolite flows; and metamorphosed basalt (Montezuma Member) (Schwab 1977). Ripple marks, filled channels, and poor sediment sorting indicate the clastic units were deposited in a fluvio-deltaic environment, while abrupt changes in thickness and rock type along strike suggest the basin subsided rapidly during deposition (Bryant & Reed 1970; Schwab 1977). The complex and laterally discontinuous stratigraphy throughout most of the Grandfather Mountain Formation is consistent with these depositional conditions.

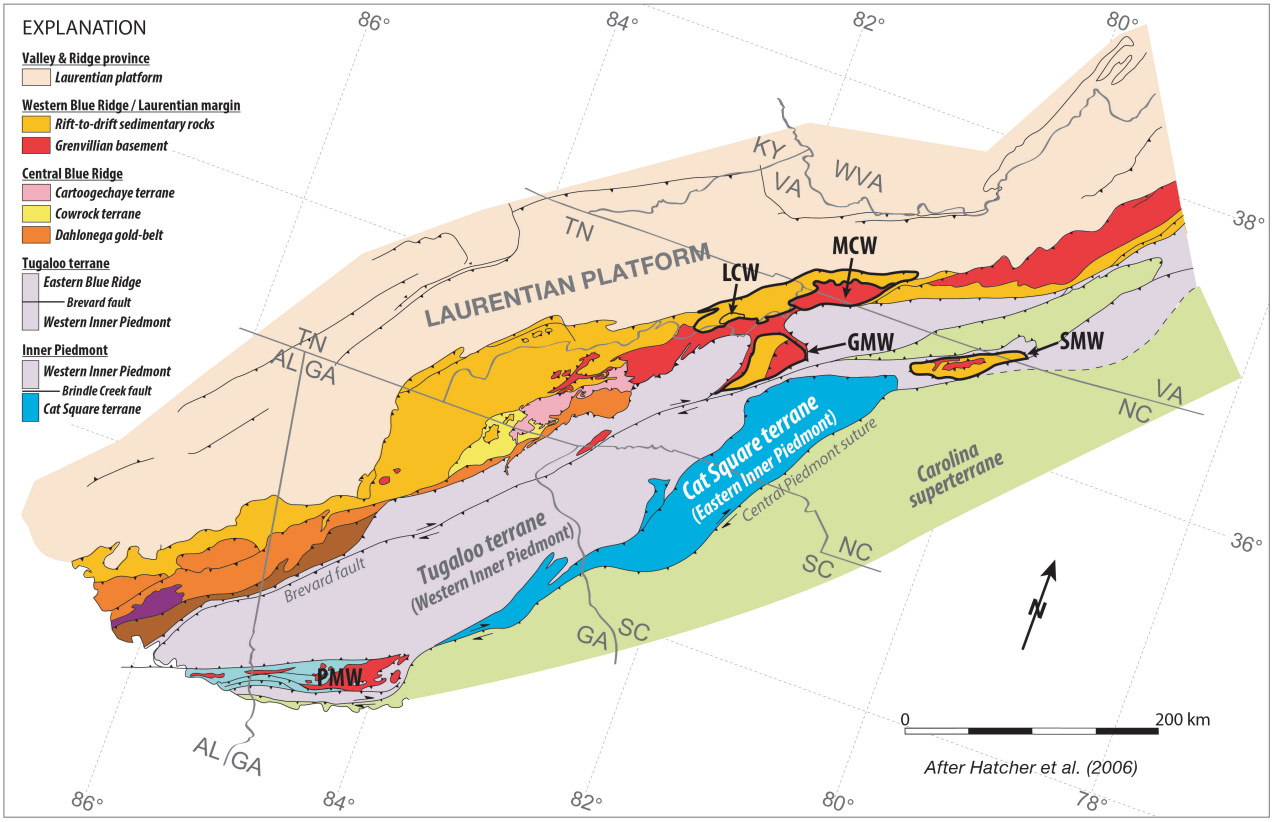

Figure 2.1: Major tectonic elements of the southern Appalachian orogen. The southern and central Appalachian orogen is defined by a series of tectonostratigraphic terranes, including the Carolina superterrane, Cat Square terrane (blue), Tugaloo terrane, and Western Blue Ridge province (Laurentian margin). Thick outlines highlight major windows, including the Grandfather Mountain window (GMW), Limestone Cove window (LCW), Mountain City window (MCW), Pine Mountain window (PMW), and Sauratown Mountains window (SMW). After Hatcher et al. (2006).

The majority of Grandfather Mountain Formation rocks are exposed in the northern part of the window, where they form part of a complex syncline overturned to the northwest (e.g. Bryant & Reed 1969; 1970), and are truncated by the Linville Falls and Tablerock faults above (Fig. 2.3). The syncline is overprinted by a later generation of NE-trending open, tight, and isoclinal mesoscale folds, and the pervasive SE-dipping foliation also present in the Blowing Rock and Wilson Creek Gneisses. All NE-trending fabrics, including several secondary faults, are truncated by the Linville Falls and Tablerock faults along the northern frame of the window and eastern edge of the Tablerock thrust sheet (Bryant & Reed 1970; Walker & Hatcher 2012b).

Both the Linville Falls and Tablerock faults are thick, ductile shear zones defined respectively by ~8.0 km and ~2.5 km of greenschist-grade mylonite (Trupe 1997). The Linville Falls shear zone contains small

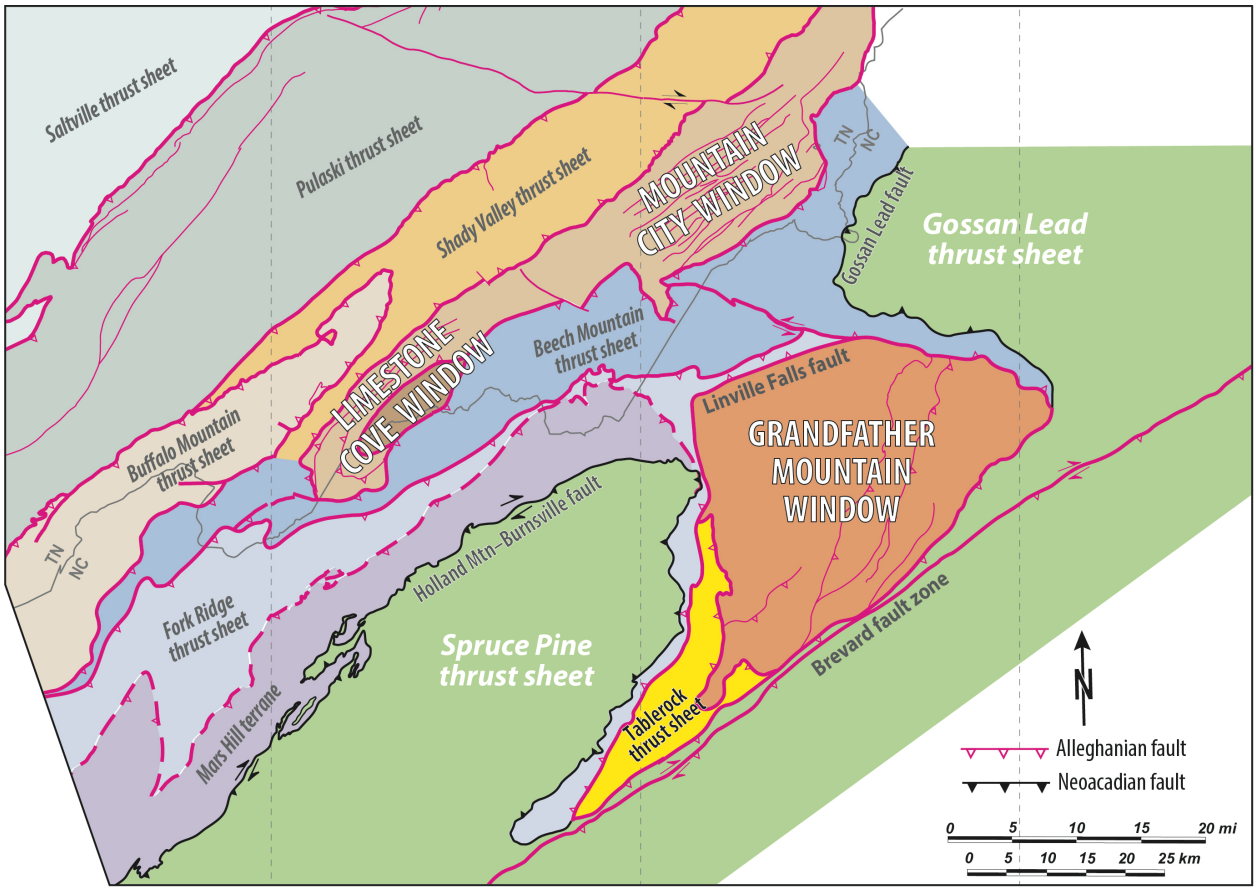

Figure 2.2: Major structural elements of the Grandfather Mountain window. Simplified tectonic map of the Grandfather Mountain window and vicinity. At this latitude the Blue Ridge-Piedmont megathrust sheet contains the Tugaloo terrane (Spruce Pine and Gossan Lead thrust sheets) and the Fork Ridge, Beech Mountain, Buffalo Mountain, and Shady Valley thrust sheets; the Saltville and Pulaski thrust sheets belong to the Valley and Ridge physiographic province. After Hatcher et al. (2006).

horses of crystalline rock derived from the base of the Blue Ridge-Piedmont megathrust sheet, including the block of Linville Falls granite overlying ~40 cm of ultramylonite at the Linville Falls type locality (Upper Falls overlook, Blue Ridge Parkway). Bryant and Reed (1970) originally mapped this unit as "Cranberry Gneiss" and placed it in the hanging wall, but later mapping by Trupe (1997) revealed the block pinches out ~0.5 km south and ~1.0 km north of the type locality, and is overlain by more than 7 km of shear zone mylonite. The tops and bases of both the Tablerock thrust sheet and the aforementioned horse of Linville Falls granite are strongly sheared by the bounding fault zones; however, only the Linville Falls shear zone contains a late cataclastic overprint in the lowermost meter of basal mylonite (Trupe 1997).

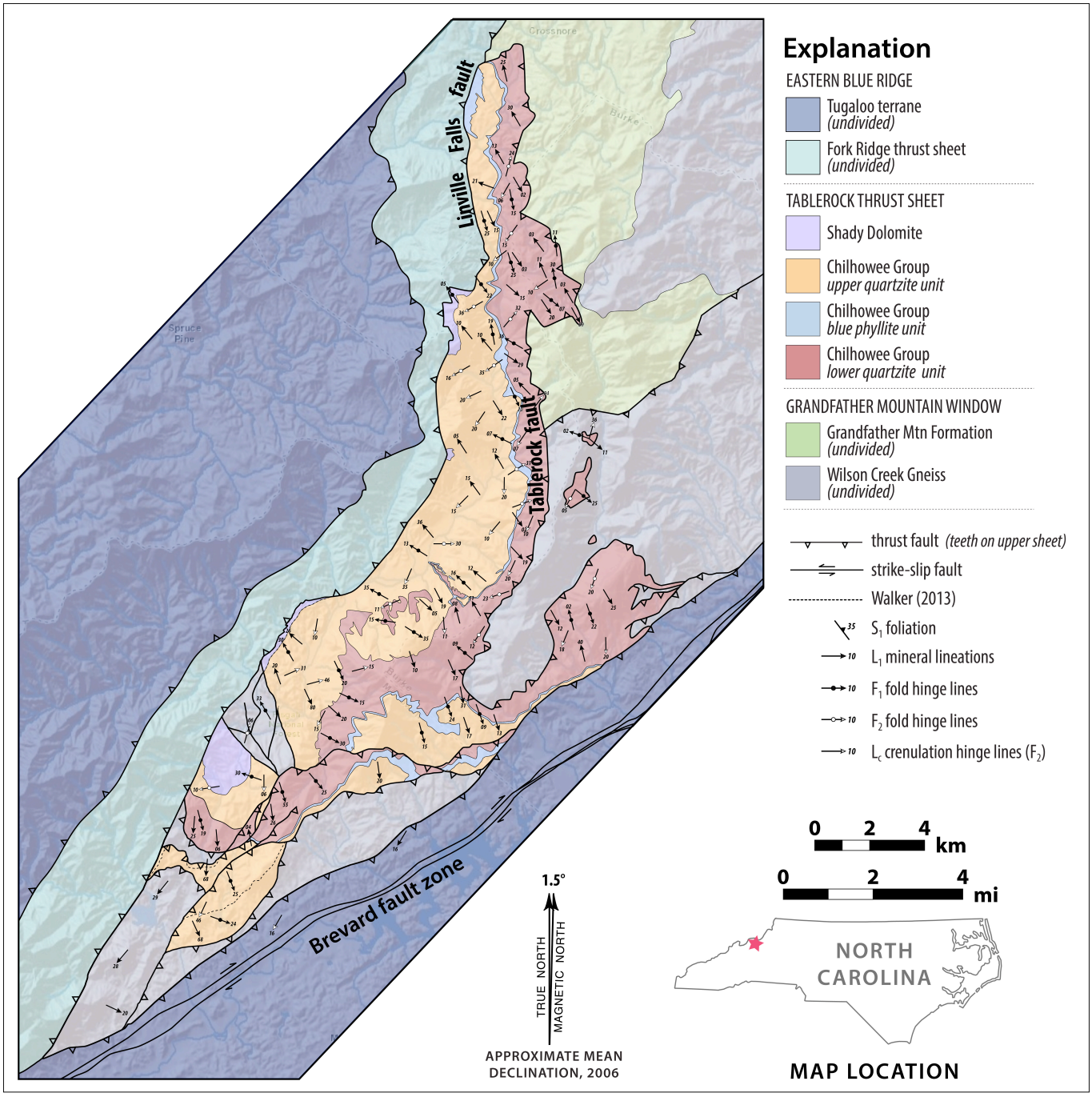

Figure 2.3: Geologic map of the Tablerock thrust sheet. F_1 fold hinges and L_1 lineations have nearly parallel, SE/NW-trending orientations, and form high- to orthogonal angles with NE/SW-trending F_2 crenulations and fold hinges. Star on inset map indicates the location of the Grandfather Mountain window just east of the Tennessee–North Carolina border. Tugaloo terrane west of the Brevard fault zone is part of the Eastern Blue Ridge, while Tugaloo terrane east of the Brevard fault zone is part of the Western Inner Piedmont. Dashed lines represent the locations of contacts and faults as originally mapped by Bryant and Reed (1970). Dashed line representing the contact between the Shady Dolomite and upper quartzite unit along the Linville Falls fault northeast of the Woodlawn quarry is newly mapped based on data presented by Bozdog et al. (2012) and Walker and Hatcher (2012b). Updated boundaries are based on observations and field measurements made during the field work for this study, but are not high-precision. After Bryant and Reed (1970); Hatcher et al. (2006); Walker & Hatcher (2012a, 2012b).

CHAPTER 3 | LITHOSTRATIGRAPHY OF THE TABLEROCK THRUST SHEET

The Chilhowee Group is a thick succession of Neoproterozoic to Early Cambrian quartzite, feldspathic quartzite, and phyllite exposed in belts along the external margin of the central and southern Appalachian Blue Ridge (Mack 1980; Cudzil & Driese 1987; Simpson & Sundberg 1987; Walker & Driese 1991). It was deposited on the Laurentian margin during the opening of the Iapetus ocean, and preserves the evolution of the margin from active rift-zone to stable shelf environment (Bryant & Reed 1970; Cudzil & Driese 1987; Simpson & Sundberg 1987; Walker & Driese 1991). Lithostratigraphic and paleocurrent data indicate Chilhowee Group rocks reflect a transition from terrestrial braidplain deposition to a tide-dominated marine shoreface, and again to a storm-influenced shelf environment (Mack 1980; Cudzil & Driese 1987; Walker & Driese 1991).

Northwest of the Grandfather Mountain window the Shady Valley thrust sheet, Mountain City window, and Doe Ridges inner-window contain Chilhowee Group rocks correlated with the Erwin, Hampton, and Unicoi Formations in northeast Tennessee (Fig. 2.1) (King & Ferguson 1960). Lithologic and stratigraphic data, and the presence of *Skolithos sp.* tubes indicate the Tablerock thrust sheet also contains Chilhowee Group rocks and Shady Dolomite. However, folding and pervasive deformation in the Tablerock thrust sheet—as well as the great distance between it and other Chilhowee Group rocks—prevented previous workers (e.g. King & Ferguson 1960; Bryant & Reed 1970) from identifying specific Chilhowee Group formations in the Tablerock thrust sheet. The extensive folding also makes stratigraphic thicknesses difficult to measure, but structural cross sections by Bryant and Reed (1970) and Boyer (1978) indicate the thrust sheet contains at least 1200 m of Chilhowee Group rocks.

3.1 Lithostratigraphic units

The lower quartzite unit (**Ꞓ**cl) is a package of white, gray, and greenish-gray quartzite with interbedded laminations of lustrous green phyllite (Fig. 3.1; Fig. 3.2D–F); it ranges in thickness from 250 m to 670 m, and contains layers a few centimeters to as much as 9 m thick (Bryant & Reed 1970). The quartzite is generally coarse-grained, feldspathic, and sugary; it contains horizons of metamorphosed quartz-

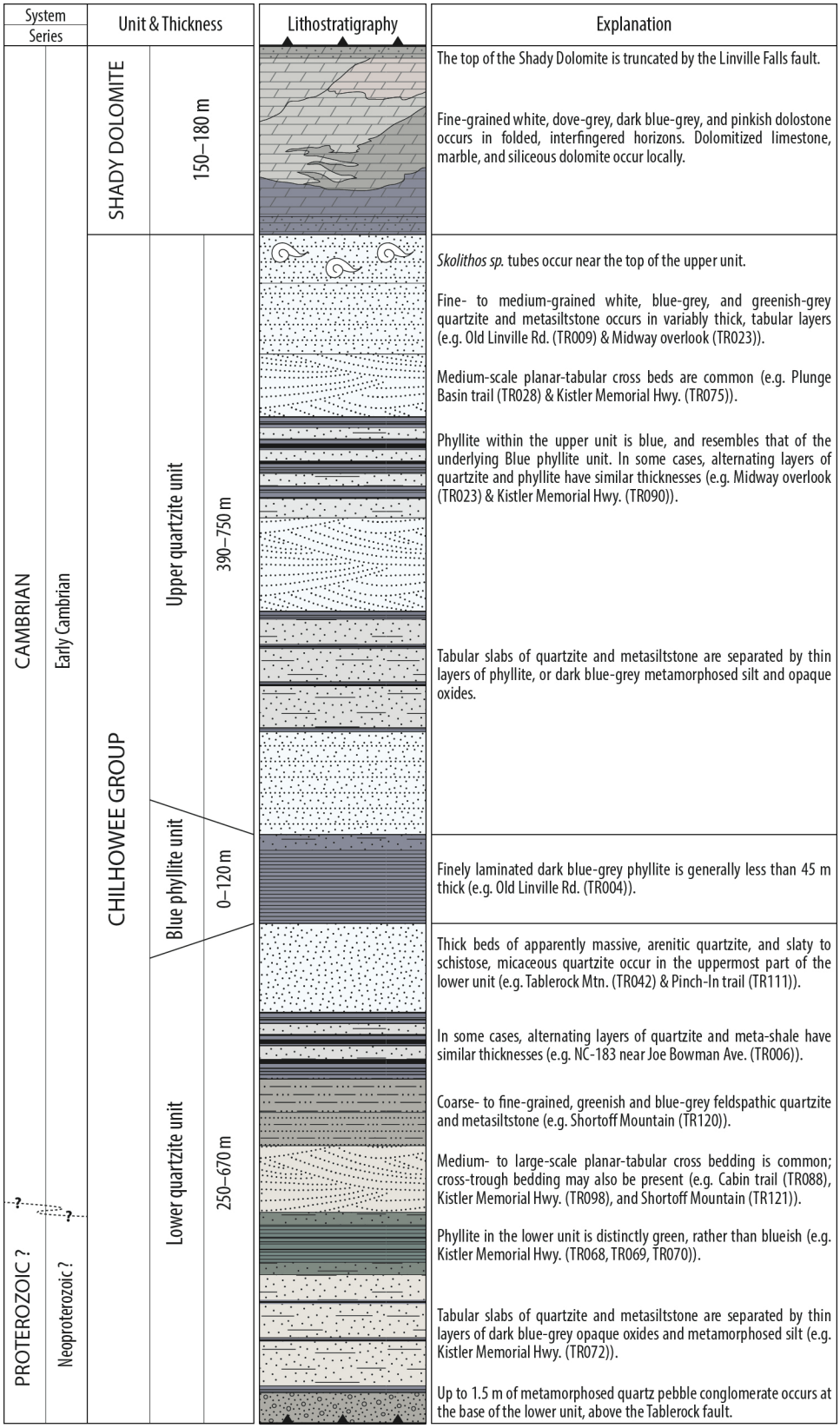

Figure 3.1: General lithostratigraphy of the Tablerock thrust sheet. The vertical positions and thicknesses of lithostratigraphic horizons within each unit are schematic, and intended for illustrative purposes only.

pebble conglomerate up to 1.5 m thick at the base, conspicuous beds of arenaceous quartzite and metasiltstone in the upper section, and approximately 20 m of vitreous quartzite near the contact with the overlying blue phyllite unit (Bryant & Reed 1970; Walker & Driese 1991). The lower unit is unfossiliferous and commonly contains cross-stratified beds. Where it contacts arkose and siltstone of underlying Grandfather Mountain Formation rocks, the lower quartzite unit can be distinguished by its laterally continuous stratigraphy, lower feldspar content, fewer conglomerate beds, and the presence of detrital tourmaline (Reed 1964; Bryant & Reed 1970).

The lower quartzite unit grades into the blue phyllite unit (Ꞓcp)—a thin, but continuous sequence of lustrous, dark blue-gray phyllite locally interbedded with sugary bands of white, gray, and blue quartzite (Fig. 3.1; Fig. 3.2C) (Bryant & Reed 1970). The exposed thickness of the blue phyllite unit varies from 0–120 m, but is generally less than 45 m in most places; bands of vitreous blue to white quartzite 3.0 cm–6.5 m thick are common where the phyllite reaches thicker intervals (Bryant & Reed 1970). The rock is strongly foliated along fine, transposed bedding laminations, and is often crenulated by millimeter-scale folds on the bedding-parallel foliation surfaces.

The top of the blue phyllite unit transitions into 390–760 m of fine- to medium-grained white, blue-gray, and greenish-gray quartzite and metasiltstone of the upper quartzite unit (Ꞓcu) (Bryant & Reed 1970). Quartzite in the upper unit resembles that of the lower unit in both texture and composition, but is generally better sorted, lacks conglomerate beds, and contains more vitreous, blue to white quartz ite horizons (Bryant & Reed 1970). Interbedded laminations of lustrous blue-gray phyllite (Fig. 3.2A–B) are similar to phyllite of the middle unit, and distinct from the green variety common to the lower unit. The top of the unit is conformably overlain by Shady Dolomite (Fig. 3.1; Fig. 3.3) and contains a few deformed *Skolithos sp.* tubes in exposures along the east flank of Linville Gorge (e.g. Wilkins 1966; Bryant & Reed 1970), indicating at least part of the upper quartzite unit belongs to the Erwin Formation.

The top of the Tablerock thrust sheet is defined by an incomplete section of Shady Dolomite exposed along the western edge of the Grandfather Mountain window in quarries and sporadic outcrops near Woodlawn, Marion, North Cove, and Linville, North Carolina (Fig. 2.3; Fig. 3.3) (Wilkins 1966; Bryant & Reed 1970; Byrd 1973; Bozdog et al. 2012; Walker & Hatcher 2012b). The rock is extremely fine-

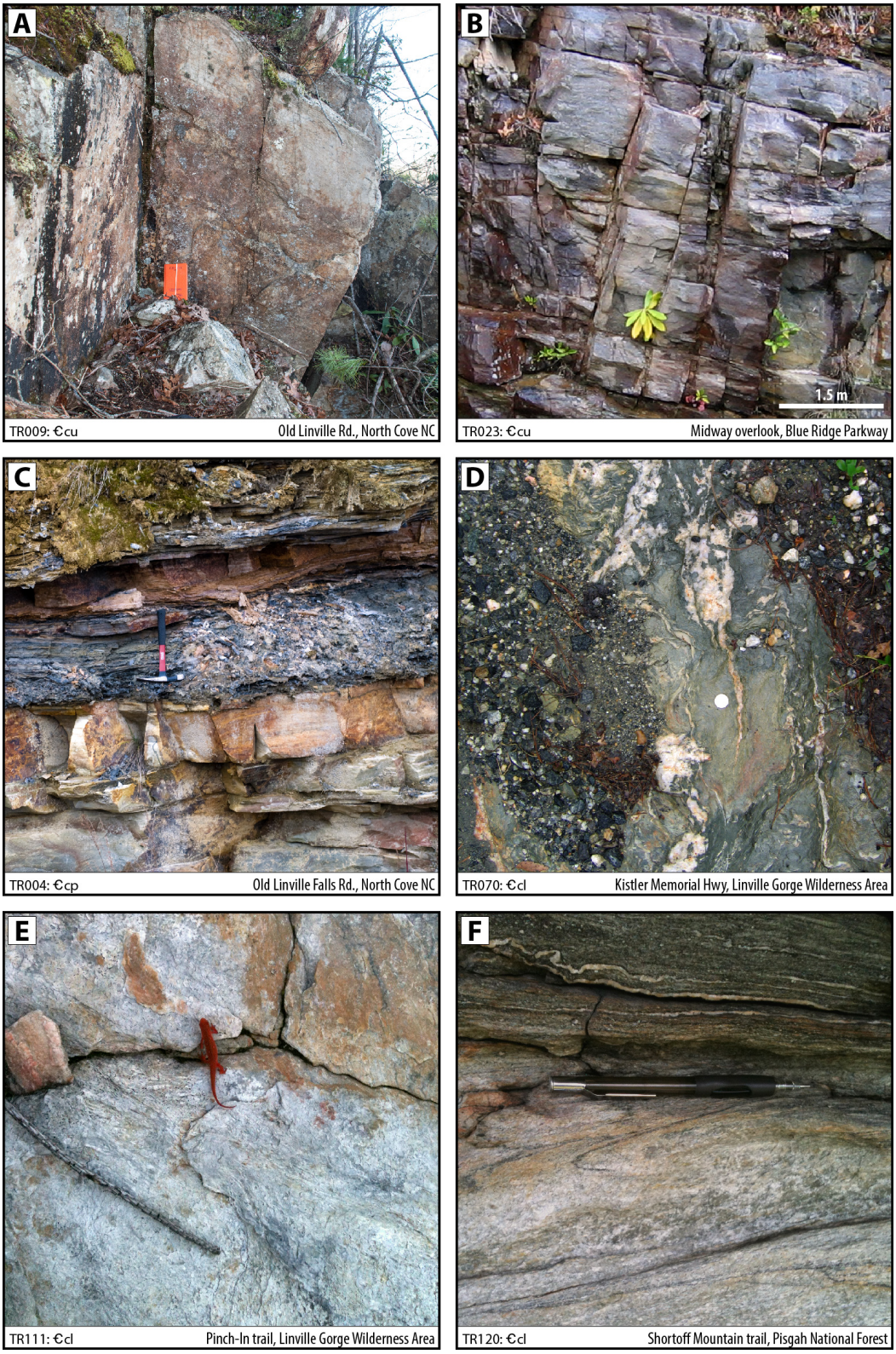

Figure 3.2: Chilhowee Group rocks of the Tablerock thrust sheet. (A) Moderately weathered arenaceous quartzite. (B) Blue, gray, and buff quartzite, and metasiltstone. (C) Thick dark blue-gray phyllite of the middle unit overlies massive white quartzite of the lower unit. (D) Green, lustrous phyllite typical of the lower unit; note coin in center of phyllite for scale. (E) Massive blueish-white quartzite typical of beds toward the top of the unit. (F) Cross-bedded greenish and blue-gray feldspathic quartzite.

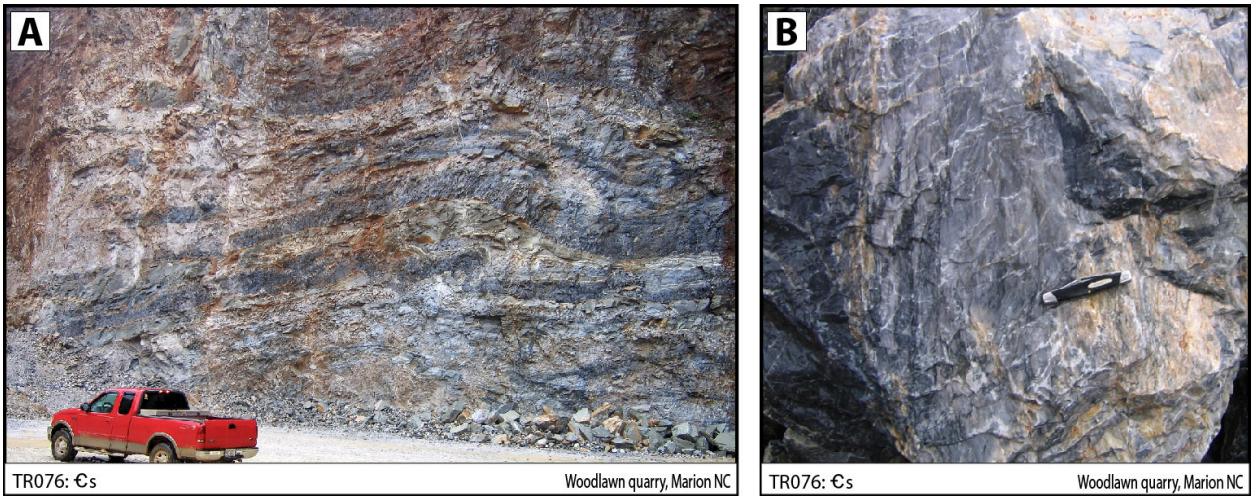

Figure 3.3: Buff, blue-gray, and dove-gray Shady Dolomite of the Tablerock thrust sheet. (A) Folded layers in quarry wall. (B) Close-up view shows the complex relationships between lithologies in the Shady Dolomite; knife is 8.5 cm long. Photos taken with permission on-site at Explosive Supply Co. (Woodlawn quarry), American Thread Rd., Marion, NC.

grained, and has a complex fabric defined by folded, lobate horizons of interfingered white, dove-gray, dark blue-gray, and pinkish dolostone. Thin layers of gray, dark green, and greenish-gray phyllite are common throughout the section, while sugary to porcelaneous dolomitized limestone, marble, and siliceous dolomite occur locally (Bryant & Reed 1970; Byrd 1973; Bozdog et al. 2012; Walker & Hatcher 2012b). Shady Dolomite adjacent to the Linville Falls fault is mylonitic, but quickly grades into more massive rock away from the fault zone (Trupe 1997).

The conformable contact between the upper quartzite unit and overlying Shady Dolomite indicates the Tablerock thrust is at least partially comprised of rocks equivalent to the Erwin Formation—and the similarity between the compositional and textural characteristics of upper and lower unit rocks, and the absence of tuffs and volcanic flows indicative of some Unicoi rocks indicate the entire thrust sheet may belong to the Erwin Formation. Similar successions of alternating quartzite, metasiltstone, and phyllite beds are exposed in upper unit rocks at Midway overlook on the Blue Ridge Parkway, and in lower unit rocks along NC-183, near Jonas Ridge. At Midway overlook the phyllite and metasiltstone beds thin and disappear as the quartzite beds thicken up-section. Medium to large-scale sets of planar-tabular and trough cross beds are preserved in thick successions of quartzite; trough cross beds may also be present at locations where the lateral and stratigraphic continuity of large-scale cross bedding is

compromised by weathering (including Pinch-In trail, Linville Gorge Wilderness Area; Plunge Basin trail in Linville Falls park, Blue Ridge Parkway; and the top of Wolf Pit trail, Shortoff Mountain). Given the large amount of strain accommodated by the Tablerock thrust sheet, it is possible the low angles of many cross beds observed during this study were produced by deformation rather than depositional processes.

Samples from the lower, middle, and upper Chilhowee units and Shady Dolomite are dominated by recrystallized quartz with variable amounts of feldspars, micas, and accessory minerals, except for local zones of mica-dominated mylonite in the Linville Falls shear zone. Feldspar content is 0–15% for all samples, and generally consists of microcline, perthite, microperthite, and rare plagioclase. There is no apparent difference in the content, behavior, or grain-character of feldspars from the different quartzite units: grain size ranges from ≤ 0.1 mm to as much as 5.0 mm, but is generally consistent within a given sample; most grains have slightly cloudy surfaces, but more advanced sieve textures are not uncommon; brittle fractures, quartz-muscovite strain shadows, and inclusions of epidote, muscovite, and zircon are common in larger grains.

Muscovite is the dominant phyllosilicate and occurs as colorless platy laths, fine-grained sericite, and green phengite (Fig. 4.1; Fig. 4.2C–D). Chlorite tends to be extremely fine-grained, colorless to clear-green, and often exhibits anomalous berlin-blue interference colors. Both chlorite and phengitic muscovite are pale green and weakly pleochroic, but are distinguished by the lower relief, parallel extinction, and 2nd-order interference colors of muscovite, and anomalous to low 1st-order interference colors and inclined extinction in chlorite. Biotite is stable in at least three samples, where fine-grained laths are light brown, contain almost no chlorite alteration, and often display anomalously weak absorption colors. In sample TR096 (**Є**cl), biotite, muscovite, and chlorite are locally associated with stringers and mats of fibrous sillimanite (Fig. 4.1C–F). Trace amounts of sillimanite also occur locally in samples TR002 (**Є**cu) and TR038 (**Є**cl) as superfine, prismatic needles included in original and recrystallized quartz grains. Where fibrous, sillimanite exhibits low 1st-order gray and yellow interference colors, and is commonly mantled by fine-grained biotite; a close association with K-feldspar is also common (Fig. 4.1C–F). Characteristic upper 2nd-order blue and purple interference colors and fractures perpendicular to the longest crystallographic axes are visible in the largest prismatic needles. Both crystal habits exhibit high relief against quartz, parallel extinction, and colorless to pale-brown pleochroism.

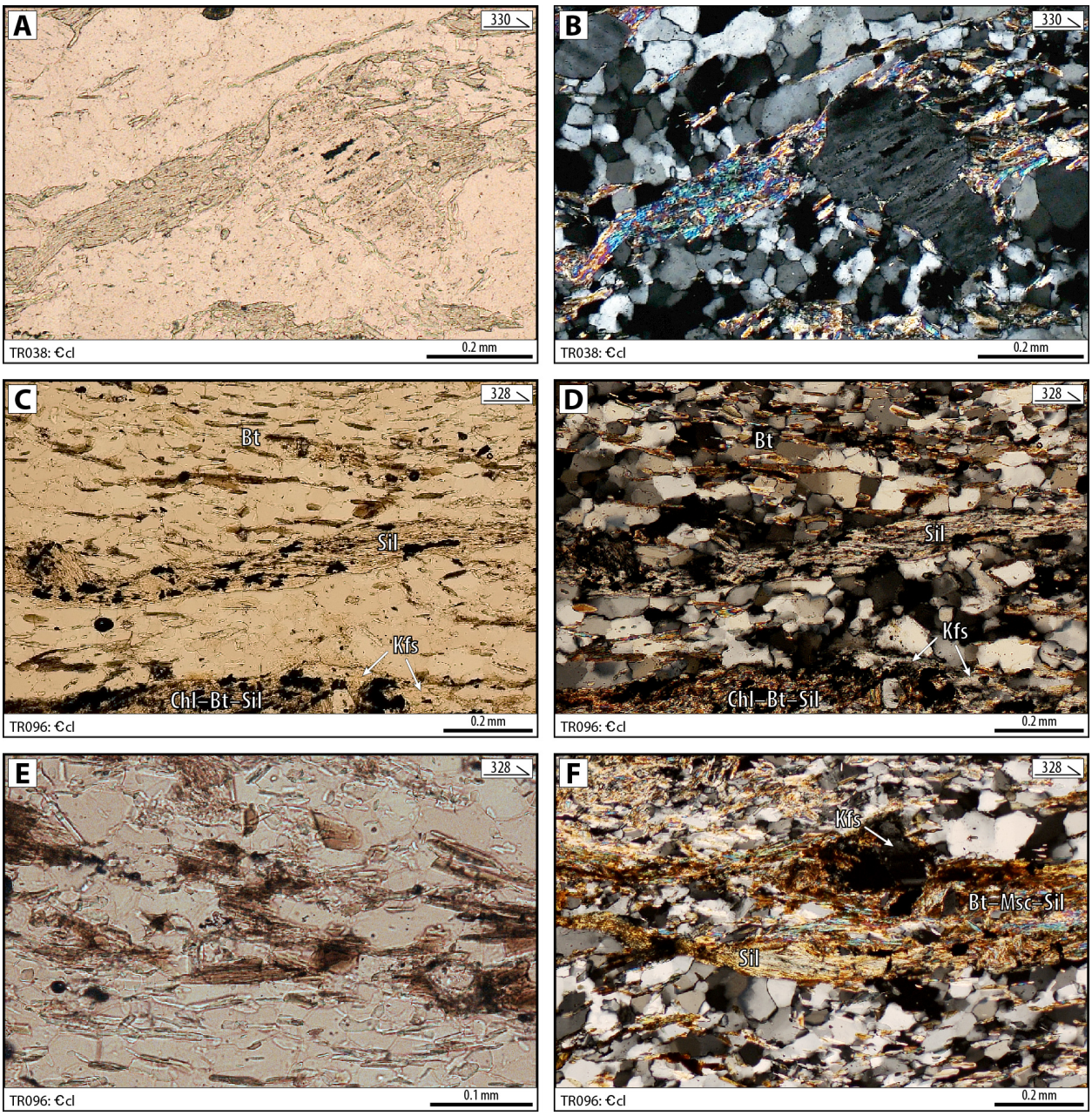

Figure 4.1: Optical characteristics of phyllosilicate minerals and fibrous sillimanite in the Tablerock thrust sheet. Sample number, map unit, and trend of L_1 are shown on each photomicrograph. Left column are viewed under plane-polarized light; right column shows the same photos under cross-polarized light. Bt is biotite; Chl is chlorite; Kfs is K-feldspar; Msc is muscovite; Sil is sillimanite. (A) & (B) Muscovite defines shear zones around a porphyroclast of K-feldspar. Phengitic muscovite exhibits light green absorption colors and weak pleochroism. (C) & (D) Fibrous sillimanite intergrown with biotite (center), and with biotite, chlorite, and K-feldspar (lower center). Brown to greenish-brown laths are biotite. Muscovite is also present, but individual grains cannot be distinguished here. Note ilmenite inclusions within mats of fibrous sillimanite. (E) Detailed view of biotite (brown); clear, colorless to light-green laths are muscovite, and smaller clear needles are chlorite. (F) Fibrous sillimanite is mantled by brown biotite, and associated with muscovite and K-feldspar.

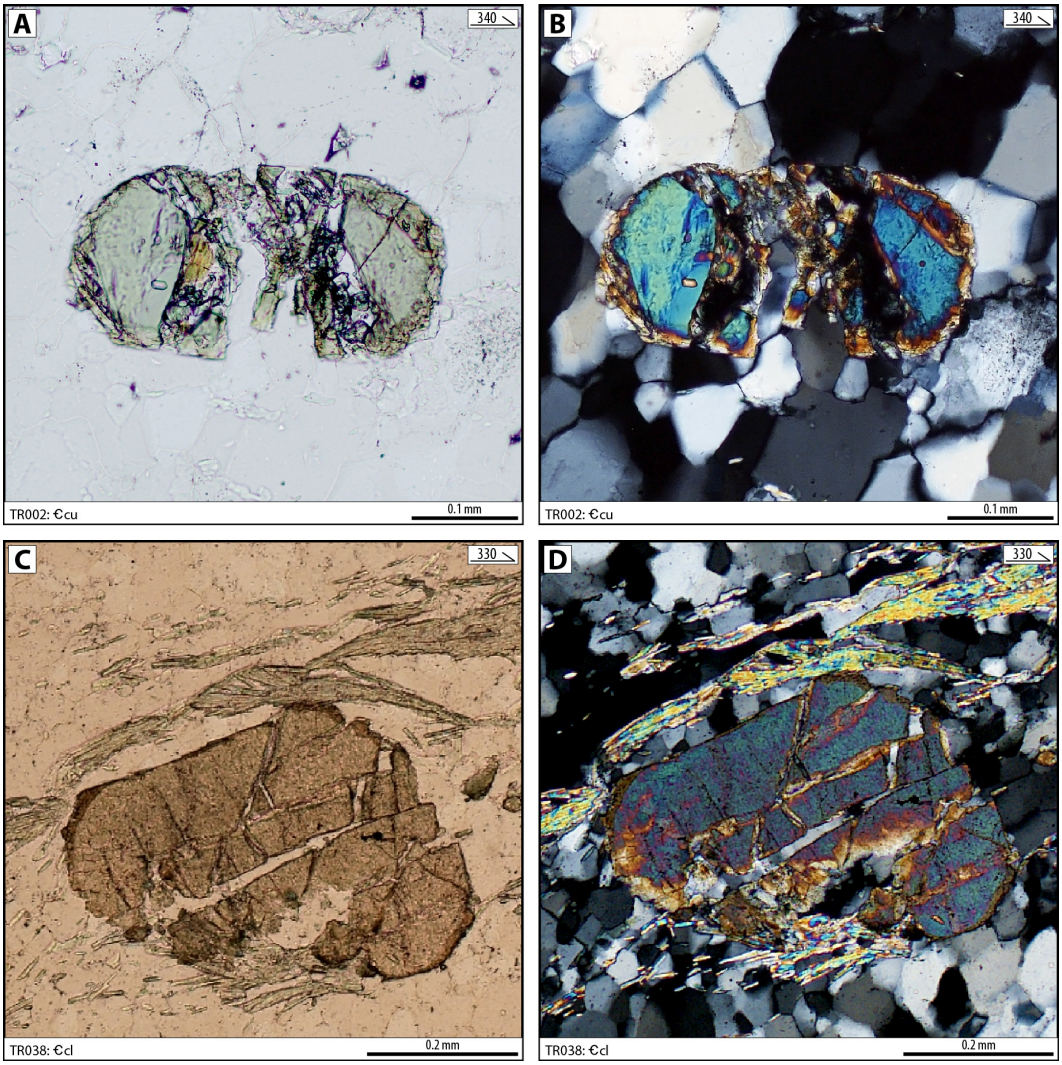

Figure 4.2: Photomicrographs of detrital tourmaline characteristic of Chilhowee Group rocks in the Tablerock thrust sheet. Left column are viewed in plane-polarized light, right column viewed in cross-polarized light; sample number, map unit, and trend of L_1 are shown on each photomicrograph. All three examples exhibit authigenic growth along grain boundaries. (A) Pale green crystal with small, radial growth of 2° tourmaline (light brown disc on inside edge of left fragment). (B) High relief against quartz is especially evident under crossed-polarized light. (C) Stubby prismatic grain with green phengite muscovite. (D) Strong absorption is characteristic, and darkens interference colors under cross-polarized light.

Epidote-group minerals, clinozoisite, detrital tourmaline, sericite, magnetite, and ilmenite–hematite (determined with reflected light microscopy) constitute the most common accessories, while zircon, rutile, apatite, and sphene occur in trace amounts; calcite and dolomite are locally abundant in the quartzite sample associated with the Shady Dolomite (TR043). Epidote minerals are most abundant in feldspar-rich samples, where small anhedral to subhedral grains (≤ 1mm) exhibit characteristic high relief and mottled 3rd-order interference colors; pale- to blue-green crystals display weak to moderate pleochroism in plane-polarized light. Clinozoisite is distinguished from epidote by its colorless, non-pleochroic crystals and 2nd-order yellow and orange interference colors; granular clusters of small, berlin-blue clinozoisite grains may represent an iron-poor composition (Deer et al. 1992). Small detrital grains of euhedral to subhedral zircon have characteristic prismatic, doubly terminating crystals, and high relief against quartz. Large, conspicuous grains of green and brown detrital tourmaline are diagnostic of Chilhowee Group rocks in the Grandfather Mountain window, and distinguish them from similar sequences of the Grandfather Mountain Formation (Bryant & Reed 1970). Subhedral prismatic crystals exhibit low 3rd-order interference colors, parallel extinction, and moderately high relief, and display moderate to strong dichroism with maximum absorption perpendicular to the vibration plane (Fig. 4.2).

CHAPTER 5 | MESOSCOPIC STRUCTURES

5.1 Foliations and lineations

Except in small outcrops of Shady Dolomite, rocks throughout the Tablerock thrust sheet are defined by alternating, variably thick layers of quartzite and phyllite that ostensibly preserve original bedding (S_0). However, intrafolial and sheath folds are common in quartz segregations and internally layered quartzites, indicating S_0 was transposed to form an S_1 foliation ($S_0 = S_1$). S_1 forms the dominant macroscopic foliation in the thrust sheet, and is generally defined by apparent bedding ($S_0 = S_1$), ~1–30 cm thick tabular layers of quartzite (Fig. 5.1C–D, F), and a well-developed slaty to schistose cleavage in micaceous quartzite and laminated phyllite (Fig. 5.1B). Tabular slabs of quartzite are separated by ~1–30 cm thick layers of phyllite (Fig. 5.1F) or millimeter-scale metamorphosed silt (Fig. 5.1D), and contain thin, semicontinuous bands of fine-grained micaceous quartzite and metasiltstone that parallel the S_1 plane. S_1 parallels or is slightly subparallel to compositional layering, except where foliation bisects the hinges of intrafolial and sheath folds, or transects the limbs of later, less-inclined folds; mylonites in the Linville Falls shear zone and Tablerock fault also parallel the S_1 foliation (Bryant & Reed 1970; Trupe 1997; Walker & Hatcher 2012b). S_1 dip directions (Fig. 5.2D–E) indicate the thrust sheet forms a broad, NW-vergent antiform with a moderate to steeply SE-dipping limb along Shortoff Mountain to the east, a sub-horizontal to gently NW-dipping limb across the central region of the thrust sheet, and a gently SW-plunging axis (Bryant & Reed 1970; Boyer 1978; Walker & Hatcher 2012b) (Fig. 5.2).

The strong SE/NW-alignment of micaceous minerals, fine-grained opaque oxides, and elongate aggregates of recrystallized quartz define a prominent mineral lineation (L_1) consistent with the regional lineation described by Bryant and Reed (1969, 1970), and others. In addition, LS tectonites (Fig. 5.1A) and stretched quartz pebbles (Fig. 5.1E) define an L_1 stretching lineation on the surface of S_1 (e.g. Walker & Hatcher 2012b), while the exposure of millimeter- to centimeter-scale intrafolial and sheath folds on the XY-plane defines an intersection lineation also consistent with L_1. A second, less-developed lineation trending NE/SW (Fig. 5.2D) may correspond to a different deformational event, a reorientation of the stress field, or a minor reorientation of the lineation that commonly occurs at lateral culminations on

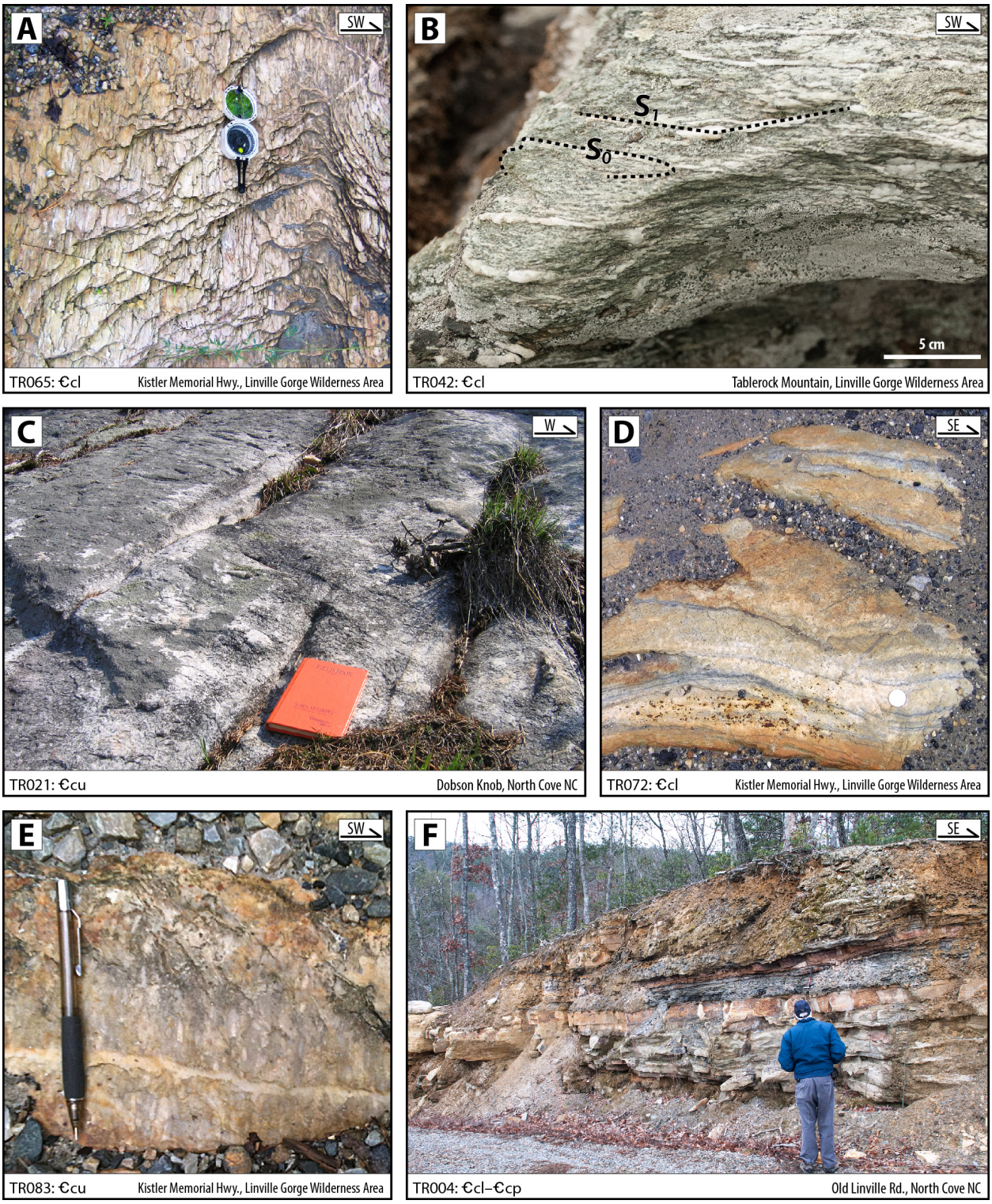

Figure 5.1: Summary of macroscopic foliations and mineral lineations in the Tablerock thrust sheet. Station number, map unit, and viewing direction are included on each photo. (A) Quartzite with strongly developed L_1 on the stretched foliation planes in an LS tectonite. (B) Slaty to schistose S_1 foliation bisects the hinges of intrafolial sheath folds in micaceous quartzite. (C) Thick, tabular quartzite layers, now overturned to a steep angle. (D) Comparatively thick beds of quartzite are separated by thin layers of metamorphosed dark, blueish-gray silt. (E) Stretched quartz pebbles and elongate aggregates of recrystallized quartz (roughly aligned with pencil). (F) Alternating layers of quartzite, phyllite, and metasiltstone at the contact between the lower quartzite unit and blue phyllite unit.

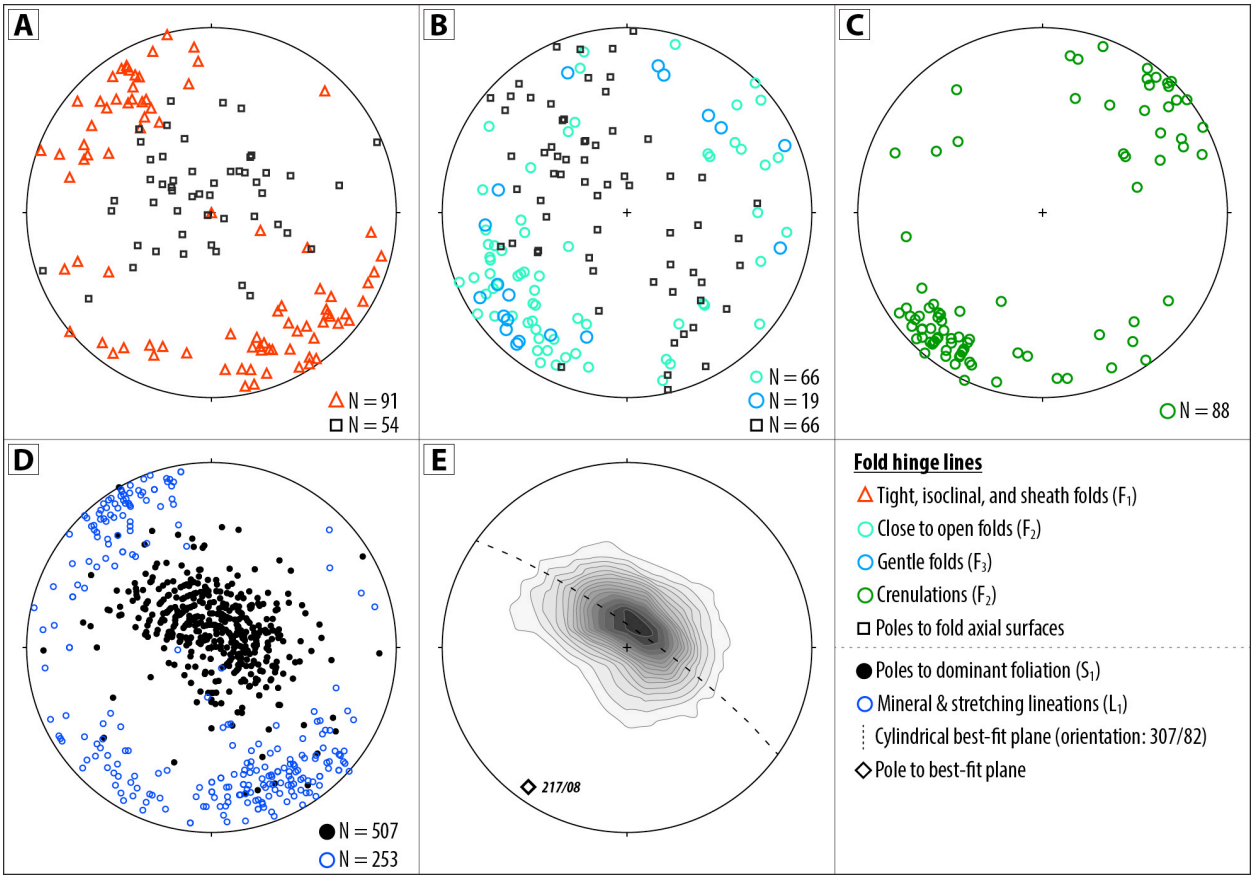

Figure 5.2: Equal-area, lower-hemisphere projections of mesofabric data from the Tablerock thrust sheet. (A) Tight, isoclinal,and sheath fold hinges, and poles to axial surfaces. (B) Close to open fold hinges, and poles to axial surfaces. (C) Crenulation hinge lines. (D) Lineations and poles to foliation planes. Foliations include 12 points of legacy data from Wilkins (1966); 244 from Bryant & Reed (1970); 93 from Trupe (1997);10 from Bozdog et al. (2012). Lineations include 108 points of legacy data from Bryant & Reed (1970), and 18 from Trupe (1997). (E) S_1 data contoured (Kamb contours; C.I. = 2σ). Dashed line is cylindrical best-fit plane (orientation: 307/82); black square is pole to best-fit plane. Fabric diagrams were produced using OSXStereonet 2.2, © Cardozo, N. & Allmendinger, R.W., 2012.

sheath folds (e.g. Skjernaa 1989; Alsop & Holdsworth 2004).

5.2 Mesoscale folds

Three generations of mesoscale folds are recognized in the Tablerock thrust sheet, and record the kinematic histories of two to three phases of deformation (Fig. 5.3). The earliest generation (F_1) consist of centimeter- to kilometer-scale folds with SE/NW-trending tight to isoclinal hinges, and recumbent, foliation-parallel axial surfaces (Fig. 5.2A; Fig. 5.4). Geometries resembling similar folds with harmonic interlayer wavelengths are common in thick, phyllite-poor sequences of quartzite, micaceous quartzite, and metasiltstone, while phyllite-hosted quartz segregations and thin layers of mylonitic quartzite

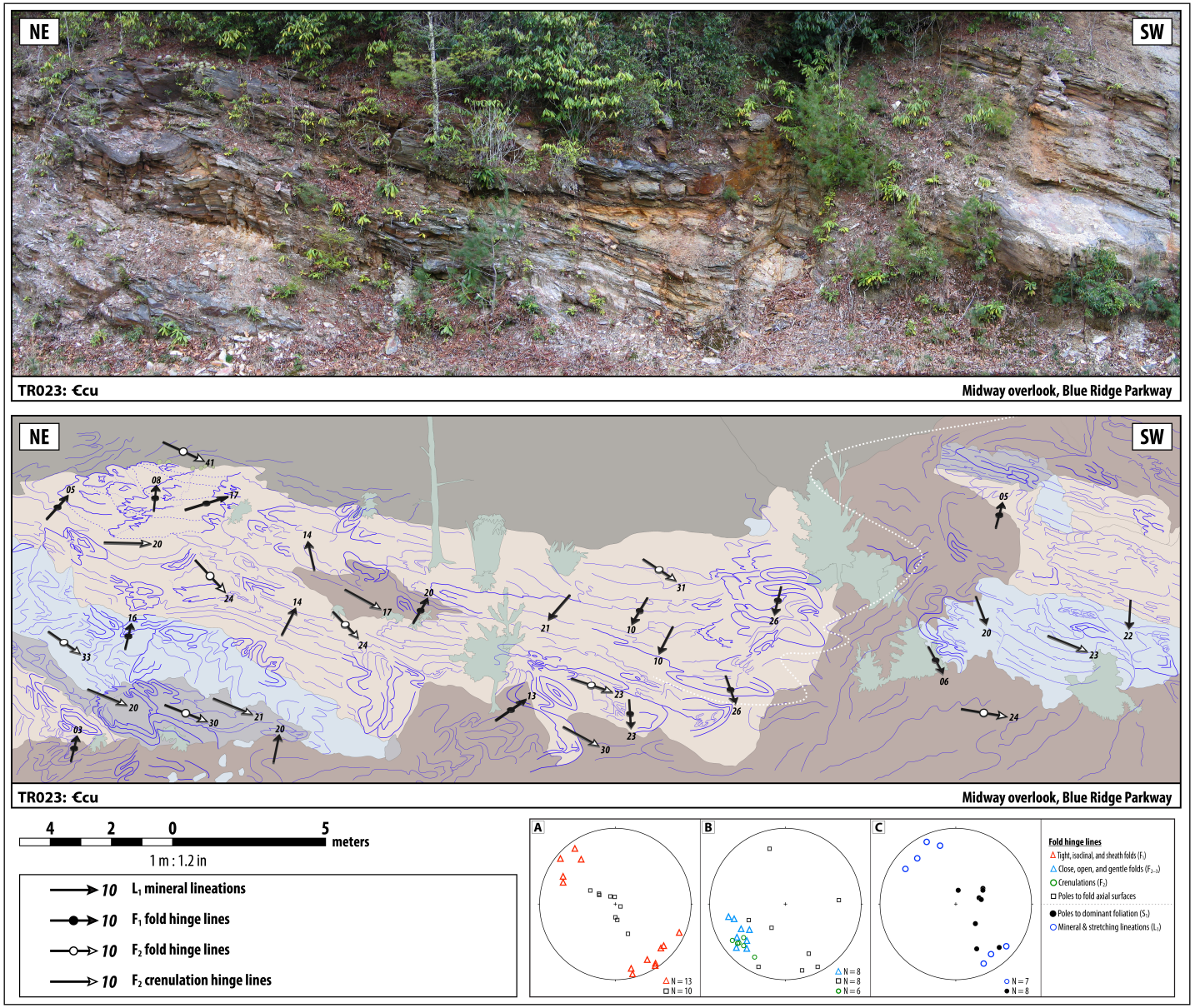

Figure 5.3: Structural relationships between fabric elements. Photo (upper) is part of the outcrop exposed at Midway overlook; simplified diagram (middle) shows measured orientations and schematic interpretations of structures mapped at this location. Colored polygons correspond to similar-colored regions in upper photo (and not to specific horizons or stratigraphic units). Blue lines correspond to major structures; large-scale folding (white dashed line) is inferred from the smaller scale structures.

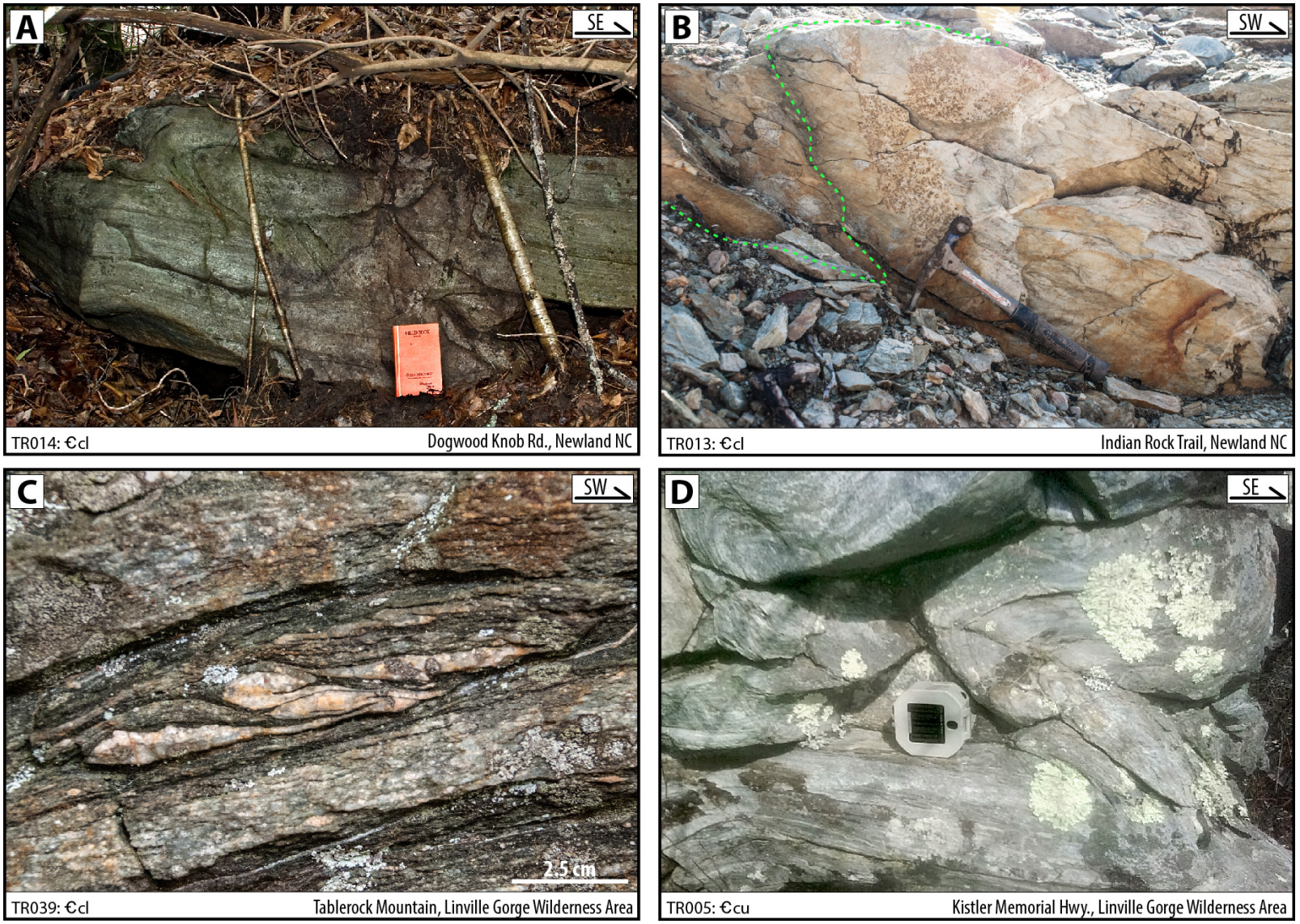

Figure 5.4: Summary of F_1 fold geometries. Station number, map unit, and viewing direction included on each photo. (A) Multilayer isoclinal folds in quartzite and metasiltstone (green color is due to moss). (B) The green dashed lined outlines an isoclinal fold pair in quartzite and phyllite. (C) Isoclinal intrafolial folds in quartz veins with thickened, lozenge-shaped hinges, and attenuated common limbs. (D) Complex geometries in isoclinally folded quartzite and metasiltstone.

frequently accommodate intrafolial and sheath folds (Fig. 5.4). All F_1 folds observed during this study have thickened hinges indicative of passive folding and heterogeneous plastic deformation. Common limbs between fold pairs are frequently thinned or completely pinched-out, while other limbs are thickened (Fig. 5.4). The noses of thickened hinges abruptly attenuate where folds have rotated into the effective flow plane, producing characteristic pinched, lozenge-shaped hinge zones (Fig. 5.4C).

Well-defined mesoscale sheath folds were observed in Chilhowee Group quartzites near Jonas Ridge in the northeast part of the thrust sheet, in the cliff wall across Linville Falls waterfall (looking southeast from Upper Falls overlook), and on Tablerock Mountain to the southeast (Fig. 5.5). Shady Dolomite exposed at Woodlawn quarry contains large-scale sheath folds; however, these could not be directly measured because of hazardous conditions. Although no well-preserved YZ-exposures of sheath noses were observed during this study, the nested clusters of sheath folds that form near the tips of nose cones are common (Fig. 1.2B). In addition to well-defined sheath folds and sheath-related structures, the strong NW-alignment between L_1 and F_1 hinges, and extensive occurrence of non-coaxial F_1 features at all scales, suggests sheath folds may be common throughout the thrust sheet.

F_1 structures are overprinted by NE/SW-trending asymmetric crenulations and open folds (F_2), and a later set of NE/SW-trending gentle folds and flexures (F_3); both F_2 and F_3 folds verge NW and have generally steep, SE-dipping axial surfaces (Fig. 5.2B). The relatively constant layer thickness in F_2 folds is consistent with parallel buckle folds (Fig. 5.6B); definitive slickenlines were not identified, suggesting layer thickness was maintained by flexural flow processes. Millimeter-scale crenulations are well-developed on the S_1 surfaces of finely laminated phyllite (Fig. 5.6A), and reach centimeter-scale in thinly bedded rocks and fault-zone mylonites; open folds range from centimeter- to meter-scale, and penetratively refold F_1 structures. The trend of F_2 folds is nearly perpendicular to the L_1 mineral lineation (Fig. 5.6A), and crenulation hinge lines bisect the tight hinges of SE/NW-trending F_1 folds; a poorly developed secondary lineation trending NE/SW (Fig. 5.2D) may correspond to an earlier event, or may represent relict F_2 crenulations where thin sheets (< 1 mm) of phyllite are almost completely removed by weathering. Axial-planar cleavage and fractures are well-developed in some F_2 folds, but are generally confined to the immediate hinge zone. F_3 structures are broad, meter-scale folds and flexures with very

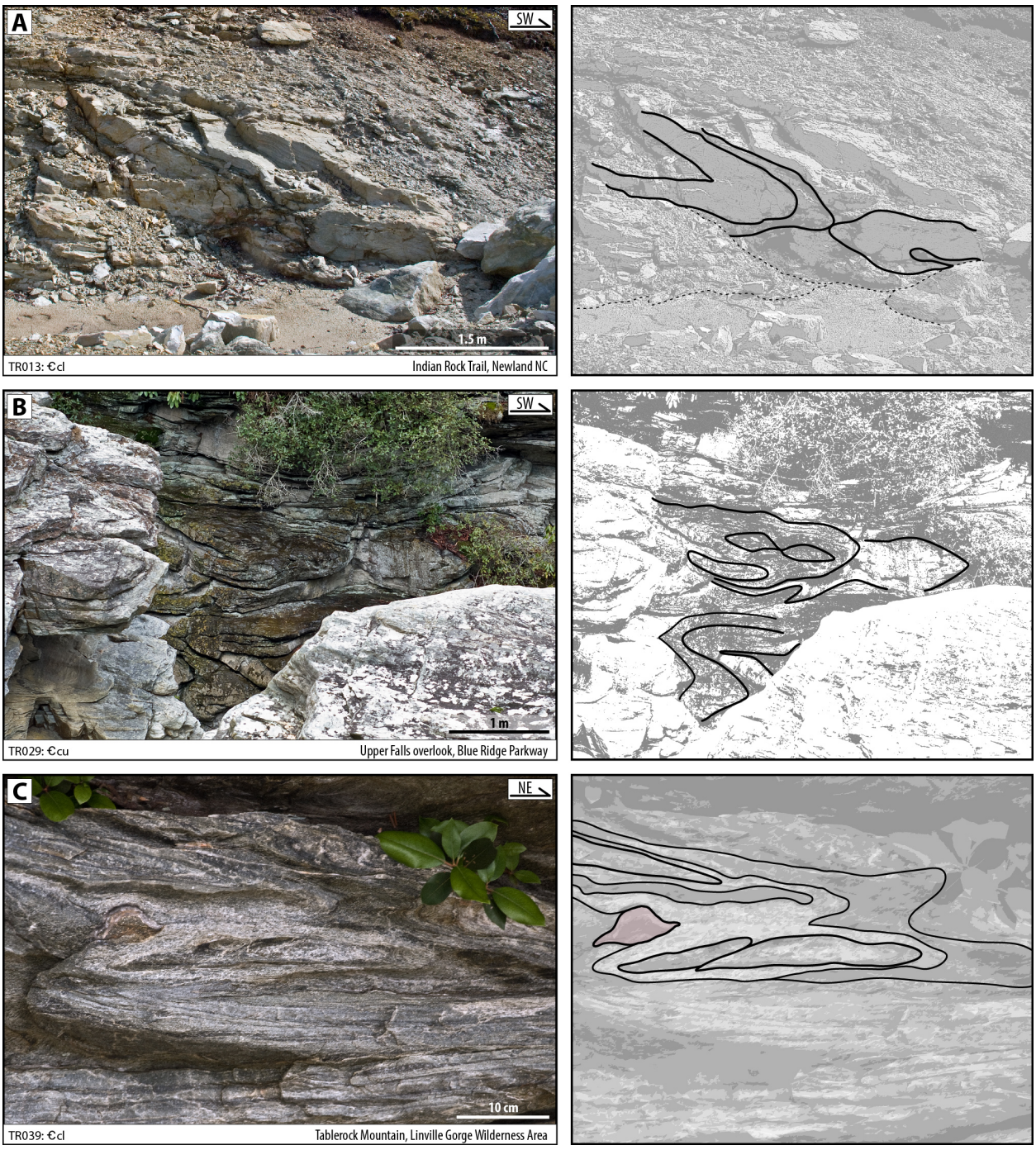

Figure 5.5: Mesoscale sheath folds. Station number and viewing direction included on each photo; right column are interpretive sketches. (A) Slightly oblique sections through the hinge nose (along XZ-planes). (B) Nested sheath folds exposed on the YZ-plane. Note—these folds are in the wall across Linville River from Upper Falls overlook, with Linville Falls waterfall plunging to the right of the photo. (C) Characteristic anvil-shaped profile produced by cross sections on the YZ-plane of tubular sheath folds. Mauve-colored polygon outlines the very tip of an intact sheath nose between two anvil-shaped cross sections.

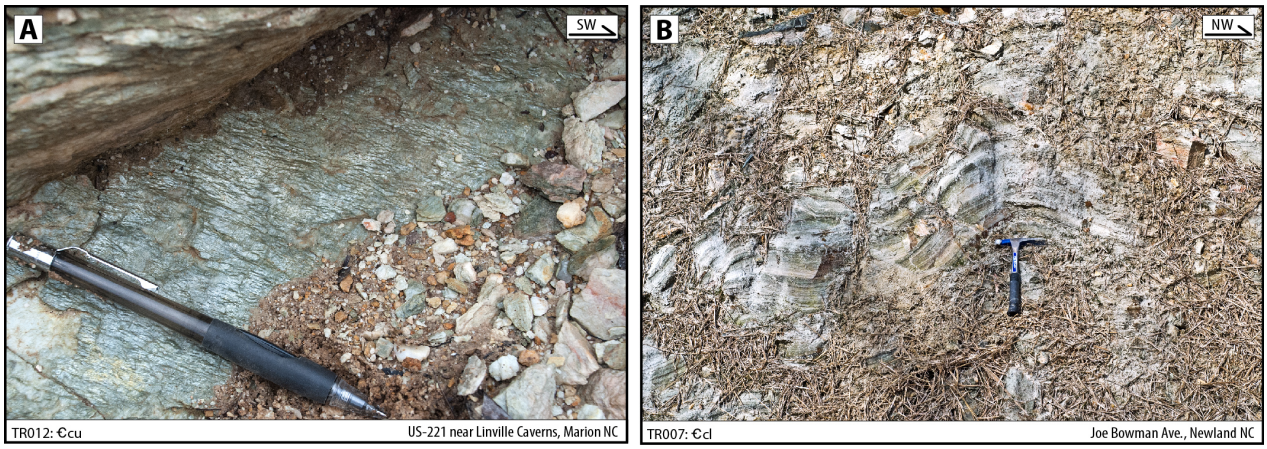

Figure 5.6: Summary of F_2 fold geometries. Station number, map unit, and viewing direction are shown on each photo. (A) F_2 crenulations in chlorite-rich phyllite; L_1 is approximately perpendicular to the pencil. (B) Mesoscale open fold in quartzite and metasiltstone.

large interlimb angles; they are interpreted here as the products of bending, or buckling—possibly related to the final movement of the overriding thrust complex (e.g. Boyer 1978)—but may also represent a late phase of F_2 flexural folding rather than a separate fold generation. F_3 folding does not appear to be penetrative.

5.3 Fold analysis

While Trupe (personal com., 2012) identified the same mesoscale sheath folds shown in Figure 5.5C during his doctoral research (e.g. Trupe 1997), sheath folding is substantially more prevalent in the Tablerock thrust sheet than previously recognized (Walker & Hatcher 2012b). The majority of F_1 folds observed during this study are centimeter- to meter-scale sheath folds or highly curvilinear folds, including those shown in Figure 5.3, and Figure 5.4C. Although Bryant and Reed (1969, 1970) didn't recognize sheath folding in the Tablerock thrust sheet, their illustrations of F_1 folds bisected by F_2 crenulation hinge lines are consistent with YZ-cross sections of sheath folds.

Classic sheath geometries may not be immediately obvious in the Tablerock thrust sheet because strong transposition, sheared-out common limbs, F_2 folding, and oblique profiles through the XZ- or YZ-planes have obscured the anvil-shaped cross sections and cone-like axial culminations generally associated with sheath folds (Fig. 5.7). In addition, recent experimental studies by Reber et al. (2013a,

b) indicate the structures traditionally associated with sheath folds only account for a small part of the overall sheath structure, and that sheath folding is not precluded by their absence in outcrop. In these studies, Reber et al. (2013a, b) demonstrated that the three-dimensional extent and geometry of slip-surface sheath folds is largely controlled by strain magnitude, the pre-deformation shape and orientation of the slip surface, and viscosity gradients between mechanical layers. For example, Reber et al. (2013b) showed that fully closed fold layers and anvil-shaped structures are difficult to identify with increasing proximity to the slip surface because they have large, variable aspect ratios. Additionally, Reber et al. (2013a) showed that sheath folds may not be visible at outcrop-scale when the ratio of inclusion height to layer thickness (their Π_3 parameter) is either too large or too small—because individual thin layers are difficult to distinguish and may pinch-out, while anvil structures are coarse, poorly defined, or absent in thick layers. The experimental results of these two studies are also consistent with observations and detailed studies of natural sheath folds (e.g. Alsop & Holdsworth 2006; Alsop et al. 2007; Alsop & Holdsworth 2012).

As discussed earlier, NW-trending mesoscale folds in the Tablerock thrust sheet tend to have tight to isoclinal hinges while NE-trending folds tend to be more open; however, tight folds are not always NW-trending, nor are open folds always NE-trending (Fig. 5.2A–C). Based on similar observations, Bryant and Reed (1969, 1970) suggested the axial surfaces and hinge lines of open and tight fold populations show a gradational transition that reflects the progressive rotation and tightening of the former to produce the latter. However, none of the structures observed during this study were intermediate between F_1 and F_2. SE/NW-trending open folds are instead interpreted as oblique sections through the YZ-planes of sheath folds; the outermost enveloping surfaces of sheath folds (Fig. 1.2A); and the second-order culminations and depressions produced by en echelon stacks of sheath folds (Fig. 1.2B; Fig. 5.8). Some NE/SW-trending tight and isoclinal folds could likewise be attributed to oblique sections through F_1 sheath folds on the XZ-plane. Alternatively, NE/SW-trending tight and isoclinal folds may represent minor F_1 culminations on sheath folds that developed oblique to L_1 (Fig. 1.2B; Fig. 5.8) because of strain gradients around larger scale culminations and depressions (e.g. Alsop & Holdsworth 2004).

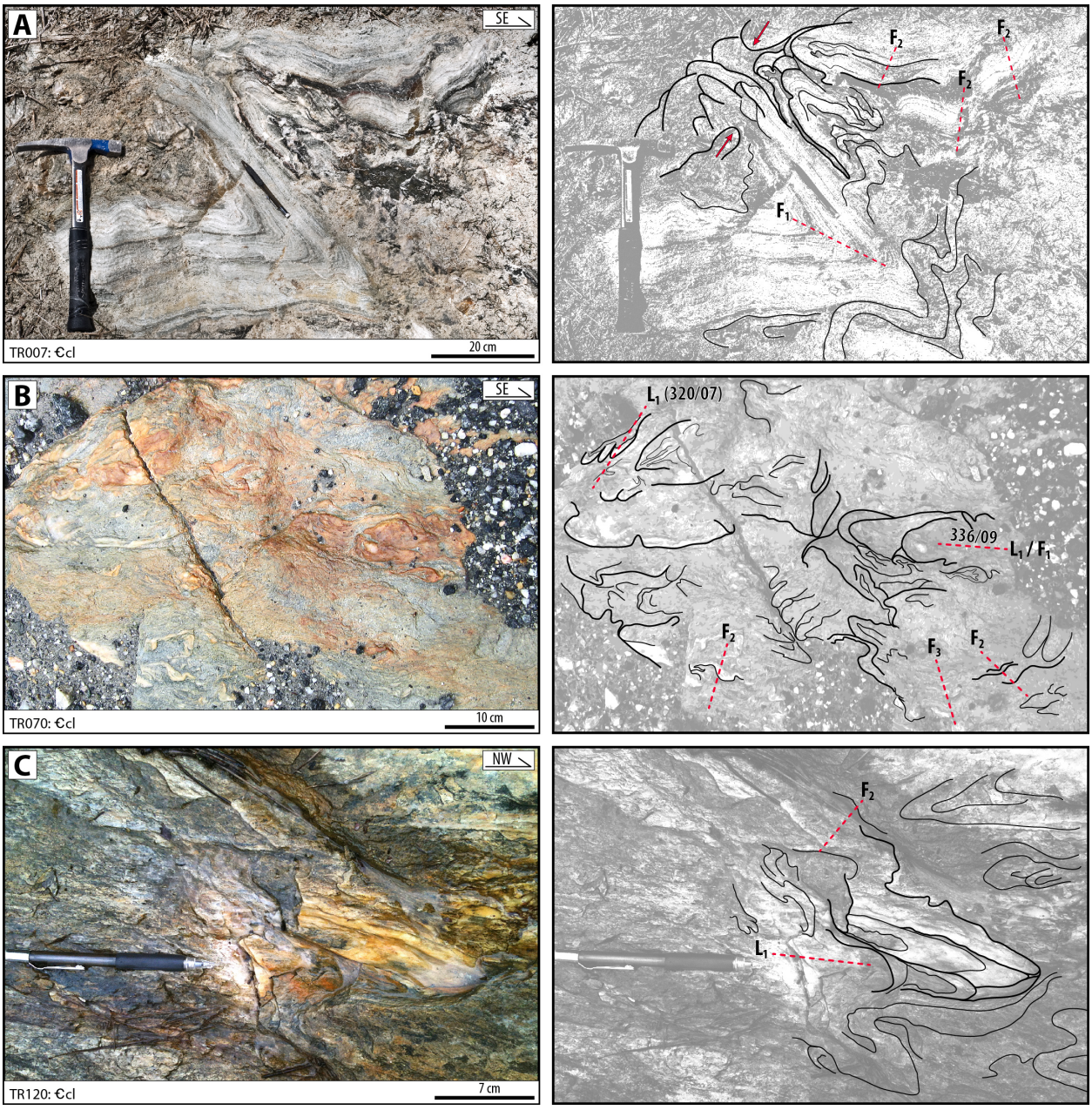

Figure 5.7: Obscured and non-classical sheath fold geometries. Station number and viewing direction included on each photo; right column are interpreted sketches. (A) Nested cones are exposed on the XZ-plane of finite strain in the upper limb (to the right of the pencil); the lower limb (left of pencil) is obliquely exposed on the XY-plane, as if looking down through the top of a sheath fold. Red arrows indicate opposite fold vergence associated with anvil-shaped cross sections. Joe Bowman Ave., Newland NC. (B) Sheath folds in thin layers of quartz mylonite (white and brown) hosted in green phyllite. L_1 parallels F_1 in the axis of nested, en echelon folds (right side of photo). The trend of L_1 deviates by ~20° as it approaches the edge of the fold, but is still subparallel with the trends of small, lateral culminations (upper left). Kistler Memorial Hwy., Linville Gorge Wilderness Area. (C) Nearly complete sheath cone in mylonitic quartzite. F_2 corresponds to sub-millimeter crenulations that are difficult to see in the photo. Note that apparent cleavage left of the "NW" arrow is actually due to pine needles draped over the ledge. Shortoff Mountain, Pisgah National Forest.

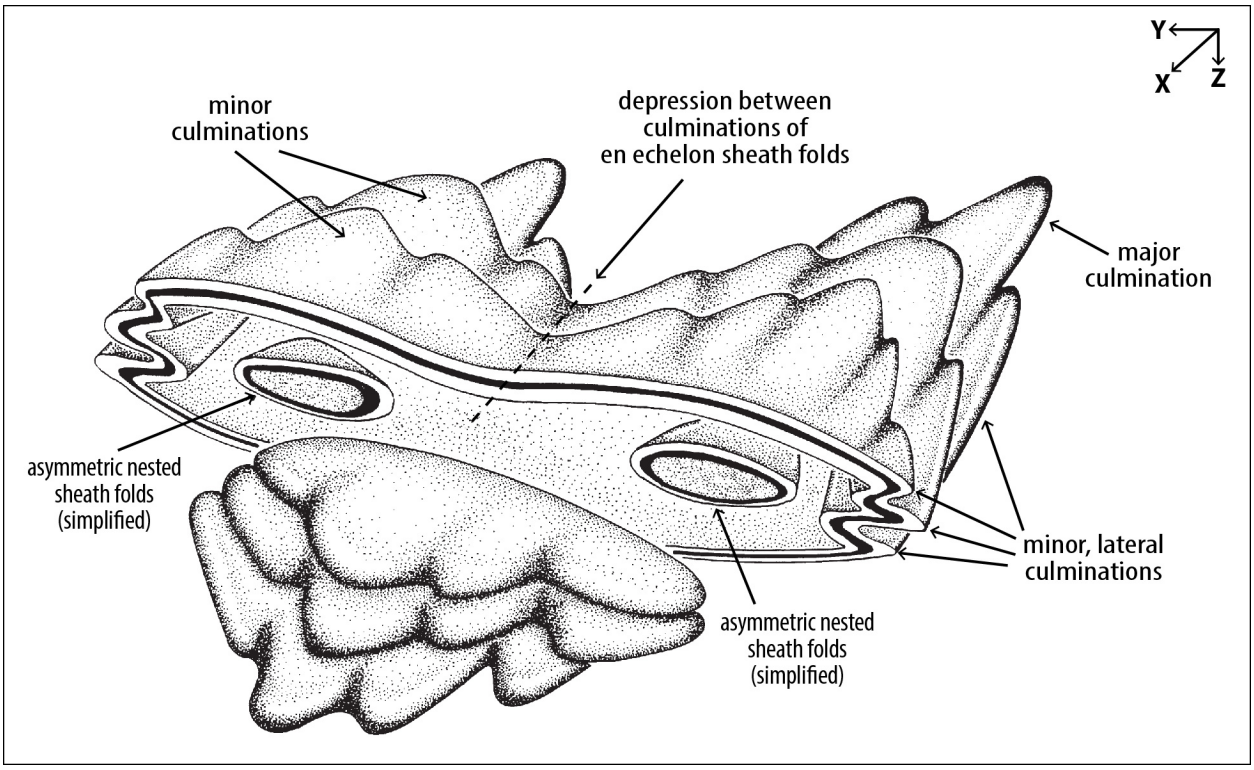

Figure 5.8: Culminations and depressions associated with sheath folds. Culminations/depressions around stacks of sheath folds ("culmination/depression surfaces" of Alsop & Holdsworth 2004) may account for SE/NW-trending open and gentle folds. After Alsop and Holdsworth (2004).

The occurrence of boudinage in the limbs of several sheath folds (Fig. 5.9) indicates deformation included a component of extension, at least locally. Boudins in the Tablerock thrust sheet are asymmetric, and display characteristics typical of ductile to semi-ductile deformation (e.g. Goldstein 1988; Gosh & Sengupta 1999; Goscombe et al. 2004)—including rounded, sigmoidal bodies, thinned necks, and shear-band type fractures (Fig. 5.9). In all observed cases, boudins are overprinted by F_2 and/or F_3 folds (Fig. 5.9). Boudinaged fold limbs could indicate that F_1 structures formed by constriction of pre-existing curvilinear folds during transpression (e.g. Bailey et al. 2004), or constriction and flattening during pure shear (e.g. Ez 2000; Mandal et al. 2009). However, asymmetric porphyroclast tails, SC fabrics, and oblique grain-shape fabrics are common throughout the Tablerock thrust sheet, indicating the bulk deformation was dominated by simple shear rather than pure shear, although, these criteria do not preclude general shear with a non-coaxial component (Ez 2000; Bailey et al. 2004).

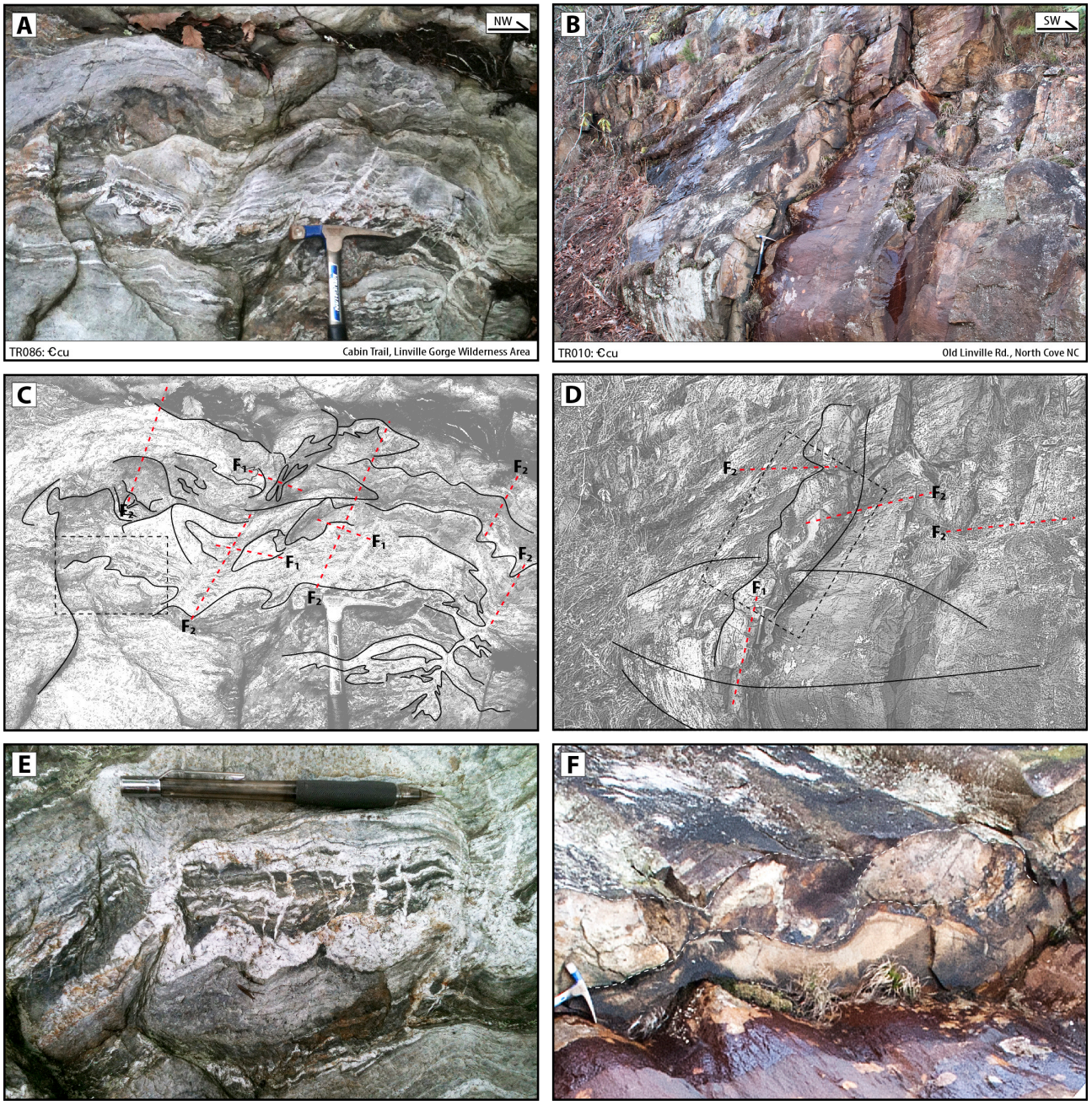

Figure 5.9: Boudinage in the limbs of F_1 sheath folds. Station number and viewing direction included on each photo. Black dashed boxes in (C) and (D) correspond to the areas magnified in (E) and (F), respectively. (A) Sheath folds in upper unit quartzites at the contact with the blue phyllite unit; photo corresponds approximately to the XZ-plane of finite strain. Quartz-filled shear fractures separate asymmetric, rotated boudins. (B) Nose of a large F_1 sheath fold with a boudinaged enveloping surface. (C) & (D) Interpreted sketches of photo-A and photo-B, respectively; note that in both cases, boudinaged layers are overprinted by F_2 and/or F_3 folds. (E) The orientation of quartz-filled shear fractures places the maximum principal stress axis (σ_1) roughly orthogonal to the pencil, while the boudin orientation indicates the X-direction of finite strain roughly parallels the pencil; shear sense is top-right. The boudins are shearband-type (e.g. Goscombe et al. 2004) with synthetic offset between boudins; the apparent antithetic offset is interpreted here as overprinting by NW-vergent F_2 and/or F_3 folds. (F) Asymmetric, sigmoidal boudins in quartzite and metasiltstone with intact necking zones (outlined by white dashed lines); shear sense is top-left.

Dynamic recovery and recrystallization describe the intracrystalline strain that accommodates dislocation creep in an aggregate during deformation. In geologic materials, recovery reduces internal strain in original grains by organizing dislocations into wall-like arrays, forming a transient, internal subgrain structure (Humphreys & Hatherly 2004; Hull & Bacon 2011). Dynamic recrystallization generates a fine-grained, recrystallized matrix with low dislocation density, which makes it capable of accumulating strain after the original material becomes too work-hardened to produce and migrate sufficient dislocations to maintain ductile flow (Karato 2008). Because the process is thermally activated, the microstructures produced by dynamic recrystallization are characteristic of the deformation conditions under which they formed (Hirth & Tullis 1992; Stipp et al. 2002; Tullis 2002; Stipp et al. 2010). At natural and experimental conditions, quartz consistently exhibits bulging recrystallization (BLG) at deformation temperatures of 280–400 °C, subgrain rotation recrystallization (SGR) at 400–500 °C, and large-scale grain-boundary migration recrystallization (GBR) at 500–700 °C (Hirth & Tullis 1992; Stipp et al. 2002; Tullis 2002; Stipp et al. 2010; Platt & Behr 2011a). Feldspar deforms by grain-scale brittle fracturing and cataclasis at temperatures ≤ 400–450 °C, and by internal microcracking, dislocation glide, minor dislocation climb, and localized BLG from 400–650 °C (Tullis & Yund 1987, 1991; Pryer 1993; Tullis 2002). SGR may be significant in feldspar at temperatures ≥ 500–550 °C, but unlike quartz deformation, occurs concurrently with microfracturing and BLG across a wide temperature range (Fitz Gerald & Stünitz 1993; Tullis 2002).

All three dynamic recrystallization mechanisms are produced by the migration of existing grain boundaries and the formation of new grain boundaries—new grains nucleate by either the BLG or SGR mechanisms, which consume original grains to produce low-strain, recrystallized grains. After nucleation, recrystallized grains grow by grain-boundary migration, which is driven by the strain energy ($\boldsymbol{\rho}$GBM) associated with dislocation gradients across grain boundaries, or the surface energy ($\boldsymbol{\gamma}$GBM) associated with grain-boundary topology (Platt & Behr 2011a). $\boldsymbol{\rho}$GBM increases the size of smaller grains at the expense of larger grains until the aggregate is fully recrystallized, at which point the action

of **ρ**GBM works to maintain the steady-state microstructure (Platt & Behr 2011a). **γ**GBM reduces surface energy between recrystallized grains by straightening curved grain boundaries until interfacial triple junctions approach 120° (Humphreys & Hatherly 2004; Platt & Behr 2011a). While **ρ**GBM bulges can migrate into and out of the same grain, **γ**GBM moves convex boundaries inward and concave boundaries outward—generally consuming smaller grains and increasing the size of larger grains (Platt & Behr 2011a). At lower stress and/or smaller grain sizes, **γ**GBM dominates and causes grain growth in the recrystallized matrix; while at higher stress and/or larger grain sizes, **ρ**GBM reduces grain-size variance by consuming original grains (Platt & Behr 2011a).

The criteria used to evaluate dynamic recrystallization microstructures and inferred deformation conditions are outlined in Table 6.1; temperature ranges are based on the experimental work of Hirth and Tullis (1992), and the natural studies of Stipp et al. (2002), Behr and Platt (2011), Platt and Behr (2011a, 2011b), and others.

6.1 Quartz microstructures

Quartz is pervasively recrystallized in all samples, and exhibits microstructures indicative of high-temperature SGR and GBR (Fig. 6.1). In porphyroclastic samples, dynamic recrystallization is not restricted to original grain boundaries, and moat structures characteristic of high-temperature BLG or low-temperature SGR are weakly developed, and highly localized. Ribbon grains consistently have internal subgrain structures with relatively straight cell walls and equant cell size (Fig. 6.1A, B, D), and exhibit internal recrystallization (Fig. 6.1A), or have been segmented by extensive recrystallization (Fig. 6.1C). In some cases, ribbons contain internal subgrain structures that have irregular boundaries and are locally overprinted by SGR, indicating they record an earlier episode of dynamic recrystallization (e.g. Fig. 6.1A, left side of ribbon grain; Fig. 6.1B, uppermost, light-colored porphyroclast; Fig. 6.1D). Recrystallized grains in all samples exhibit two or more sizes of grain-boundary bulges and often contain internal subgrain structures, suggesting the ostensibly new matrix also records more than one discrete phase of deformation. In general, recrystallized grains are similar in size to adjacent subgrains,

Table 6.1: Criteria used to evaluate dynamic recrystallization (DRX) microstructures in quartz, and inferred deformation temperatures.

DRX Mechanism	Deformation Temp. (°C)	Microstructures	Reference
BLG (280–400 °C)	280–390	- DRX restricted to original grain boundaries; - Original grain boundaries serrated due to small-scale bulging;	1, 3, 6 1, 2, 3, 4
	T ≃ 340	- Porphyroclasts are slightly elongate with patchy & undulose extinction;	1, 2, 4
	390–400	- Stable moat structures; - Patchy to irregular undulose extinction;	1, 6 1, 2, 4
Transition (390–420 °C)	T ≥ 390	- A few subgrains may develop within interiors of porphyroclasts;	1, 2
	T ≥ 400	- Rextlz'd grains are significantly larger than at previous temps;	1, 2, 4
SGR (420–500 °C)	T ≥ 420	- Polygonization of ribbon grains;	1, 2, 4
	420–490	- Sweeping undulose extinction;	1
	420–500	- DRX not restricted to original grain boundaries; - Size & shape of rextlz'd grains similar to that of internal subgrain structures; - Original grain boundaries have approximately straight edges; - Porphyroclasts transformed to elongate ribbon grains;	3, 4, 6 1, 2, 3, 6 1, 2, 4 1, 2, 5
	T ≥ 490	- Elongate ribbons + rextlz'd grains form oblique 2nd foliation; - Rextlz'd grains & internal subgrains ≃ same size/shape;	2, 5 3, 6
Transition (490–530 °C)	T ≥ 490	- Rextlz'd grains significantly larger at the SGR–GBR boundary (~120 μm); - Original grains may still exhibit internal subgrain structures near & slightly above SGR–GBR transition;	1, 5, 6 2
GBR (530–700 °C)	T ≃ 560	- Irregular, lobate to amoeboid grain shapes, sizes, and boundaries;	1, 2, 3, 6
	T ≥ 630	- α–β transition (P = 2.5–3.0 kb); - No original grains remain (i.e. fully rextlz'd); - Chessboard extinction (subgrain boundaries parallel to prism and basal planes);	1, 2, 5 1, 2, 4 5
Modified by ρGBM		- Boundaries of rextlz'd grains invaded by large-amplitude bulges;	3, 6
Modified by γGBM		- Boundaries of rextlz'd grains approaching straight, equant, 120° triple junctions;	3, 6

[1] Stipp et al. (2002)
[2] Tullis (2002)
[3] Humphreys & Hatherly (2004)
[4] Vernon (2004)
[5] Stipp et al. (2010)
[6] Platt & Behr (2011b)

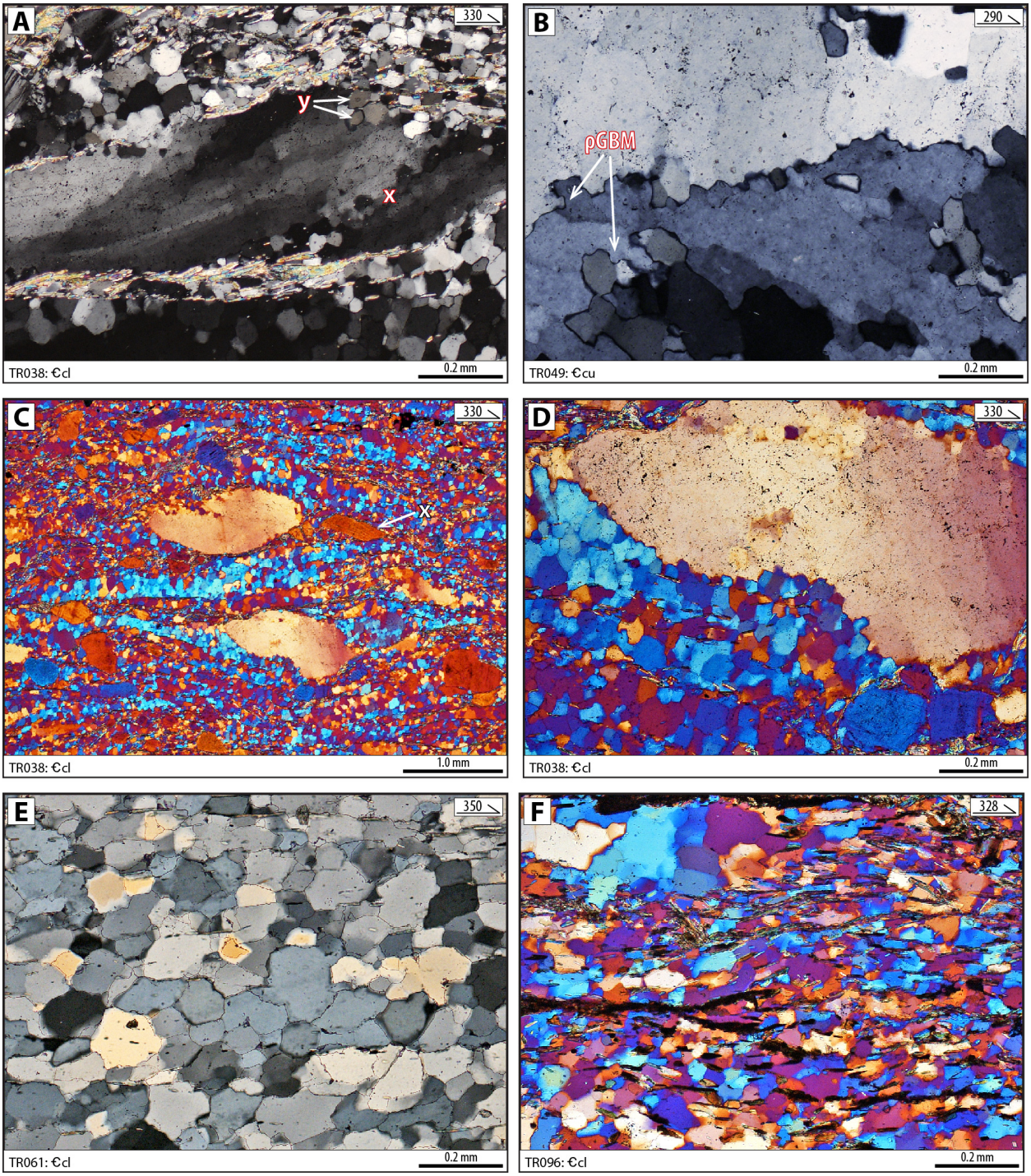

Figure 6.1: Deformation microstructures in quartz from the Tablerock thrust sheet. Sample number, map unit, and trend of L_1 are shown on each photomicrograph. All photos are cross-polarized light; C, D, and F also shown with gypsum plate. In general, deformation temperature increases from upper to lower photos. (A) Elongate ribbon grain with internal subgrain structure. X indicates region of low-angle subgrains similar in size and shape to high-angle recrystallized subgrains (Y). Camp Creek bridge, Blue Ridge Parkway. (B) Internal subgrain structure, recrystallized subgrains, and large-amplitude bulges produced by strain-driven grain boundary-migration (***ρ***GBM). Cross Creek Dr., Marion, NC. (C) Elongate ribbon grains (light-orange) are almost completely recrystallized (surrounding blue grains). X points to a semi-ductile, lozenge-shaped feldspar porphyroclast. (D) Enlarged view of lower light-orange ribbon grain in photo-C. Original part of ribbon grain has internal subgrain structure, blocky extinction, and grain boundaries significantly invaded by strain-induced bulges. (E) Quartz matrix fully recrystallized by GBR. Note the deeply sutured boundaries produced by **ρ**GBM. Bald Mountain Trail, Marion, NC. (F) Transposed F_1 fold; the boundaries of highly irregular grains form large-amplitude lobes indicative of GBR. Kistler Memorial Hwy., Linville Gorge Wilderness Area.

suggesting new grains nucleated by SGR. However, the irregular, lobate boundaries between recrystallized grains, as well as the extensive invasion of porphyroclast grain boundaries by large-amplitude bulges indicate dynamic recrystallization microstructures have been modified by ρGBM.

Samples of quartzite from the Shady Dolomite (Fig. 6.2F) and lower quartzite unit (Fig. 6.1E–F; Fig. 6.2E) are more than 90% recrystallized, and contain inequigranular aggregates of dynamically recrystallized grains with irregular, lobate grain boundaries. The deeply sutured boundaries and large grain size seen in TR061 (Fig. 6.1E) are characteristic of the transition from SGR to GBR near ~510 °C, while the amoeboidal structure of grains in TR043 and TR096 (and some regions of TR061) are indicative of the fast grain-boundary migration associated with GBR ≥ ~560 °C (Stipp et al. 2002, 2010). Porphyroclasts containing an earlier generation of internal subgrain structures often exhibit slightly block extinction that may represent weakly developed prism [c]+basal <a> "chessboard" extinction consistent with GBR at temperatures > ~630 °C (e.g. Stipp et al. 2010); the patchy and sweeping undulose extinction well-developed in all other porphyroclasts and ribbon grains is attributed to a late increment of strain.

6.2 Feldspar microstructures

Feldspar exhibits a range of brittle and semi-ductile behavior throughout the sample suite (Fig. 6.2): rigid porphyroclasts occur as isolated grains, crushed piles, and imbricated stacks; and commonly display patchy to sweeping undulose extinction, deformation lamellae, and kink bands. Brittle, grain-scale fracturing dominates feldspar deformation in all samples, and may be synkinematic with mylonite in sample TR038, where crushed piles of lozenge-shaped K-feldspar fragments are concentrated along small, foliation-parallel shear zones. Most feldspars have rounded grain boundaries, and approach fish-shapes in several samples (Fig. 6.1C; 6.2E). Localized BLG recrystallization occurs along high-stress, fractured grain boundaries in five of seven samples; in two of these samples, BLG is pervasive, and accompanies significant SGR recrystallization (Fig. 6.2E–F). Well-developed, polygonal subgrains also occur locally in samples without extensive SGR recrystallization, suggesting deformation in the Tablerock thrust sheet was high-grade enough to accommodate dislocation climb in feldspar (Tullis 2002). The

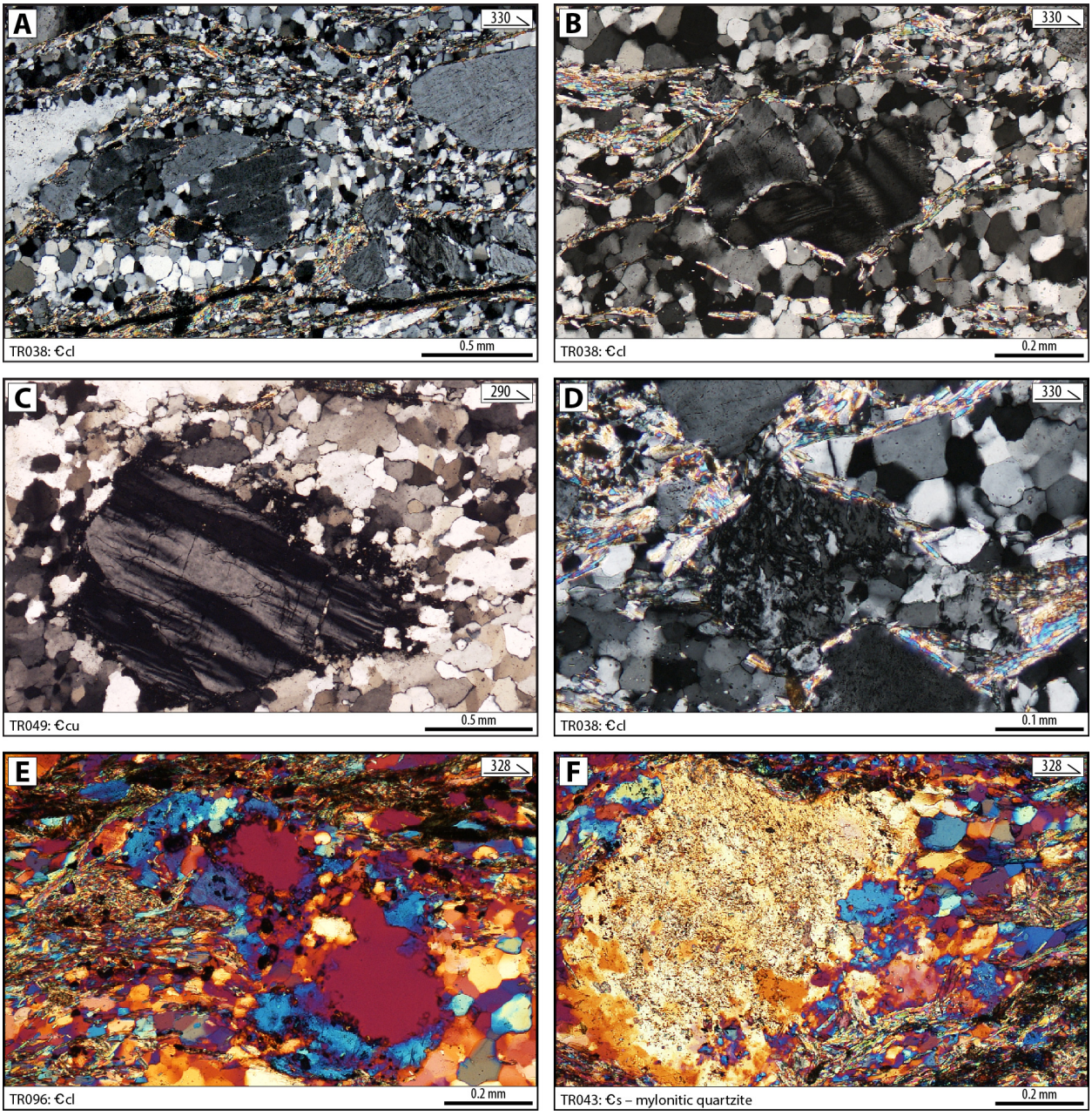

Figure 6.2: Deformation microstructures in feldspar from the Tablerock thrust sheet. Sample number, map unit, and trend of L_1 are shown on each photomicrograph. All photos are cross-polarized light; E and F also shown with gypsum plate. In general, deformation temperature increases from upper to lower photos. (A) Feldspar porphyroclasts with bookshelf-style shear fractures (left, center), and internal microkinks and shear fractures (crushed pile, lower right). Note the fine-grained region of BLG recrystallized feldspar above the bookshelf grain. Camp Creek bridge, Blue Ridge Parkway. (B) Grain-scale fractures, deformation lamellae, and kink bands in feldspar porphyroclast. (C) Tapering deformation twins. Cross Creek Dr., Marion, NC. (D) Partially recrystallized myrmekite on K-feldspar. (E) Extensive feldspar recrystallization by BLG and SGR. Kistler Memorial Hwy., Linville Gorge Wilderness Area. (F) Extensive feldspar recrystallization by BLG and SGR. US-221, Marion, NC.

occurrence of deformation-induced symplectite (i.e. myrmekite) in samples from the upper and lower quartzite units (Fig. 6.2D) is consistent with the conditions for active dislocation climb (Tullis & Yund 1987, 1991; Pryer 1993; Tullis 2002). However, myrmekite occurs only rarely in these samples, and may be ≤ 50 μm in diameter—suggesting they developed in extremely localized regions of high-stress; are only just starting to develop; or represent relics of recrystallized myrmekite. Given that myrmekite on K-feldspar can be recrystallized to a fine-grained quartz-plagioclase matrix at deformation conditions as low-grade as upper greenschist to lower amphibolite facies (e.g. Tullis 2002), partial recrystallization in the largest myrmekite lobes observed during this study is interpreted to indicate the latter suggestion.

The kinematic sense of shear was evaluated on the basis of fold vergence and asymmetry, porphyroclast tail-morphology, the orientation of mica fish, oblique grain-shape fabrics, and S-C microstructures (Table 7.1). All kinematic data were measured or derived from thin sections cut parallel to the L_1 lineation and perpendicular to the dominant, S_1 foliation. The degree of grain-shape obliquity was determined by measuring the long axes of 100–200 quartz grains across a minimum of five discrete regions per thin section. Because of the uncertainty introduced by folding, oblique grain-shape data from these samples are semi-quantitative, and therefore were not used to estimate kinematic vorticity (e.g. Xypolias 2009, 2010).

NW-vergent F_1 and F_2 folds, δ- and σ-type porphyroclast behavior, mica fish, NW-vergent oblique grain-shape fabrics (S_2), and the orientation of S-C structures consistently indicate top-to-NW shear sense throughout the Tablerock thrust sheet (Table 7.1). Antithetic microscale shear bands (i.e. bookshelf- or domino-type) are common in high-strain rocks, where progressive non-coaxial deformation was accommodated by shear fractures in rigid grains (Fig. 7.1C–D). Sigmoidal domains of recrystallized quartz aggregates bounded by C-type shear bands exhibit σ-type behavior (Fig. 7.1F), and apparent

Table 7.1: Summary of kinematic indicators used to evaluate shear sense in the Tablerock thrust sheet.

Unit & Sample	Shear Sense	Folds	Mineral Rotation	Oblique Fabric[1]	S-C Fabric
Shady Dolomite (Ꞓs)					
TR043	top–NW	F_1	δ- & σ-type – *porphyroclasts*	*too folded* [3]	S_1, S_2, S-C
Upper quartzite (Ꞓcu)					
TR002	top–NW	*none*	*none*	δ ≈ 56°	S_1, S_2
TR032	top–NW	F_1, F_2, F_3	δ-type – *porphyroclasts*	*too folded* [2]	S_1, S_2
TR049	top–NW	*none*	σ-type – *mineral fish*	δ ≈ 49°	S_1, S_2
Lower quartzite (Ꞓcl)					
TR038	top–NW	F_1, F_2, F_3	δ-type – *porphyroclasts*	*too folded* [2]	S_1, S_2
TR061	top–NW	*none*	δ-type – *mineral fish*	δ ≈ 34°	S_1, S_2, C
TR096	top–NW	F_1, F_2	δ-type – *quartz sigmoids*	δ ≈ 51°	S_1, S_2, S-C

[1] Mean grain-shape obliquity given; (δ) is the acute angle between S_1 and the long axes of matrix quartz grains (S_2).

[2] No consistent S_2 fabric; but long axes of recrystallized grains are axial planar to the latest folds represented in the sample.

[3] e.g. Xypolias (2009, 2010).

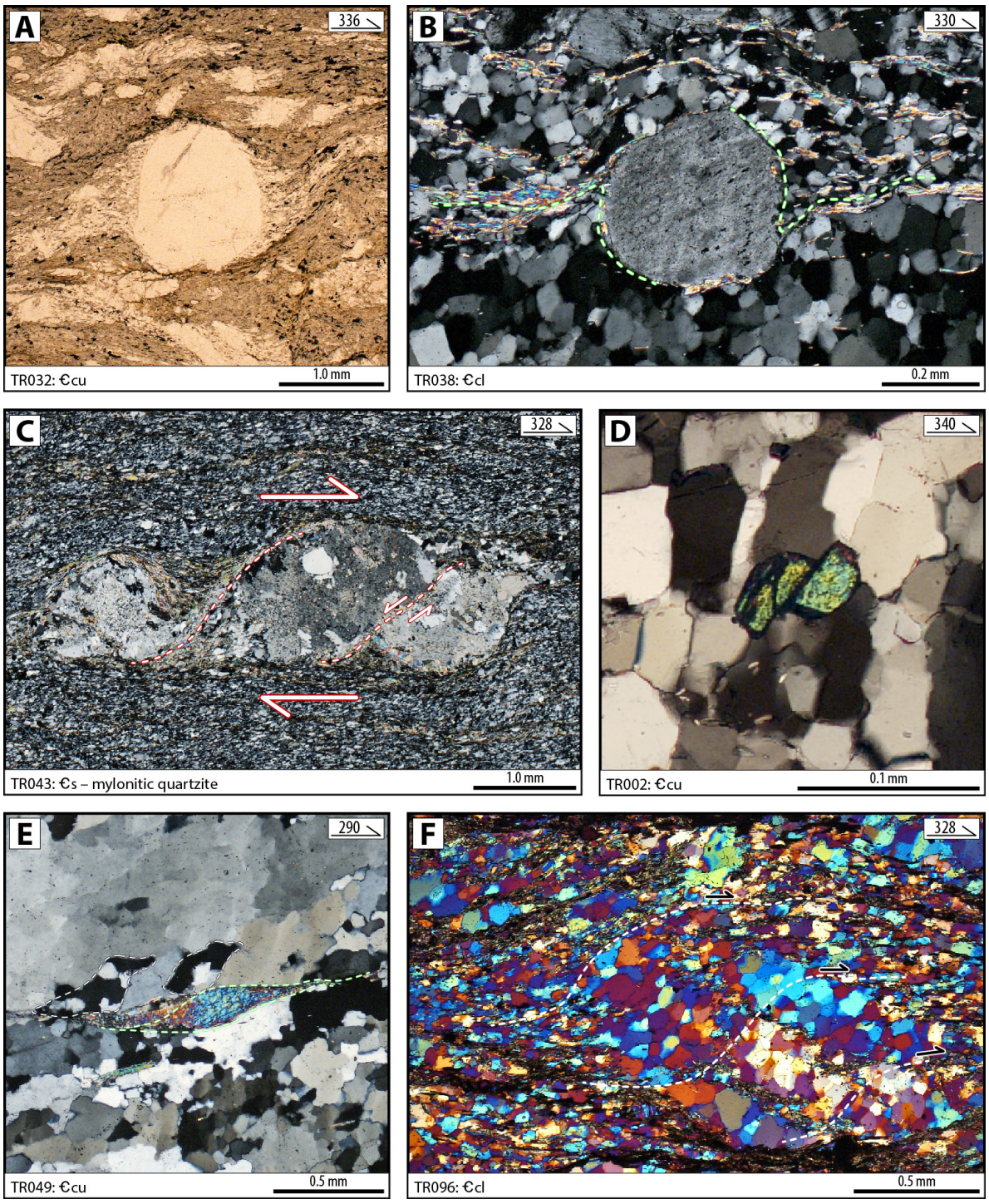

Figure 7.1: Summary of kinematic indicators in the Tablerock thrust sheet. Sample number, map unit, and trend of L_1 are shown on each photomicrograph. Photo-A is plane-polarized light; B–E are cross-polarized light; photo-F is cross-polarized light with gypsum plate. Shear sense is top-to-right in all cases. (A) δ-type rotated quartz porphyroclast. Upper Falls overlook, Blue Ridge Parkway. (B) δ-type rotated feldspar porphyroclast. Camp Creek bridge, Blue Ridge Parkway. (C) Saussuritized feldspar porphyroclasts with antithetic shear fractures and recrystallized quartz-feldspar-sericite tails; left-most grain exhibits δ-type rotation, while the central and right-most grains display σ-type tails. New roadcut along US-221 (e.g. Bozdog et al. 2012), Marion, NC. (D) Antithetic fracture through detrital zircon. Old Linville Rd., North Cove, NC. (E) Mica fish and oblique grain-shape fabric; white dashed lines indicate two small lozenges of recrystallized quartz exhibiting σ-type behavior. Cross Creek Dr., Marion, NC. (F) S-C fabric defined by sigmoids of recrystallized quartz bounded by fine-grained quartz, muscovite, and biotite. Kistler Memorial Hwy., Linville Gorge Wilderness Area.

domino- and δ-type (or back-rotated) behavior consistent with synkinematic S-C fabric in the limbs of F_1 folds (Fig. 7.2). Some of these sigmoids are overprinted by tension cracks oriented nearly perpendicular to bulk shear, placing the X-axis of finite strain subparallel to the shear direction (Fig. 7.2C). Oblique grain-shape fabrics in the Tablerock thrust sheet are defined by elongate porphyroclasts and ribbon aggregates, and the long axes of dynamically recrystallized quartz grains with respect to shear-zone boundaries and C-surfaces. Porphyroclasts and quartz ribbons are subparallel to the main foliation plane, and where recrystallized, contain an internal subgrain structure with the same weak to moderate obliquity developed in the dynamically recrystallized matrix. As such, original grains and ribbons likely represent an earlier increment of higher-strain deformation, while the matrix and internal subgrains record the latest, apparently lower-strain increment. The long axes of internal subgrains and recrystallized matrix in samples TR032 (c-cu) and TR038 (c-cl) are axial planar to F_2 folds, further supporting the above relationship.

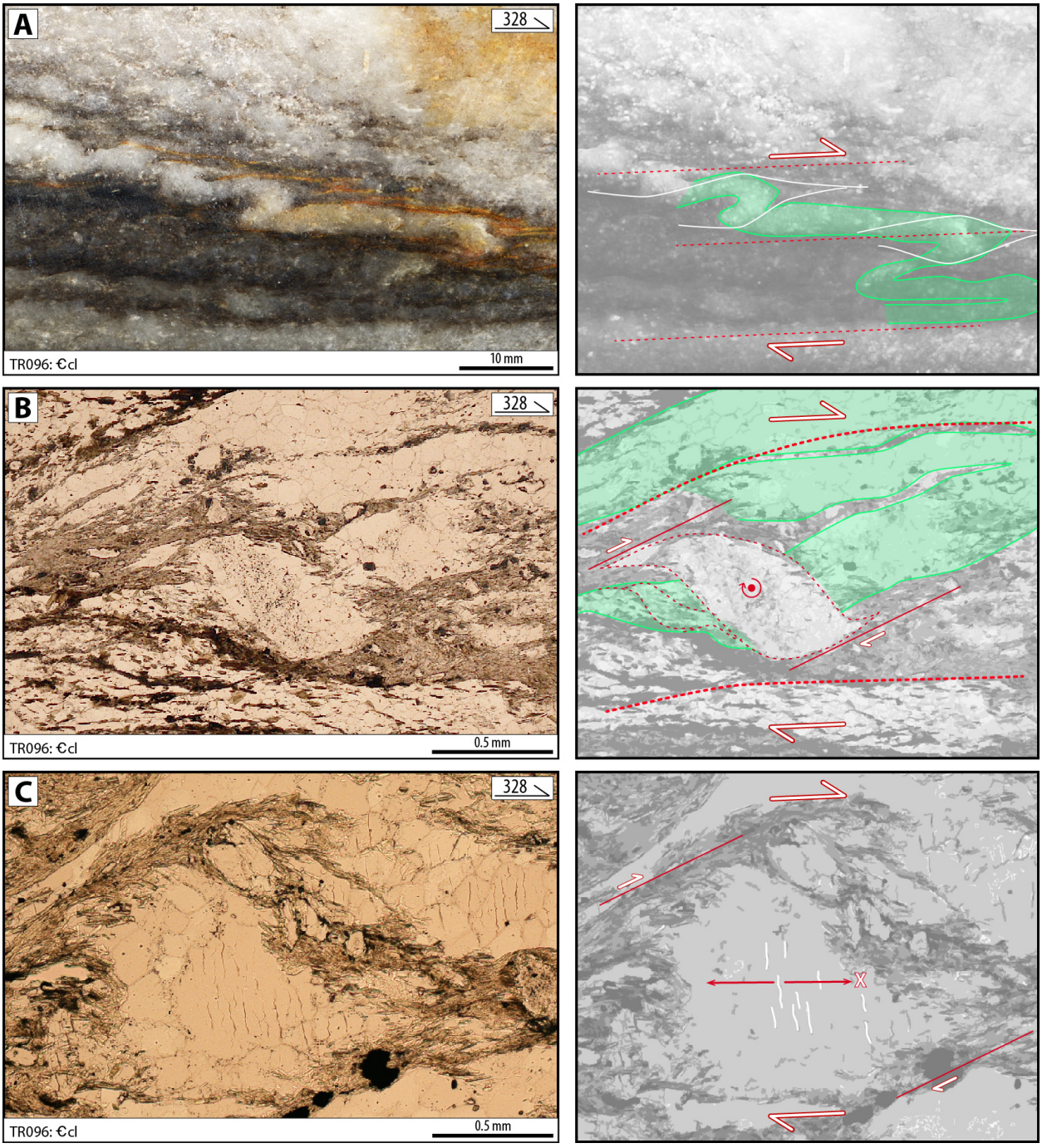

Figure 7.2: Synkinematic shear fabric in the limbs of F_1 folds in a sample of lower unit quartzite. Station number, map unit, and trend of L_1 are shown on each photo; right column are interpretations. Large white arrows indicate the dominant bulk shear sense, and small white arrows indicate localized sense of shear; green polygons highlight folds. Photos B and C are plane-polarized photomicrographs. (A) Photograph of TR096 hand sample showing NW-vergent F_1 folds. Red dashed lines indicate dominant C-planes and correspond to the large white arrows. White lines show S-planes developing around hinge zones. (B) Localized shear along S-planes (solid red lines, small white arrows) produced back-rotation of a partially recrystallized sigmoid of quartz aggregate on the limb of an intrafolial fold (sense of rotation indicated by red semicircle). (C) Tension cracks in recrystallized quartz sigmoids are nearly orthogonal to the dominant C-planes (large white arrows).

CHAPTER 8 | THERMAL INDICATORS

The estimated temperature of deformation for the Tablerock thrust sheet is based on metamorphic mineral assemblages, quartz lattice-preferred orientations (LPO), dynamic recrystallization microstructures, feldspar deformation microstructures, and the opening angles of quartz [c]-axis fabrics. Electron backscatter diffraction (EBSD) patterns were collected and indexed from four samples using a Philips X-MAX 30 environmental scanning electron microscope (E-SEM), and HKL CHANNEL 5 post-processing software at the Jackson School of Geosciences Electron Microbeam Laboratory, University of Texas–Austin. E-SEM analysis was conducted with a 30 kv beam, 6 µm spot size, and 70° tilt-correction. Indexed Kikuchi bands with mean angular deviations < 1.0° were selected to construct pole figures in HKL CHANNEL 5 with 15° half-widths and 5° data clusters.

8.1 Metamorphic mineral assemblages

Previous studies by Bryant and Reed (1969, 1970) and Trupe (1997) reported greenschist facies metamorphic conditions for the Tablerock thrust sheet. However, the discovery of local, accessory to trace amounts of sillimanite in rocks of the upper and lower quartzite units suggests higher-temperature conditions prevailed for at least part of the thrust sheet's deformation history. Similar occurrences of fibrolitic sillimanite containing segregations of quartz, feldspar, and ilmenite have been reported in amphibolite facies shear zones in the Lachlan fold-thrust belt, eastern Australia (e.g. Vernon 1979); the Rhodope orogen, central Bulgaria (e.g. Georgieva et al. 2002); and the Higher Himalayan crystalline sequence, Khumbu region, Nepal (e.g. Musumeci 2002). At these locations, the formation of sillimanite is attributed to fluid-assisted, retrograde biotite and muscovite oxidation reactions facilitated by continuous ductile and brittle-ductile deformation, and attendant fluid circulation (Foster 1977; Vernon 1979; Georgieva et al. 2002; Musumeci 2002). Mobile, ion-rich fluids destabilize many metamorphic silicate minerals, resulting in the nucleation of whichever aluminum silicate polymorph is most energetically suited to the prevailing conditions; in small-scale and/or localized reaction sites, sillimanite may be favored over andalusite and kyanite because of the extremely fine grain size at which its acicular

and fibrous habits nucleate (Vernon 1979). The presence of fibrolitic sillimanite in rocks of the Tablerock thrust sheet indicates deformation reached lower to middle amphibolite facies conditions at temperatures ≥ ~550 °C (e.g. Georgieva et al. 2002; Musumeci 2002).

Because this is the first detailed study to focus on the interior of the Tablerock thrust sheet, and because the sillimanite occurrences are small and localized, this finding may not contradict the lower-temperature estimates of earlier workers, who simply may not have encountered sillimanite-bearing units. Additionally, the occurrence of biotite in samples of Shady Dolomite (TR043), the upper quartzite unit (TR049), and the lower quartzite unit (TR038, TR061, TR096) is consistent with the findings of previous workers, and places their temperature estimates at the upper end of greenschist facies conditions, only 100–120 °C lower than minimum estimates for the sillimanite-bearing rocks of this study.

8.2 Lattice-preferred orientations of quartz

Slip in a covalent crystal lattice occurs along the planes of densest atomic packing, and in directions of highest linear density (Humphreys & Hatherly 2004; Karato 2008). Close-packed coordinations produce the lowest energy-configurations because they provide the shortest bond lengths and lowest bond energies between neighboring, intraplanar atoms, and the longest (i.e. weakest) bond lengths between stacked planes (Humphreys & Hatherly 2004). Because crystal faces tend to develop parallel to the densest-packed planes (e.g. the Law of Bravais), the plane and vector of crystallographic slip in a lattice are specified by their Miller indices, or the Miller indices of symmetrically equivalent systems (Hull & Bacon 2011).

In quartz, slip is observed by measuring the relative orientations of [c] and <a> crystallographic axes using EBSD analysis or U-stage microscopy, and plotting their distributions in stereographic space; the resulting point data cluster into different maxima characteristic of the slip systems active during deformation (Fig. 8.1; Table 8.1). At low to medium temperature conditions, quartz [c]-axes record <a>-directed slip on (0001) basal pinacoids, secondary $\{11\bar{2}0\}$ rhomb prisms, and $\{10\bar{1}0\}$ hexagonal prisms; these are referred to as the basal <a>, rhomb <a>, and prism <a> slip systems, respectively. At medium to high temperatures, [c]-axes record prism <a> and rhomb <a> slip; and at the highest

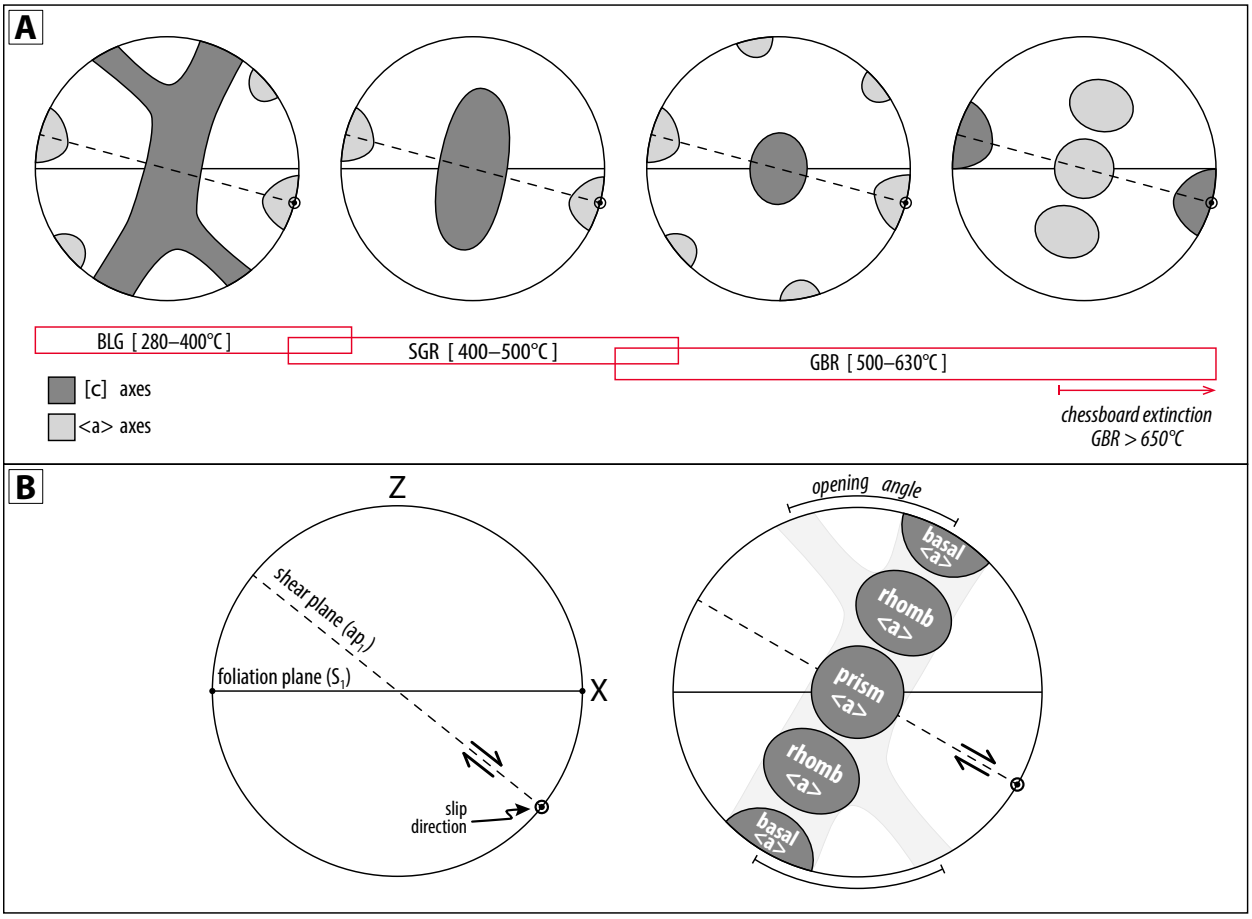

Figure 8.1: Simplified relationships between dynamic recrystallization microstructures, quartz LPO patterns, inferred slip systems, and deformation temperature. BLG is the bulge recrystallization mechanism; SGR is subgrain rotation recrystallization; GBR is grain boundary migration recrystallization. X and Z are directions of finite strain (Y points into the page at the center of the stereonet). (A) Idealized quartz LPO patterns formed at different temperatures during non-coaxial deformation. Overlapping boxes represent transition zones between the BLG, SGR, and GBR mechanisms. Chessboard extinction is produced by the combined activities of prism [c] and basal <a> slip systems. (B) Idealized locations of [c]-axis maxima produced by the activity of different slip systems. The inferred shear plane (i.e. flow plane) corresponds to an extensional apophysis (ap_1) of the flow. After Twiss and Moores (1992); Langille et al. (2010b); Xypolias 2010; Singleton and Mosher (2012).

Table 8.1: Summary of quartz [c]-axis LPO patterns produced by thermally activated slip systems.

DRX Mechanism	Deformation Temperature	Lattice-Preferred Orientation (LPO) Patterns	Slip Systems[1]
BLG	280–400° C	multi-system (single girdles; crossed-girdles)	basal <a>[2] / basal+rhomb+prism <a>
–transition–	390–420° C	multi-system (single girdles; crossed-girdles)	basal <a>[2] / basal+rhomb+prism <a>
SGR	420–500° C	multi-system (single girdles; crossed-girdles)	basal+rhomb+prism <a>
–transition–	490–530° C	single Y-maximum	prism <a>
GBR	530–700° C	T < 630° → single Y-maximum T = 630° → α–β transition[3] T > 630° → secondary maxima T > 650° → chessboard extinction	prism <a> prism <a> + prism [c] prism <a> ± prism [c] prism [c] + basal <a>

[1] Slip systems listed in order of dominance (Stipp et al. 2002; Tullis 2002);
[2] Porphyroclasts and ribbon grains exhibit basal <a> slip independent of temperature up to 500–550° C (Stipp et al. 2002);
[3] Transition between α and β quartz polytypes; Kruhl (1996) attributed chessboard extinction to this transition.

temperatures, slip on prism planes occurs in the [c]-direction (Fig. 8.1A, far right pole figure). Below ~550 °C, porphyroclasts exhibit temperature-independent basal <a> slip, which is thought to be responsible for the formation of elongate ribbon grains (Stipp et al. 2002). The distribution of quartz <a>-axes normal to $\{11\bar{2}0\}$ secondary rhombic prism planes and $\{10\bar{1}0\}$ hexagonal prism planes (Fig. 8.2; Fig. 8.3) was used to clarify the interpretations of equivocal [c]-axis patterns. Additionally, the arc between small circle legs of [c]-axis cross-girdle LPO patterns (i.e. the opening angle) tends to increase during dynamic recrystallization with increasing temperature and decreasing strain rate (e.g. Platt & Behrman 1986; Kruhl 1996, 1998; Law et al. 2004; Langille et al. 2010a), and can be used in the Kruhl (1998) geothermometer to estimate deformation temperature:

$$T \pm 50\ °C = [\ (o.a. - 11.27) / 0.1032\ ] \qquad (1)$$

At experimental conditions, plastic deformation in quartzite orients the central girdle of [c]-axis fabrics orthogonal to the shear plane during simple shear, and orthogonal to the XY-plane of finite strain during pure shear (Platt & Behrman 1986). The shear plane is a material or particle line of no angular velocity (i.e. an apophysis of the flow), and is approximated by a line perpendicular to the central [c]-axis girdle in quartz LPO (Fig. 8.1b) (Platt & Behrmann 1986; Xypolias 2009; Langille et al. 2010b). The acute angle

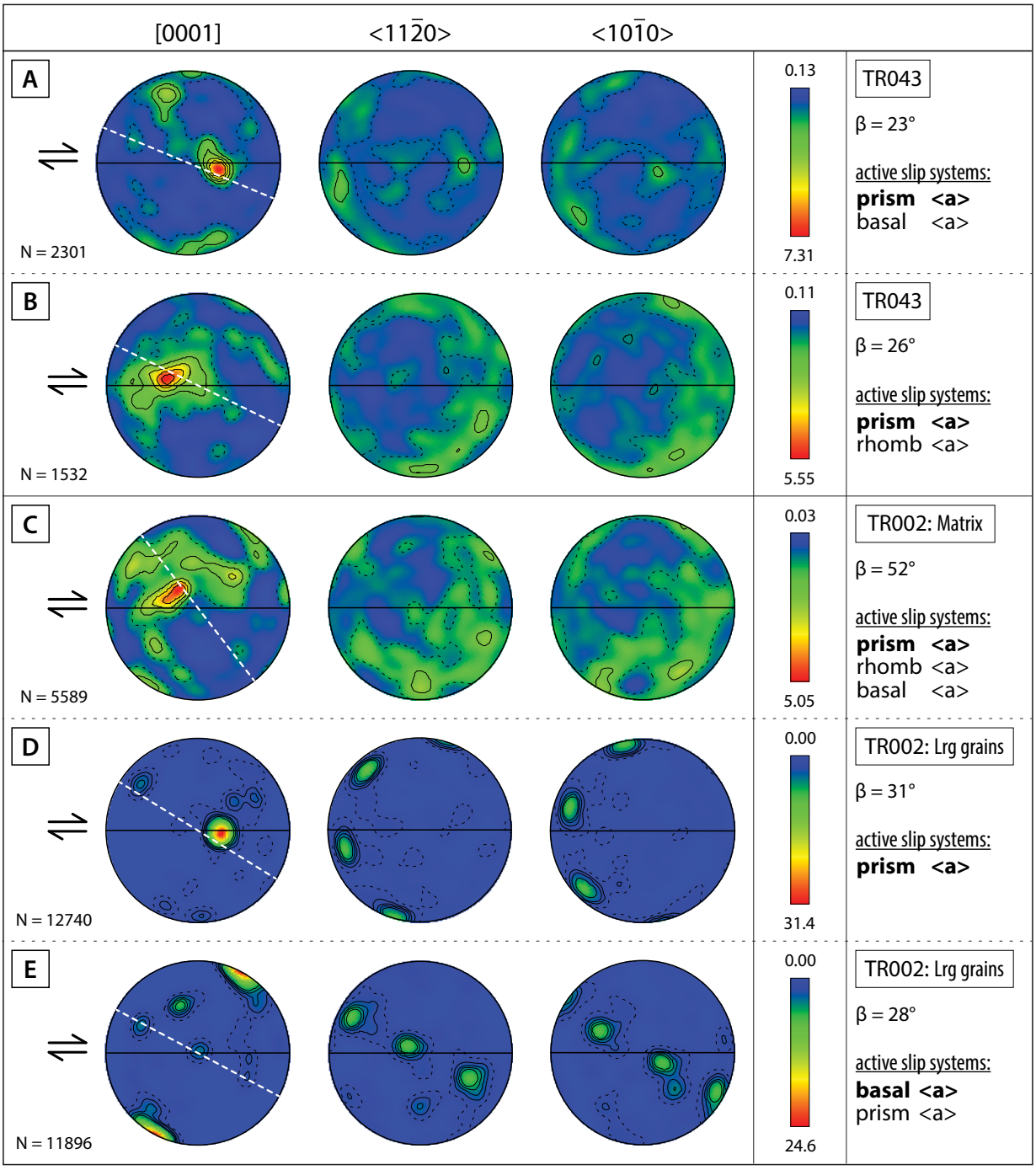

Figure 8.2: EBSD pole figures for samples of Shady Dolomite (Ꞓs) and the upper quartzite unit (Ꞓcu). Sample numbers are listed in far right column, along with the acute angle between the foliation and flow planes (β), and the dominant active slip system (bold); additional slip systems are listed in order of LPO strength. Colors correspond to multiples of uniform density (m.u.d.); maximum and minimum m.u.d. given in center column. White dotted lines are inferred flow planes. Shear sense is top-NW in all cases (shown here as top-Right). Left column of pole figures corresponds to [c]-axes; center and right columns correspond to the two unique <a>-axes. (A) & (B) Phyllonitic quartzite from the Shady Dolomite. US-221 roadcut, Marion, NC. (C) Bulk recrystallized matrix for a mature quartzite from the upper unit. Old Linville Rd., North Cove, NC. (D) & (E) Large (Lrg) grains are original quartz porphyroclasts.

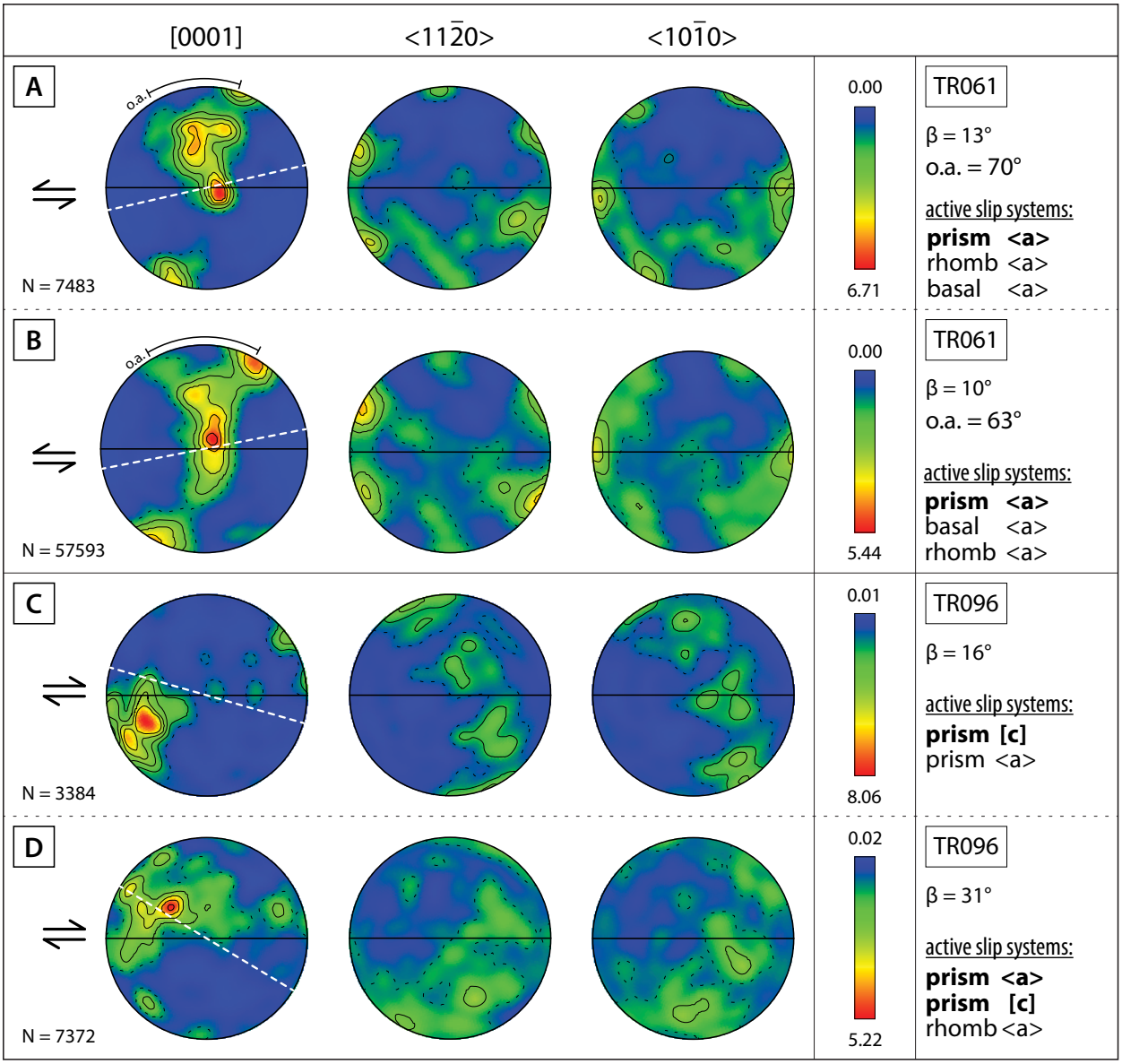

Figure 8.3: EBSD pole figures for rocks of the lower quartzite unit (Ɛcl). Sample numbers are listed in far right column, along with the acute angle between the foliation and flow planes (β), and the dominant active slip system (bold); additional slip systems are listed in order of LPO strength. Where measured, o.a. is opening angle. Colors correspond to multiples of uniform density (m.u.d.); maximum and minimum m.u.d. given in center column. White dotted lines are inferred flow planes. Shear sense is top-NW in all cases (shown here as top-Left for TR061, top-Right for TR096). Left column of pole figures corresponds to [c]-axes; center and right columns correspond to the two unique <a>-axes. (A) & (B) Interlayered quartzite, phyllite, and metasiltstone. Bald Mountain trail, Marion, NC. (C) & (D) Interlayered quartzite, phyllite, and metasiltstone, similar to TR061, but folded. Kistler Memorial Hwy., Linville Gorge Wilderness Area.

(β) between the main foliation plane (XY) and the line perpendicular to the central [c]-axis girdle is inferred to be the angle between the extensional apophysis (ap_1) and the X-axis of finite strain (Platt & Behrmann 1986; Wallis 1995; Xypolias 2009).

All samples used for EBSD analysis exhibit complex, but relatively well-developed quartz LPO patterns with [c]-axis concentrations > 5 times the multiples of uniform distribution (m.u.d.) (Fig. 8.2; Fig. 8.3). The [c]-axis LPO patterns of six of nine analyses form dominant Y-maxima consistent with prism <a> slip; of these, 5 analyses include variable contributions by rhomb <a> and/or basal <a> slip. In sample TR002, the LPO patterns for original grains with well-developed internal subgrain structures are dominated by prism <a> slip characteristic of recrystallization at the SGR–GBR transition (490–530 °C), or by GBR at temperatures < ~550 °C (Fig. 9.2D). Sample TR002 LPO for original grains with weak subgrain structures exhibit basal <a> patterns, suggesting slip in these grains occurred primarily by temperature-independent dynamic recrystallization at temperatures < ~550 °C (Fig. 8.2E); minor prism <a> slip may be related to recrystallized subgrains, or the adjacent matrix. Sample TR061 is transitional between asymmetric cross girdles and single girdles inclined toward the inferred shear direction—consistent with recrystallization by the SGR mechanism or during the SGR–GBR transition at temperatures 450–530 °C (Fig. 8.3A–B); the average deformation temperature estimated from the sample's well-defined opening angles is 550 ± 50 °C. The point maxima in LPO patterns from TR096 are clustered near the intersection of the primitive and the inferred X-axis, suggesting they represent a transition between, or combination of prism <a> and prism [c] slip during GBR at temperatures 530–630 °C (Fig. 8.3C–D); the distribution of $<11\bar{2}0>$ and $<10\bar{1}0>$ <a>-axis patterns in a girdle nearly orthogonal to [c]-axis maxima in one case (Fig. 8.3C), and along the primitive in the other (Fig. 8.3D), is consistent with prism [c] + prism <a> and prism <a> + prism [c] slip, respectively.

8.3 Combined results

The coexistence of sillimanite inclusions, myrmekite, and ductile feldspar with lower-temperature quartz microstructures, slip systems, and brittle feldspar in samples TR002 and TR038 is attributed to overprinting relationships between two distinct phases of tectonometamorphic deformation during

emplacement of the Tablerock thrust sheet (Fig. 8.4). Despite the relative paucity of sillimanite in these two samples, the feldspar microstructures indicate higher temperature ranges than do the quartz microstructures, suggesting an earlier deformation phase with T > ~550 °C was overprinted by a later phase of pervasive quartz recrystallization at T < ~550 °C. Microstructures in other samples are also consistent with a composite deformation history, including internal subgrain structures modified by ρGBM, and overprinted by later dynamic recrystallization (Fig. 6.1A, B, D); multiple sets of grain-boundary bulges of different sizes; dynamically recrystallized matrix grains with internal subgrain structures; complex quartz LPO patterns (Fig. 8.2; Fig. 8.3); and the large opening angles of [c]-axis cross girdles in the quartz fabrics of sample TR061 (Fig. 8.3A–B). Considered collectively, geothermometers in the sample suite indicate the earlier deformation phase reached lower–middle amphibolite facies conditions at 550–595 °C, while the later phase reached upper greenschist to lower amphibolite facies conditions at 465–550 °C.

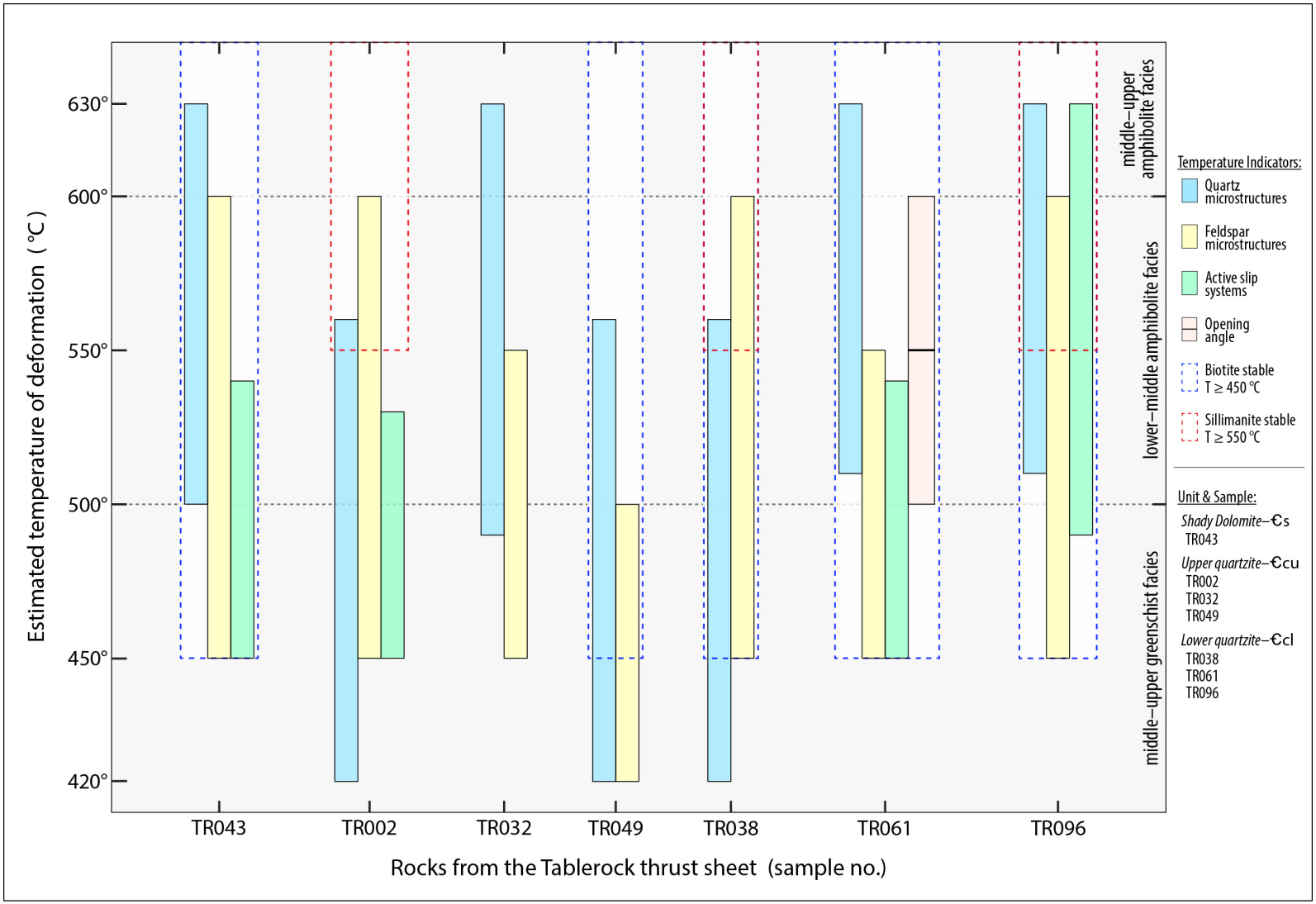

Figure 8.4: Summary of thermal indicators in samples from the Tablerock thrust sheet. Bars represent the temperature ranges indicated by each thermal gauge. Metamorphic mineral assemblages (biotite and sillimanite) and deformation microstructures were determined by thinsection microscopy; active slip systems were interpreted from EBSD pole figures (see Fig. 9.2 and 9.3). The opening angle of quartz [c]-axis fabrics (TR061) was derived from EBSD pole figures, and used to calculate the estimated deformation temperature ± 50° C with the geothermometers of Law et al. (1990) and Kruhl (1996, 1998); black line within the bar indicates the calculated temperature, and the bar indicates the range of the confidence interval. Dashed lines illustrate biotite (blue) and sillimanite (red) stability fields for the temperature space covered by the graph.

CHAPTER 9 | SYNTHESIS

9.1 Map-scale sheath folds

Fabrics and deformation structures throughout the Tablerock thrust sheet indicate that large, NW-trending folds at Indian Rock Trail, Linville Falls waterfall (Fig. 9.1), Woodlawn quarry, Linville Gorge Wilderness Area, and in roadcuts along US-221 are consistent with culminations on map-scale sheath folds. Outcrop patterns mapped by Bryant and Reed (1970) (Fig. 9.2), and possible kilometer-scale NW-trending folds visible in satellite images (Fig. 9.3) exhibit strikingly similar geometries and structural trends to F_1 structures throughout the thrust sheet, and therefore may also be consistent with map-scale sheath folds (Walker & Hatcher 2012b). Additionally, some or all of the small horses at the southwest end of the thrust sheet may be map-scale sheath folds, or may have developed from them (Fig. 9.2).

9.2 Simplified, conceptual model for the emplacement of the Tablerock thrust sheet

Stage 1—Thrust sheet formation and initial structural evolution:
Fold-related fault propagation beneath the Blue Ridge-Piedmont megathrust sheet removed a large horse of Shady Dolomite and Chilhowee Group rocks from the footwall.

Folds, lineations, and foliations in the Tablerock thrust sheet have similar geometries and structural orientations to those of the overriding Blue Ridge-Piedmont megathrust sheet, suggesting the two thrust sheets share similar deformation histories (Bryant & Reed 1970; Trupe 1997; Walker & Hatcher 2012b). Rocks inside the window are also overprinted by the L_1 transport lineation and NW-vergent/NE-trending crenulations; but unlike the Tablerock thrust sheet, rocks in the Grandfather Mountain Formation have not been transposed, and are instead truncated by the overriding Tablerock and Blue Ridge-Piedmont thrust sheets (Bryant & Reed 1970; Boyer 1978; Trupe 1997). In addition, nearly compete transposition, pervasive sheath folding, and upper greenschist to middle amphibolite facies deformation conditions in the Tablerock thrust sheet suggest the Tablerock thrust sheet was coupled with, and deformed along the base of the Blue Ridge-Piedmont megathrust sheet, where it accumulated a large amount of strain before arriving at its present location.

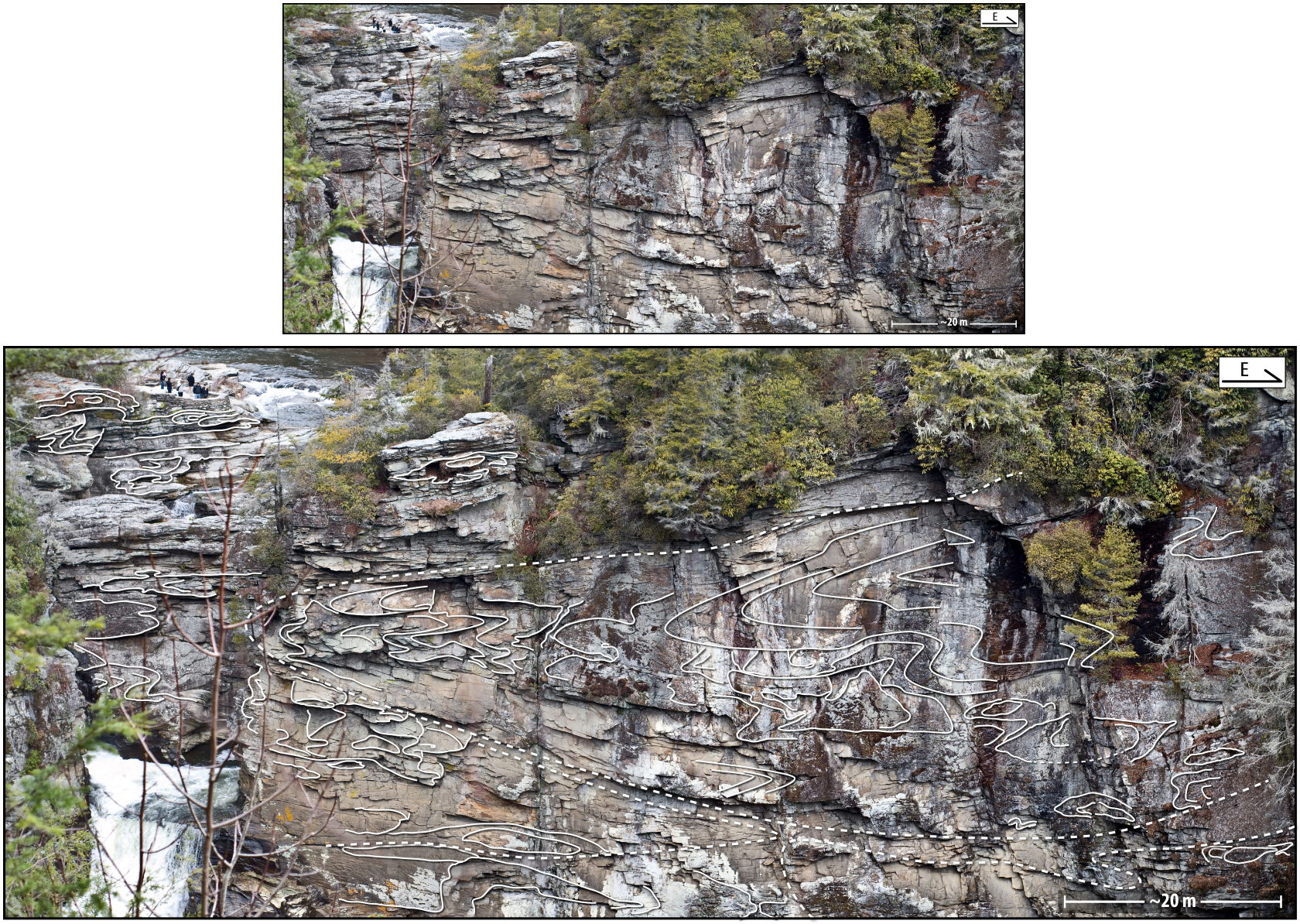

Figure 9.1: Linville Falls sheath folds. View of Linville Falls waterfall from Chimney overlook (top photo), and interpretive sketches (lower photo). Upper Falls over look is visible in upper left corner of photos (see people for reference). Dashed lines approximate enveloping surfaces of possible km-scale sheath folds.

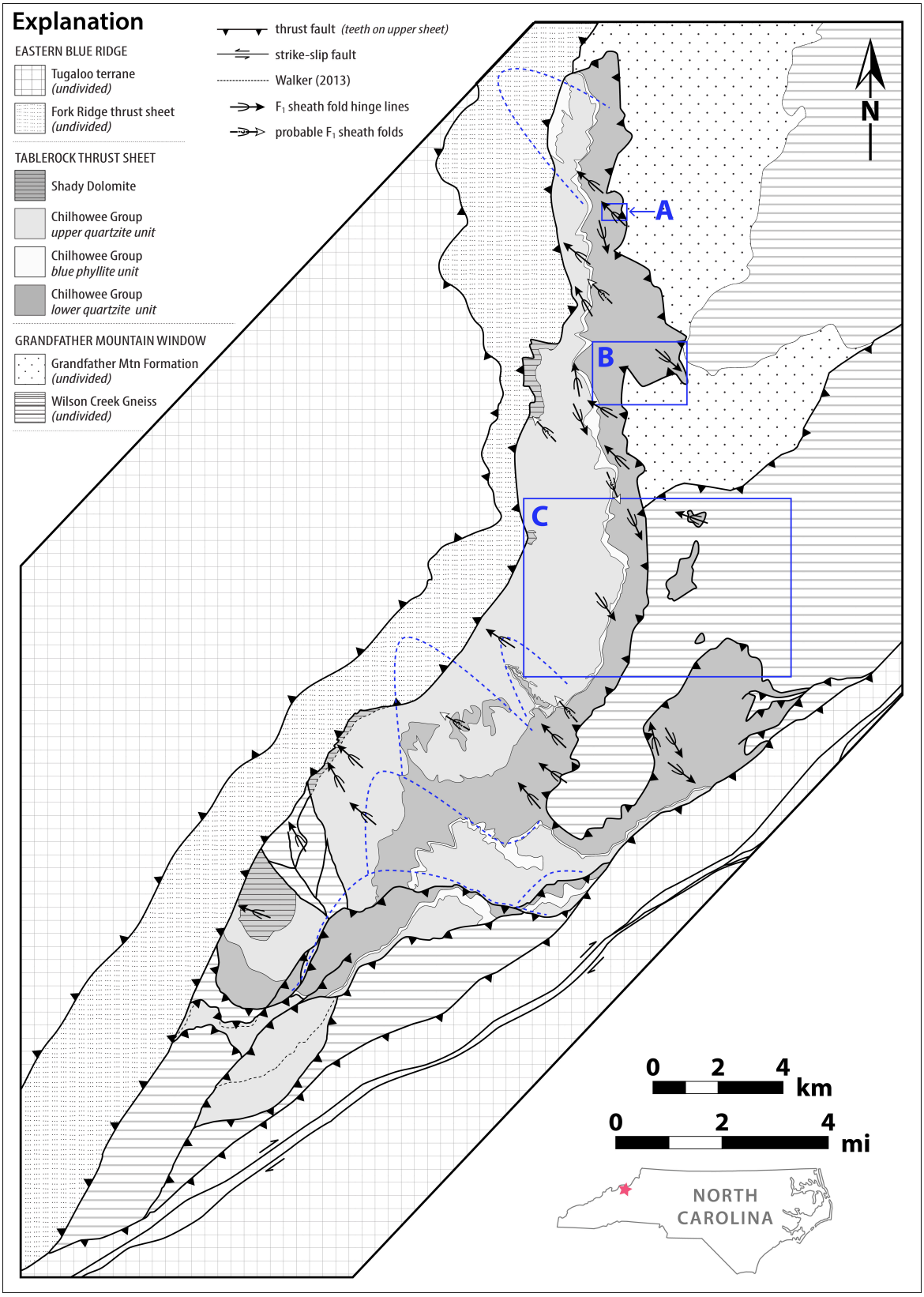

Figure 9.2: Location of definitive, probable, and possible sheath folds. Depicted sheath folds are representative, and signify the occurrence of sheath folds rather than the actual quantity observed. Blue boxes are the approximate areas magnified in satellite images shown in Fig. 9.3. Blue dashed lines illustrate possible map-scale sheath folds, as estimated from the map patterns of Bryant and Reed (1970), and supported by field data from this study.

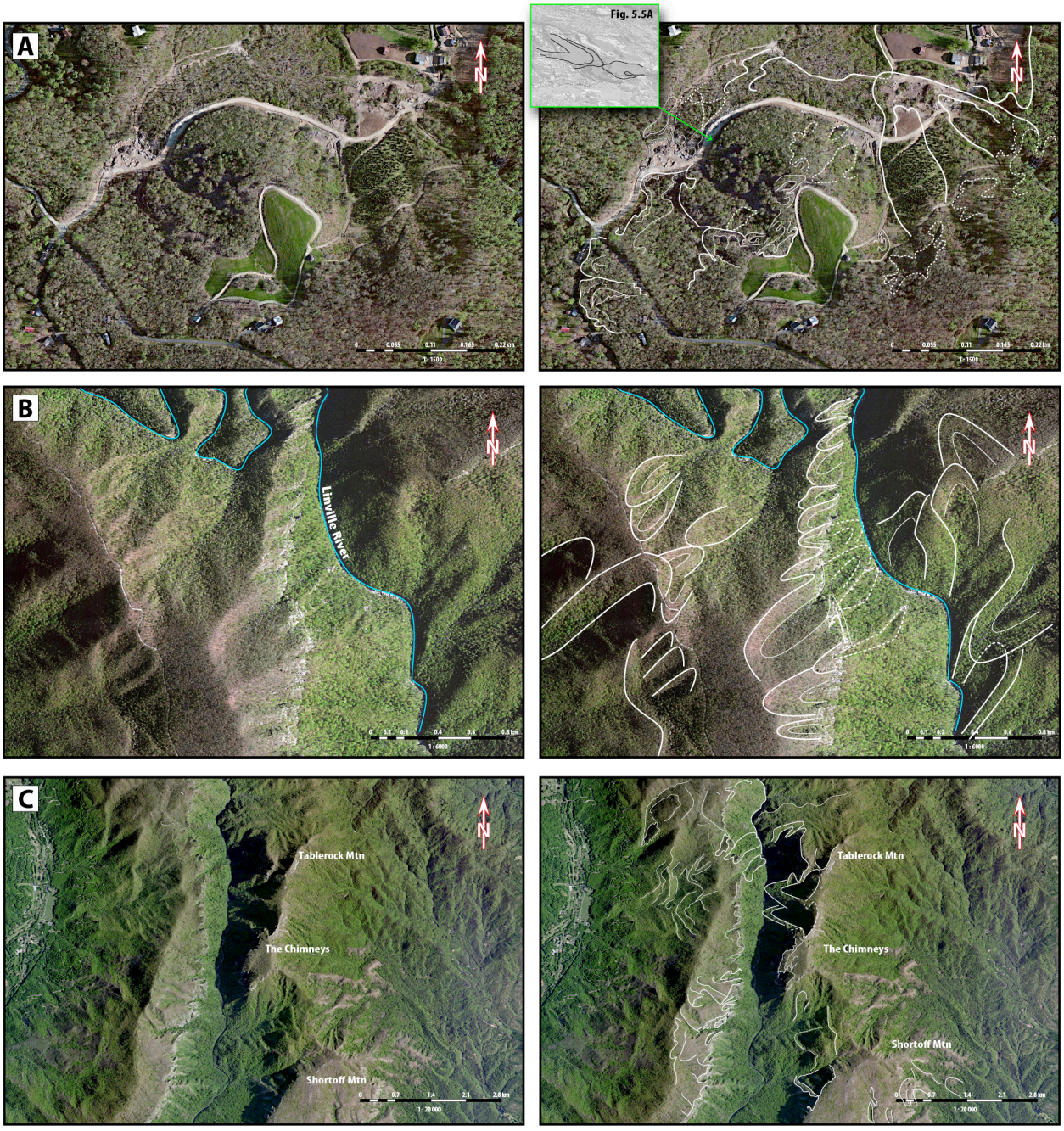

Figure 9.3: Possible map-scale sheath folds in the Tablerock thrust sheet. Left column shows NASA Blue Marble satellite images at three different scales (Fig. 9.1 for map locations). Right column shows schematic interpretations of possible map-scale sheath folds. (A) Location corresponds to station TR013 near Jonas Ridge, NC. Inset shows location of large mesoscale sheath folds observed during this study. (B) Location is just S–SE of Linville Falls waterfall along the eastern rim of Linville Gorge. The Linville River is highlighted blue for reference. (C) Image shows the eastern rim of Linville Gorge, two klippen (Tablerock Mountain and The Chimneys), and the semi-detached piece that makes up Shortoff Mountain.

Type-F (fold-related) thrust sheets (e.g. Hatcher & Hooper 1992) and fold-nappes form megascopic sheath folds at the bases of many large thrust sheets, including those of the Cabo Ortegal complex, northwest Spain; Tambo nappe, central Swiss Alps; Dumbara syncline, Sri Lanka; and the Shimanto accretionary complex, Japan (Azcárrga et al. 2002, and references therein; Searle & Alsop 2007). Pervasive transposition (S_1) and sheath folding (F_1) in the Tablerock thrust sheet is attributed to a similar process of fold-related faulting and subsequent transport along the base of the Blue Ridge-Piedmont megathrust sheet. Folding may have nucleated around perturbations in bedding during transport (e.g. Alsop & Holdsworth 2002; Reber et al. 2012, 2013a, b), or by the rotation and tightening of folds associated with strain in the footwall prior to faulting (e.g. Alsop 1992; Carreras et al. 2005; Alsop & Carreras 2007). The early, high-temperature phase of deformation indicated by sillimanite-bearing metamorphic mineral assemblages, SGR–GBR microstructures, and prism <a> dominated quartz fabrics is consistent with deformation conditions in the known occurrences of sheath folds along the bases of the sheets mentioned above.

The association of the Grandfather Mountain Formation with a failed rifting event, as well as its highly variable thickness suggest it was deposited in a basin that subsided rapidly, but unevenly along strike. The great thickness of Chilhowee Group rocks in the Tablerock thrust sheet, as compared with all other known exposures, could likewise be a product of deposition in locally deep sub-basins, fault propagation through thicker sections deposited near the shelf edge break, or some combination thereof. Alternatively, thickening of fold hinges and limbs during map-scale sheath folding and emplacement as a Type-F thrust sheet could potentially account for the greater thickness of Chilhowee Group rocks in the Tablerock thrust sheet.

Stage 2—Emplacement of the Tablerock thrust sheet:

The Tablerock thrust sheet effectively docked at the failed-rift basin containing the Grandfather Mountain Formation, and is decoupled from the Blue Ridge-Piedmont megathrust sheet as the master detachment steps down.

Whether tectonically inverted or not, an aulacogenic rift basin, like the one containing the Grandfather Mountain Formation, could easily increase the dip angle along a detachment enough to promote

duplexing in the footwall (Boyer & Elliott 1982; Mitra & Boyer 1986; Konstantinovskaya & Malavieille 2011). After reaching the Grandfather Mountain basin, the Tablerock thrust sheet may have accommodated the first increments of strain associated with steeper dip along the Blue Ridge-Piedmont detachment by decoupling from the overriding thrust sheet. NE/SW-trending F_2 open folds and crenulations could have been produced after the master detachment stepped down to imbricate the underlying window rocks. The onset of the lower-temperature phase of deformation in the Tablerock thrust sheet is attributed to progressively decreasing deformation and temperature conditions associated with cratonward transport of the Blue Ridge-Piedmont megathrust sheet over the Laurentian margin.

Stage 3—Duplex formation:

Continued movement of the Blue Ridge-Piedmont megathrust sheet imbricated underlying Grandfather Mountain Formation rocks and basement gneisses, which arch into an antiformal stack duplex.

Large displacements along individual imbricates caused the branch lines of each thrust sheet to cluster and form an antiformal stack (Boyer 1978; Boyer & Elliott 1982; Mitra & Boyer 1986). F_3 folds and flexures are attributed to this stage, as is the formation of diffuse zones of cataclastic deformation in thrust sheets above the Tablerock thrust sheet (e.g. Bryant & Reed 1970; Trupe 1997); both features could have formed during the final phase of stage-2, throughout stage-3, or during both.

1. Sheath folding is substantially more prevalent in the Tablerock thrust sheet than previously recognized. Sheath folds were observed at centimeter- through kilometer-scale, and occur throughout the interior of the thrust sheet as well as in fault zones. Extensive transposition, colinearity between F_1 and L_1, and the occurrence and orientation of mesoscale sheath folds suggests meter- to kilometer-scale folds at Indian Rock Trail, Linville Falls waterfall, Woodlawn quarry, Linville Gorge Wilderness Area, and in roadcuts along US-221 are culminations on map-scale sheath folds. The occurrence of ductile to semi-ductile asymmetric boudins, asymmetric porphyroclast tails, SC fabrics, and oblique grain-shape fabrics suggest sheath folds formed during bulk simple shear or non-coaxial general shear, rather than bulk pure shear.

2. Extensive transposition and intrafolial sheath folds in the Tablerock thrust sheet, and the lack of transposition and sheath folding in rocks of the Grandfather Mountain Formation suggest F_1 folds were formed, rotated, and tightened before the Tablerock thrust sheet arrived at its present location. This contrasts with Bryant and Reed's (1969, 1970) interpretation that NE/SW-trending open folds were rotated and flattened into SE/NW-trending tight and isoclinal folds. In their scenario, buckle folding and the rotation and tightening of fold hinges occurred contemporaneously as the Blue Ridge-Piedmont megathrust sheet was emplaced. However, F_2 and F_3 folds deform the S_1 foliation, and are never transected by it, indicating NE/SW-trending open, close, and gentle folds postdate the major phase of fabric development.

3. Deformation temperatures estimated from metamorphic mineral assemblages, quartz lattice-preferred orientations, dynamic recrystallization microstructures, feldspar deformation microstructures, and the opening angles of quartz [c]-axis fabrics indicate the Tablerock thrust sheet reached 550–595 °C during lower–middle amphibolite facies conditions, and was later overprinted by upper greenschist to lower amphibolite facies conditions at 465–550 °C. These estimates are at least 120 °C higher than all previously reported temperatures (e.g. Bryant & Reed 1969, 1970; Boyer 1978; Trupe 1997; Trupe et

al. 2004; Hatcher et al. 2006), and are consistent with a model in which the Tablerock thrust sheet was significantly deformed during coupled transport with the Blue Ridge-Piedmont megathrust sheet prior to being emplaced at its present location.

4. The preservation of ribbon grains in several samples and partially recrystallized quartz pebbles in sample TR002 suggests stages 1 and 2 of the proposed model occurred rapidly enough that rocks in the Tablerock thrust sheet were not completely recrystallized during the high temperature phase of deformation.

5. The Tablerock thrust sheet may be a small Type-F thrust sheet that was penetratively deformed by sheath folding during coupled transport with the Blue Ridge-Piedmont megathrust sheet prior to, and/or shortly after, being emplaced at its present location.

WORKS CITED

Ábalos, B., Puelles, P., Fernández-Armas, S. & Sarrionandia, F. (2011). EBSD microfabric study of pre-Cambrian deformations recorded in quartz pebbles from the Sierra de la Demanda (N Spain). Journal of Structural Geology, 33: 500–518.

Adams, M. & Su, Q. (1996). The nature and timing of deformation in the Beech Mountain thrust sheet between the Grandfather Mountain and Mountain City windows in the Blue Ridge of northwestern North Carolina. Journal of Geology, 104: 197–213.

Aleinikoff, J.N., Zartman, R.E., Walter, M., Rankin, D.W., Lyttle, P.T. & Burton, W.C. (1995). U-Pb ages of metarhyolites of the Catoctin and Mount Rogers Formations, central and southern Appalachians: Evidence for two pulses of Iapetan rifting. American Journal of Science, 295: 428–454.

Alsop, G.I. (1992). Progressive deformation and the rotation of contemporary fold axes in the Ballybofey Nappe, north-west Ireland. Geological Journal, 27: 271–283.

Alsop, G.I. & Carreras, J. (2007). The structural evolution of sheath folds: A case study from Cap de Creus. Journal of Structural Geology, 29: 1915–1930.

Alsop, G.I. & Holdsworth, R.E. (1999). Vergence and facing patterns in large-scale sheath folds. Journal of Structural Geology, 21: 1335–1349.

Alsop, G.I. & Holdsworth, R.E. (2002). The geometry and kinematics of flow perturbation folds. Tectonophysics, 350: 99–125.

Alsop, G.I. & Holdsworth, R.E. (2004a). The geometry and topology of natural sheath folds: A new tool for structural analysis. Journal of Structural Geology, 26: 1561–1589.

Alsop, G.I. & Holdsworth, R.E. (2004b). Shear zone folds: Records of flow perturbation or structural inheritance? Geological Society of London Special Publications, 224: 177–199.

Alsop, G.I. & Holdsworth, R.E. (2006). Sheath folds as discriminators of bulk strain type. Journal of Structural Geology, 28: 1588–1606.

Alsop, G.I. & Holdsworth, R.E. (2012). The three dimensional shape and localisation of deformation within multilayer sheath folds. Journal of Structural Geology, 44: 110–128.

Alsop, G.I., Holdsworth, R.E. & McCaffrey, K.J.W. (2007). Scale invariant sheath folds in salt, sediments and shear zones. Journal of Structural Geology, 29: 1585–1604.

Azcárraga, J., Ábalos, B. & Ibarguchi, J. (2002). On the relationship between kilometer-scale sheath folds, ductile thrusts and minor structures in the basal high-pressure units of the Cabo Ortegal complex (NW Spain). Journal of Structural Geology, 24: 1971–1989.

Bailey, C.M., Francis, B.E. & Fahrney, E.E. (2004). Strain and vorticity analysis of transpressional high-strain zones from the Virginia Piedmont, USA. Geological Society Special Publication, 224: 249–264.

Behr, W.M. & Platt, J.P. (2011). A naturally constrained stress profile through the middle crust in an extensional terrane. Earth & Planetary Science Letters, 303: 181–192.

Boyer, S.E. (1978). Structure and origin of Grandfather Mountain Window, North Carolina. [Ph.D. thesis], Baltimore, MD: The Johns Hopkins University.

Boyer, S.E. (1984). Origin and significance of compositional layering in Late Precambrian sediments, Blue Ridge Province, North Carolina, U.S.A. Journal of Structural Geology,

Boyer, S.E. & Elliott, D. (1982). Thrust systems. American Association of Petroleum Geologists Bulletin, 66 (9): 1196–1230.

Bozdog, G.N., Cattanach, B.L. & Wooten, R.M. (2012). Recent road cut on U.S. 221 in McDowell County, NC reveals a new exposure of the Linville Falls fault. Geological Society of America Abstracts with Programs, 44 (4): 71.

Bryant, B. & Reed, J.C. (1962). Structural and metamorphic history of the Grandfather Mountain area, North Carolina: A preliminary report. American Journal of Science, 260: 161–180.

Bryant, B. & Reed, J.C. (1969). Significance of lineation and minor folds near major thrust faults in the southern Appalachians and the British and Norwegian Caledonides. Geological Magazine, 106 (5): 412–429.

Bryant, B. & Reed, J.C. (1970). Geology of the Grandfather Mountain window and vicinity, North Carolina and Tennessee. Geological Survey Professional Paper 615.

Butler, J.R. (1973). Paleozoic deformation and metamorphism in part of the Blue Ridge thrust sheet, North Carolina. American Journal of Science, 271-A: 72–88.

Byrd, W.J. (1973). Petrology of the Cambrian Shady Dolomite in North Carolina, northeast Tennessee, and southwest Virginia. Dissertation [Ph.D. thesis], Chapel Hill, NC: University of North Carolina at Chapel Hill.

Carreras, J., Druguet, E. & Griera, A. (2005). Shear zone-related folds. Journal of Structural Geology, 27: 1229–1251.

Cobbold, P.R. & Quinquis, H. (1980). Development of sheath folds in shear regimes. Journal of Structural Geology, 2: 119–126.

Cook, S.J., Swift, D.A., Graham, D.J. & Midgley, M.G. (2011). Origin and significance of 'dispersed facies' basal ice: Svínafellsjökull, Iceland. Journal of Glaciology, 57: 710–720.

Cudzil, M.R. & Driese, S.G. (1987). Fluvial, tidal, and storm sedimentation in the Chilhowee Group (Lower Cambrian), northeastern Tennessee, U.S.A. Sedimentology, 34: 861–883.

D'Agostino, J.P., Whitlow, J.W., Gazdik, G.C. & Harrison, D.K. (1983). Mineral resource potential of the Linville Gorge Wilderness and proposed extensions, Burke and McDowell Counties, North Carolina. United States Geological Survey Map Pamphlet MF-1610-B.

Deer, W.A., Howie, R.A. & Zussman, J. (1992). An Introduction to the Rock-Forming Minerals, 2nd Edition. Prentice Hall: New York.

Escher, A. & Watterson, J. (1974). Stretching fabrics, folds, and crustal shortening. Tectonophysics, 22: 223–231.

Exner, U. & Dabrowski, M. (2010). Monoclinic and triclinic 3D flanking structures around elliptical cracks. Journal of Structural Geology, 32: 2009–2021.

Ez, V. (2000). When shearing is a cause of folding. Earth-Science Reviews, 51: 155–172.

Fetter, A.H. & Goldberg, S.A. (1995). Age and geochemical characteristics of bimodal magmatism in the Neoproterozoic Grandfather Mountain rift formation. Journal of Geology, 103: 313–326.

Fitz Gerald, J.D. & Stünitz, H. (1993). Deformation of granitoids at low metamorphic grade. I: Reactions and grain size reduction. Tectonophysics, 221: 269–297.

Foster, C.T., Jr. (1977). Mass transfer in sillimanite-bearing schists near Rangeley, Maine. American Mineralogist, 62: 727–746.

Georgieva, M., Cherneva, Z., Kolcheva, K., Sarov, S., Gerdjikov, I. & Voinova, E. (2002). P-T metamorphic path of sillimanite-bearing schists in an extensional shear zone, Central Rhodopes, Bulgaria. Geochemistry, Mineralogy, and Petrology, 39: 95–106.

Goldberg, S.A., Butler, J.R. & Mies, J.W. (1986). Subdivision of the Blue Ridge thrust complex, western North Carolina and adjacent Tennessee. Geological Society of America Abstracts with Programs, 18: 616–617.

Goldstein, A.G. (1988). Factors affecting the kinematic interpretation of asymmetric boudinage in shear zones. Journal of Structural Geology, 10: 707–715.

Goscombe, B.D., Passchier, C.W. & Hand, M. (2004). Boudinage classification: End-member boudin types and modified boudin structures. Journal of Structural Geology, 26: 739–763.

Gosh, S.K. & Sengupta, S. (1999). Boudinage and composite boudinage in superposed deformations and syntectonic migmatization. Journal of Structural Geology, 21: 97–110.

Hatcher, R.D. Jr. (1978). Tectonics of the western Piedmont and Blue Ridge, southern Appalachians: Review and speculation. American Journal of Science, 278: 276–304.

Hatcher, R.D. Jr. (1991). Tectonic setting of the southern Appalachians. In: Southern Appalachian Windows: Comparison of Styles, Scales, Geometry, and Detachment Levels of Thrust Faults in the Foreland and Internides of a Thrust-Dominated Orogen. Intercontinental Geological Congress Field Trip Guidebook T167. American Geophysical Union: Washington, D.C.

Hatcher, R.D., Jr. (2002a). An Inner Piedmont primer. In: Hatcher, R.D., Jr. & Bream, B.R., eds., Inner Piedmont tectonics focused mostly on detailed studies in the South Mountains and the southern Brushy Mountains, North Carolina. Carolina Geological Society Guidebook, North Carolina Geological Survey: 1–18.

Hatcher, R.D. Jr. (2002b). Alleghanian (Appalachian) orogeny, a product of zipper tectonics: Rotational transpressive continent-continent collision and closing of ancient oceans along irregular margins. Geological Society of America Special Paper 364: 199–208.

Hatcher, R.D. Jr. (2004a). Southern Appalachian crustal transect – Day 1: Transect from Laurentian rifted margin to suspect terranes and the upper crust to lower middle crust, SE TN, western NC Blue Ridge: Ordovician greenschist to granulite facies Barrovian metamorphism. 17th International Basement Tectonics Association Field Trip Guidebook: 13–28.

Hatcher, R.D. Jr. (2004b). Properties of thrusts and upper bounds for the size of thrust sheets. In: McClay, K.R., eds., Thrust tectonics and hydrocarbon systems: American Association of Petroleum Geologists Memoir 82: 18–29.

Hatcher, R.D. Jr. (2010). The Appalachian orogen: A brief summary. In: Tollo, P., Bartholomew, M.J., Hibbard, J.P. & Karabinos, P.M., eds., From Rodinia to Pangea: The Lithotectonic Record of the Appalachian Region. Geological Society of America Memoir 206: 1–19.

Hatcher, R.D. Jr., Bream, B.R. & Merschat, A.J. (2007a). Tectonic map of the southern and central Appalachians: A tale of three orogens and a complete Wilson cycle. Geological Society of America Memoir 200: 1–38.

Hatcher, R.D. Jr., Lemiszki, P.J. & Whisner, J.B. (2007b). Character of rigid boundaries and internal deformation of the southern Appalachian foreland fold-thrust belt. GSA Special Paper 433: 243–276.

Hatcher, R.D., Jr. & Hooper, R.J. (1992). Evolution of crystalline thrust sheets in the internal parts of mountain chains. In: McClay, K.R., eds., Thrust Tectonics. London: Chapman & Hall: 217–234.

Hatcher, R.D. Jr., Merschat, A.J. & Raymond, L.A. (2006). Geotraverse: Geology of northeastern Tennessee and the Grandfather Mountain region. In: Labotka, T.C. & Hatcher, R.D. Jr., eds., Southeastern Section Meeting, Geological Society of America Field Trip Guidebook, 6: 129–184.

Hirth, G. & Tullis, J. (1992). Dislocation creep regimes in quartz aggregates. Journal of Structural Geology, 14: 145–159.

Hull, D. & Bacon, D.J. (2011). Introduction to Dislocations, 5th edition. Elsevier Science: Oxford.

Humphreys, F.J. & Hatherly, M. (2004). Recrystallization and Related Annealing Phenomena. Elsevier Science: Oxford.

Jiang, D. & Williams, P.F. (1999). When do dragfolds not develop into sheath folds in shear zones? Journal of Structural Geology, 21: 577–583.

Karato, S.I. (2008). Deformation of Earth Materials: An Introduction to the Rheology of Solid Earth. Cambridge University Press: New York.

King, P.B. & Ferguson, H.W. (1960). Geology of northeasternmost Tennessee. Geological Survey Professional Paper 311.

Konstantinovskaya, E. & Malavieille, J. (2011). Thrust wedges with décollement levels and syntectonic erosion: A view from analog models. Tectonophysics, 502: 336–350.

Kruhl, J.H. (1996). Prism- and basal-plane parallel subgrain boundaries in quartz: A microstructural geothermometer. Journal of Metamorphic Geology, 14: 581–589.

Kruhl, J.H. (1998). Reply: Prism- and basal-plane parallel subgrain boundaries in quartz: A microstructural geothermometer. Journal of Metamorphic Geology, 16: 142–146.

Langille, J.M., Lee, J., Hacker, B. & Seward, G. (2010a). Middle crustal ductile deformation patterns in southern Tibet: Insights from vorticity studies in Mabja Dome. Journal of Structural Geology, 32: 70–85.

Langille, J.M., Jessup, M.J., Cottle, J.M., Newell, D. & Seward, G. (2010b). Kinematic evolution of the Ama Drime detachment: Insights into orogen-parallel extension and exhumation of the Ama Drime Massif, Tibet–Nepal. Journal of Structural Geology, 32: 900–919.

Law, R.D., Schmid, S.M. & Wheeler, J. (1990). Simple shear deformation and quartz crystallographic fabrics: A possible natural example from the Torridon area of NW Scotland. Journal of Structural Geology, 12: 29–45.

Law, R.D., Searle, M.P. & Simpson, R.L. (2004). Strain, deformation temperatures and vorticity of flow at the top of the Greater Himalayan Slab, Everest Massif, Tibet. Journal of the Geological Society, 161: 305–320.

Mack, G.H. (1980). Stratigraphy and depositional environments of the Chilhowee Group (Cambrian) in Georgia and Alabama. American Journal of Science, 280: 497–517.

Mandal, N., Mitra, A.K., Sarkar, S. & Chakraborty, C. (2009). Numerical estimation of the initial hinge-line irregularity required for the development of sheath folds: A pure shear model. Journal of Structural Geology, 31: 1161–1173.

Marques, F.G. & Cobbold, P.R. (1995). Development of highly non-cylindrical folds around rigid ellipsoidal inclusions in bulk simple shear regimes: Natural examples and experimental modelling. Journal of Structural Geology, 17: 589–602.

Marques, F.O., Guerreiro, S.M. & Fernandes, A.R. (2008). Sheath fold development with viscosity contrast: Analogue experiments in bulk simple shear. Journal of Structural Geology, 30:1348–1353.

Mies, J.W. (1991). Planar dispersion of folds in ductile shear zones and kinematic interpretation of fold-hinge girdles. Journal of Structural Geology, 13: 281–297.

Mies, J.W. (1993). Structural analysis of sheath folds in the Sylacauga Marble Group, Talladega slate belt, southern Appalachians. Journal of Structural Geology, 15: 983–993.

Mitra, G. & Boyer, S.E. (1986). Energy balance and deformation mechanisms of duplexes. Journal of Structural Geology, 8: 291–304.

Morales, L.F.G., Casey, M., Lloyd, G.E. & Williams, D.M. (2011). Kinematic and temporal relationships between parallel fold hinge lines and stretching lineations: A microstructural and crystallographic preferred orientation approach. Tectonophysics, 503: 207–221.

Musumeci, G. (2002). Sillimanite-bearing shear zones in syntectonic leucogranite: Fluid-assisted brittle-ductile deformation under amphibolite facies conditions. Journal of Structural Geology, 24: 1491–1505.

Neton, M.J. (1992). Late Proterozoic rifting of Laurentia: Source and deposition of conglomerate units of the Grandfather Mountain Formation, North Carolina Blue Ridge. [M.S. thesis], Knoxville, TN: The University of Tennessee.

Nicolas, A. (1987). Principles of Rock Deformation. Reidel Publishing: Dordrecht.

Platt, J.P. & Behr, W.M. (2011a). Grainsize evolution in ductile shear zones: Implications for strain localization and the strength of the lithosphere. Journal of Structural Geology, 33: 537–550.

Platt, J.P. & Behr, W.M. (2011b). Lithospheric shear zones as constant stress experiments. Geology, 39: 127–130.

Platt, J.P. & Behrmann, J.H. (1986). Structures and fabrics in a crustal scale shear zone, Betic Cordillera, SE Spain. Journal of Structural Geology, 8: 15–34.

Pryer, L.L. (1993). Microstructures in feldspars from a major crustal thrust zone: The Grenville Front, Ontario, Canada. Journal of Structural Geology, 15: 21–36.

Reber, J.E., Dabrowski, M. & Schmid, D.W. (2012). Sheath fold formation around slip surfaces. Terra Nova, 24 (5): 417–421.

Reber, J.E., Galland, O., Cobbold, P.R. & Le Carlier de Veslud, C. (2013a). Experimental study of sheath fold development around a weak inclusion in a mechanically layered matrix. Tectonophysics 586: 130–144.

Reber, J.E., Dabrowski, M., Galland, O. & Schmid, D.W. (2013b). Sheath fold morphology in simple shear. Journal of Structural Geology, 53: 15–26.

Reed, J.C. (1964). Geology of the Linville Falls quadrangle North Carolina. Geological Survey Bulletin, 1161–B.

Rosas, F., Marques, F.O., Luz, A. & Coelho, S. (2002). Sheath folds formed by drag induced by rotation of rigid inclusions in viscous simple shear flow: Nature and experiment. Journal of Structural Geology, 24: 45–55.

Schwab, F.L. (1977). Grandfather Mountain Formation: Depositional environment, provenance, and tectonic setting of Late Precambrian alluvium in the Blue Ridge of North Carolina. Journal of Sedimentary Petrology, 47: 800–810.

Searle, M.P. & Alsop, G.I. (2007). Eye-to-eye with a mega-sheath fold: A case study from Wadi Mayha, northern Oman Mountains. Geology, 35: 1043–1046.

Simpson, E.L. & Sundberg, F.A. (1987). Early Cambrian age for synrift deposits of the Chilhowee Group of southwestern Virginia. Geology, 15: 123–126.

Singleton, J.S. & Mosher, S. (2012). Mylonitization in the lower plate of the Buckskin-Rawhide detachment fault, west-central Arizona: Implications for the geometric evolution of metamorphic core complexes. Journal of Structural Geology, 39: 180–198.

Skjernaa, L. (1989). Tubular folds and sheath folds: Definitions and conceptual models for their development, with examples from the Grapesvare area, northern Sweden. Journal of Structural Geology, 11: 689–703.

Stipp, M., Stünitz, H., Heilbronner, R. & Schmid, S.M. (2002). The eastern Tonale fault zone: A 'natural laboratory' for crystal plastic deformation of quartz over a temperature range from 250 to 700 °C. Journal of Structural Geology, 24: 1861–1884.

Stipp, M., Tullis, J., Scherwath, M. & Behrmann, J.H. (2010). A new perspective on paleopiezometry: Dynamic recrystallized grain size distributions indicate mechanism changes. Geology, 38: 759–762.

Sullivan, W.A. (2013). L-tectonites. Journal of Structural Geology, 50: 161–175.

Trupe, C.H. (1997). Deformation and metamorphism in part of the Blue Ridge thrust complex, northwestern North Carolina. [Ph.D. thesis], Chapel Hill, NC: The University of North Carolina.

Trupe, C.H., Stewart, K.G., Adams, M.G., Water, C.L., Miller, B.V. & Hewitt, L.K. (2003). The Burnsville fault: Evidence for the timing and kinematics of southern Appalachian Acadian dextral transform tectonics. Geological Society of America Bulletin, 115: 1365–1376.

Trupe, C.H., Stewart, K.G., Adams, M.G. & Foudy, J.P. (2004). Deciphering the Grenville of the southern Appalachians through evaluation of the post-Grenville tectonic history in northwestern North Carolina. Geological Society of America Memoir, 197: 679–695.

Tullis, J. (2002). Deformation of granitic rocks: Experimental studies and natural examples. In: Karato, S. & Wenk, H., eds., Plastic Deformation of Minerals and Rocks, Reviews in Mineralogy and Geochemistry, 51: 51–95.

Tullis, J. & Yund, R.A. (1987). Transition from cataclastic flow to dislocation creep of feldspar: Mechanisms and microstructures. Geology, 15: 606–609.

Tullis, J. & Yund, R.A. (1991). Diffusion creep in feldspar aggregates: Experimental evidence. Journal of Structural Geology, 14: 987–1000.

Twiss, R.J. & Moores, E.M. (1992). Structural Geology, 2nd edition. Freeman: New York, 532 p.

Vernon, R.H. (1979). Formation of late sillimanite by hydrogen metasomatism (base-leaching) in some high-grade gneisses. Lithos, 12: 143–152.

Vernon, R.H. (2004). A practical guide to rock microstructure. Cambridge University Press.

Viola, G. & Mancktelow, N.S. (2005). From XY tracking to buckling: Axial plane cleavage fanning and folding during progressive deformation. Journal of Structural Geology, 27: 409–417.

Vollmer, F.W. (1988). A computer model of sheath-nappes formed during crustal shear in the Western Gneiss Region, central Norwegian Caledonides. Journal of Structural Geology, 10: 735–743.

Walker, A.E. & Hatcher, R.D., Jr. (2012a). Was the Tablerock thrust sheet deformed by sheath folding? Geological Society of America Abstracts with Programs – Southeast section, 44 (4): 82.

Walker, A.E. & Hatcher, R.D., Jr. (2012b). Structural analysis of the Tablerock thrust sheet, Grandfather Mountain window, northwestern North Carolina: Emplacement kinematics of a large horse in a major thrust system. Geological Society of America Abstracts with Programs, 44 (7): 483.

Walker, D. & Driese, S.G. (1991). Constraints on the position of the Precambrian–Cambrian boundary in the southern Appalachians. American Journal of Science, 291: 258–283.

Whisonant, R.C. (1974). Petrology of the Chilhowee Group (Cambrian and Cambrian(?)) in central-eastern and southern Tennessee. Journal of Sedimentary Petrology, 44: 228–241.

Wilkins, R.L. (1966). Stratigraphy and structure of the Shady Dolomite, Linville Falls region, northern McDowell County, North Carolina. [M.S. thesis], Raleigh, NC: North Carolina State University.

Xypolias, P. (2009). Some new aspects of kinematic vorticity analysis in naturally deformed quartzites. Journal of Structural Geology, 31: 3–10.

Xypolias, P. (2010). Vorticity analysis in shear zones: A review of methods and applications. Journal of Structural Geology, 32: 2072–2092.

APPENDIX

Table A-1.1: Index of station numbers and locations

Station	Unit	Latitude (°N)	Longitude (°W)	Location
001	Ycg	35 47.735	-82 01.547	American Thread Rd.
002	€cu	35 49.286	-82 00.563	Old Linville Rd., North Cove
003	€cu	35 51.516	-81 57.422	Railroad crossing, Old Linville Rd., North Cove
004	€cl	35 50.099	-81 58.030	Old Linville Rd., North Cove
005	€cu	35.865588	-81.914685	Kistler Memorial Hwy., LGWA
006	€cl	35.972711	-81.918914	NC-183, Newland
007	€cl	35.972874	-81.914640	Joe Bowman Ave., Newland
008	*no data*	N/A	N/A	N/A
009	€cu	35.858828	-81.956909	~100m NE from 003
010	€cu	35.858828	-81.956909	~100m NE from 003
011	€cu	35.914218	-81.939106	US-221, near Linville Caverns, Marion
012	€cu	35.913719	-81.939585	US-221, near Linville Caverns, Marion
013	€cl	35.973881	-81.912162	Indian Rock Trail; off of Joe Bowman Ave.
014	€cl	35.974878	-81.915256	Dogwood Knob Rd., Newland
015	€cu	35.966144	-81.927531	NC-183, Newland
016	€cl	35.947599	-81.894391	Gingercake Rd. (FS-210), Newland
017	€cl	35.946429	-81.896095	Martin Rd., Newland
018	€cl	35.971013	-81.920148	address 7999, NC-183; near Joe Bowman Ave.
019	€cu	35.963465	-81.929949	under the NC-183 overpass; below Midway overlook
020	€cu	N/A	N/A	part way up Dobson Knob
021	€cu	35.811285	-81.991704	Dobson Knob, North Cove
022	€cu	35.970341	-81.931397	River Bend overlook, Blue Ridge Parkway
023	€cu	35.969302	-81.929447	Midway overlook, Blue Ridge Parkway
024	€cu	35.952347	-81.923769	Plunge Basin trail, Blue Ridge Parkway
025	€cu	35.952347	-81.923769	Plunge Basin trail, Blue Ridge Parkway
026	€cu	35.952347	-81.923769	Plunge Basin trail, Blue Ridge Parkway
027	€cu	35.952347	-81.923769	Plunge Basin trail, Blue Ridge Parkway
028	€cu	35.949855	-81.924489	Plunge Basin trail, Blue Ridge Parkway
029	€cu	35.94987	-81.92694	Upper Falls overlook, Blue Ridge Parkway
030	€cu	35.97189	-81.93188	Linville Falls Spur Rd., Blue Ridge Parkway
031	€cu	35.95421	-81.92808	Linville Falls visitor center, Blue Ridge Parkway
032	€cu	35.94992	-81.92747	Linville Falls fault type locality; Upper Falls overlook
033	€cu	35.94992	-81.92747	~100m north of 032, toward uppermost waterfall
034	€cu	35.94992	-81.92747	Upper Falls overlook, Blue Ridge Parkway
035	Ycg	35.96983	-81.94257	Linville Falls Spur Rd., Blue Ridge Parkway
036	€cl	35.97809	-81.91891	Camp Creek bridge, Blue Ridge Parkway
037	€cl	35.97809	-81.91891	~200m east from 036
038	€cl	35.97809	-81.91891	~100m east from 037
039	€cl	35.88899	-81.88604	Tablerock Mountain, LGWA
040	€cl	35.88913	-81.88684	Tablerock Mountain, LGWA
041	€cl	35.89165	-81.88320	Tablerock Mountain, LGWA
042	€cl	35.89165	-81.88320	Tablerock Mountain, LGWA
043	€s	35.82461	-82.01039	US-221, North Cove
044	Ywc	35.704489	-82.069539	Lake Tahoma Rd., Marion
045	Ywc	35.704355	-82.069954	Lake Tahoma Rd., Marion

Table A-1.1: Index of station numbers and locations, continued

Station	Unit	Latitude (°N)	Longitude (°W)	Location
046	Ywc	35.719249	-82.071541	Toms Creek Rd., Marion
047	Ywc	35.724677	-82.070919	Toms Creek Rd., Marion
048	€cu	35.726621	-82.036903	Cross Creek Rd., Marion
049	€cu	35.728972	-82.038082	Cross Creek Rd., Marion
050	€s	35.821521	-82.012041	US-221, south of 043
051	Ycg	35.914480	-81.953925	English Rd., Marion
052	Ywc	N/A	N/A	N/A
053	Ywc	35.757558	-82.041143	Hicks Chapel Loop, Marion
054	€cl	35.757558	-82.041143	Hicks Chapel Loop, Marion
055	€cu	35.728820	-82.038942	Cross Creek Rd., Marion
056	€cu	35.729165	-82.039658	Cross Creek Rd., Marion
057	€cu	35.745870	-82.047476	Appalachian Stone Co. quarry, US-221
058	€cl	35.756552	-82.037748	Hicks Chapel Loop, Marion
059	€cl	35.767054	-82.038936	Bald Mountain trail (FS-105), Marion
060	€cu	35.765717	-82.034773	Bald Mountain trail (FS-105), Marion
061	€cl	35.763324	-82.033528	Bald Mountain trail (FS-105), Marion
062	Tu	35.732591	-82.007403	Hankins Rd., Marion
063	Tu	35.743806	-81.979865	Hankins Rd., Marion
064	€cp	35.798416	-81.927151	Kistler Memorial Hwy., LGWA
065	€cu	35.799719	-81.931007	Kistler Memorial Hwy., LGWA
066	€cu	35.802674	-81.935453	Kistler Memorial Hwy., LGWA
067	€cp	35.804430	-81.935759	Kistler Memorial Hwy., LGWA
068	€cl	35.810171	-81.938768	Kistler Memorial Hwy., LGWA
069	€cl	35.817211	-81.935786	Kistler Memorial Hwy., LGWA
070	€cl	35.823557	-81.929787	Kistler Memorial Hwy., LGWA
071	€cl	35.828554	-81.928784	Kistler Memorial Hwy., LGWA
072	€cl	35.834299	-81.928808	Kistler Memorial Hwy., LGWA
073	€cu	35.835519	-81.941918	Kistler Memorial Hwy., LGWA
074	€cu	35.819286	-81.964307	Kistler Memorial Hwy., LGWA
075	€cu	35.820348	-81.974355	Kistler Memorial Hwy., LGWA
076	€s	35.781216	-82.037294	Woodlawan quarry, American Thread Rd.
077	€cl	35.947857	-81.896682	Martin Rd., Newland
078	€cl	35.947514	-81.896646	Martin Rd., Newland
079	€cl	35.945634	-81.896287	Martin Rd., Newland
080	€cl	35.927816	-81.889867	Sitting Bear Mountain, LGWA
081	€cl	35.927524	-81.889596	Sitting Bear Mountain, LGWA
082	€cu	35.938669	-81.928736	Kistler Memorial Hwy., LGWA
083	€cu	35.932145	-81.928748	Kistler Memorial Hwy., LGWA
084	€cu	35.931139	-81.928599	Kistler Memorial Hwy., LGWA
085	€cp	35.928076	-81.923928	Kistler Memorial Hwy., LGWA
086	€cp	35.928076	-81.923859	Cabin trail, LGWA
087	€cl	35.928722	-81.922517	Cabin trail, LGWA
088	€cl	35.928981	-81.921061	Cabin trail, LGWA
089	€cl	35.928978	-81.921061	Cabin trail, LGWA
090	€cu	35.924342	-81.923254	Kistler Memorial Hwy., LGWA

Table A-1.1: Index of station numbers and locations, continued

Station	Unit	Latitude (°N)	Longitude (°W)	Location
094	€cl	35.905293	-81.910263	Wiseman's View, LGWA
095	€cp	35.918121	-81.919499	Kistler Memorial Hwy., LGWA
096	€cl	35.910125	-81.913537	Kistler Memorial Hwy., LGWA
097	€cl	35.899053	-81.911475	Kistler Memorial Hwy., LGWA
098	€cl	35.897567	-81.911652	Kistler Memorial Hwy., LGWA
099	€cl	35.890250	-81.906628	Conley Cove trail (trailhead parking lot), LGWA
100	€cl	35.887965	-81.904650	Conley Cove trail, LGWA
101	€cl	35.888972	-81.903993	Conley Cove trail, LGWA
102	€cl	35.884150	-81.906112	Kistler Memorial Hwy., LGWA
103	€cu	35.865463	-81.914942	Kistler Memorial Hwy., LGWA
104	€cu	35.844570	-81.923342	Kistler Memorial Hwy., LGWA
105	€cp	35.844570	-81.926268	Kistler Memorial Hwy., LGWA
106	€cu	35.838948	-81.930200	Kistler Memorial Hwy., LGWA
107	€cp	35.837900	-81.929608	FS-106, LGWA
108	€cp	35.835587	-81.937860	FS-106, LGWA
109	€cu	35.829788	-81.946445	Kistler Memorial Hwy., LGWA
110	€cu	35.836193	-81.944395	Trail-308G, off of FS-106
111	€cl	35.850907	-81.910837	Pinch-In trail, LGWA
112	€cl	35.823632	-81.891286	Wolf Pit Rd., Shortoff Mountain, Pisgah National Forest
113	€cl	35.826501	-81.895784	Shortoff Mountain trail
114	€cl	35.829714	-81.898679	Shortoff Mountain trail
115	€cl	35.832785	-81.898429	Shortoff Mountain trail
116	€cl	35.832553	-81.902683	Shortoff Mountain trail
117	€cl	35.831207	-81.901728	Shortoff Mountain trail
118	€cl	35.829351	-81.900964	Shortoff Mountain trail
119	€cl	35.828426	-81.897372	Shortoff Mountain trail
120	€cl	35.827689	-81.894839	Shortoff Mountain trail
121	€cl	35.824684	-81.892390	Shortoff Mountain trail
122	Zgm	35.926983	-81.888805	Sitting Bear Mountain, LGWA
123	€cl	35.927459	-81.889053	Sitting Bear Mountain, LGWA
124	€cl	35.931292	-81.890439	Sitting Bear Mountain, LGWA

Map unit abbreviations:

€s	*Shady Dolomite*	Ybr	*Blowing Rock Gneiss*
€cu	*Chilhowee Group, upper quartzite unit*	Ycg	*Cranberry Gneiss, undivided*
€cp	*Chilhowee Group, blue phyllite unit*	Ywc	*Wilson Creek Gneiss, undivided*
€cl	*Chilhowee Group, lower quartzite unit*	Zbm	*Brown Mountain Granite*
Tu	*Tugaloo terrane, undivided*	Zgm	*Grandfather Mountain Formation, undivided*

Other abbreviations:

FR	*Forest Road*	LGWA	*Linville Gorge Wilderness Area*
FS	*Forest Service trail*	Mtn	*Mountain*
Hwy	*Highway*		

Note:

Kistler Memorial Hwy. is interchangeably called County Line Rd., Old NC-105, and Historical Wagon Trail Rd.

Table A-2: S_1 foliations

Station	strike	dip	Station	strike	dip	Station	strike	dip
003	119	27	036	214	21	077	029	19
006	225	20	037	226	24	079	070	29
006	070	10	037	220	55	080	015	18
007	176	12	038	270	11	080	015	18
009	320	65	038	105	20	082	153	12
013	150	13	041	56	20	083	057	56
013	015	20	042	103	36	083	030	35
013	340	20	042	030	34	084	078	29
013	048	24	043	270	23	085	005	11
013	022	19	044	050	41	085	192	13
013	165	25	045	055	44	086	214	70
016	220	40	045	205	06	086	010	56
017	084	27	046	062	43	086	035	41
017	150	40	047	166	18	087	284	12
021	155	45	048	080	50	088	014	25
022	195	12	048	145	42	089	083	24
022	130	16	049	080	46	090	035	15
023	150	33	049	245	32	092	185	16
023	245	55	049	085	26	092	060	04
023	225	70	050	270	20	094	161	23
023	225	30	051	178	13	095	020	43
023	165	26	051	190	25	096	100	10
023	100	15	051	200	20	096	058	14
024	200	14	052	060	34	096	070	39
025	170	31	053	175	32	097	105	08
025	200	34	054	110	34	098	116	18
026	160	28	055	348	09	099	085	12
026	060	90	056	050	68	100	086	18
027	190	38	056	086	46	101	100	22
028	172	27	057	119	40	102	284	11
028	225	21	058	070	23	104	055	17
028	080	32	058	095	28	105	225	30
029	115	03	059	165	31	106	055	27
029	205	14	060	033	19	107	248	31
029	310	11	061	030	24	108	126	08
029	270	36	062	076	21	110	205	06
029	225	24	063	360	52	111	046	14
030	300	18	064	123	21	112	038	43
030	285	25	065	087	23	113	047	22
030	235	80	066	067	12	114	020	49
032	200	22	067	105	28	115	335	18
032	260	25	068	110	13	116	020	14
032	248	21	068	213	14	117	166	21
033	215	24	071	155	23	117	052	09
033	205	24	072	166	09	118	060	12
033	190	25	073	083	10	121	050	30
035	123	26	074	270	24	122	055	22
035	135	25	075	073	14	124	063	06

Table A-3: L_1 mineral lineations

Station	trend	plunge	Station	trend	plunge	Station	trend	plunge
002	056	24	038	330	13	080	169	05
002	340	20	039	147	07	089	345	06
003	203	27	039	301	13	090	151	16
007	150	02	040	130	11	091	320	10
009	320	36	041	125	23	091	145	24
015	230	24	042	130	11	092	323	03
019	270	24	042	110	07	093	316	03
019	340	10	043	310	26	094	316	01
021	155	80	043	328	34	095	125	31
022	295	21	044	115	20	096	146	06
022	235	29	046	220	28	096	149	18
023	130	14	047	200	30	097	148	22
023	235	17	047	219	29	098	145	23
023	230	20	051	321	05	099	323	06
023	145	20	051	162	33	100	135	13
023	155	14	054	185	25	102	330	12
023	320	22	056	185	68	103	145	02
023	335	10	057	180	23	105	310	32
023	345	21	059	175	06	106	156	20
023	305	20	060	140	23	107	330	11
024	295	25	061	350	04	108	345	08
024	290	21	063	211	16	110	153	19
026	245	14	064	162	13	111	137	19
029	330	05	065	174	17	112	346	43
029	326	03	066	164	10	113	345	18
029	045	11	067	170	31	114	145	27
029	276	09	068	332	06	115	166	22
030	290	21	068	156	17	116	160	06
030	240	05	068	172	54	117	151	12
032	315	13	069	320	90	118	336	14
032	325	24	070	326	07	119	157	21
032	329	08	070	336	09	120	165	32
032	340	10	071	291	09	120	180	28
033	315	11	072	212	08	120	135	31
033	326	22	072	350	04	121	155	24
033	330	08	073	347	09	122	151	09
035	323	13	074	162	10	123	338	02
035	315	22	075	142	06	123	154	08
036	346	07	077	325	03	123	316	09
037	320	12	078	346	11	123	165	24
037	335	07	079	160	30	124	162	12
038	319	09	080	146	20	124	330	03

Table A-4: Crenulation hinge lines & interlimb angles

Station	trend	plunge	°ILA	Station	trend	plunge	°ILA
002	066	31		056	205	46	30
002	075	46		057	190	24	
002	056	24		062	210	16	75
007	210	06	20	070	045	23	65
007	056	45	110	071	032	32	55
007	054	45	115	077	205	10	20
013	145	16	10	078	226	23	23
013	062	16	20	079	230	24	
013	020	05	45	080	210	11	
013	292	15	30	082	238	24	
016	310	40		085	062	02	
022	325	20	150	086	186	23	105
023	230	21		087	052	01	
023	225	23		088	156	09	130
023	210	20		090	230	11	
024	300	34		091	235	11	40
025	220	31		092	036	04	
026	215	15	15	093	155	28	10
026	220	18		094	260	26	20
028	220	12	15	095	210	22	50
028	040	05	35	095	210	22	30
029	205	01		096	225	21	
029	235	06		097	210	14	
029	038	09		098	220	13	150
029	050	12	25	099	214	07	
029	232	10	25	100	220	01	
032	230	14	20	101	214	20	30
032	220	09		102	013	16	50
032	225	04		103	224	14	75
032	229	07		104	044	03	
033	226	10	150	105	224	07	
033	220	08	150	106	145	03	
033	050	06	46	108	215	10	
033	220	10	145	109	175	11	
036	040	11	125	111	140	24	150
037	210	15		120	125	18	10
037	221	08		122	210	12	
038	216	17	135	123	223	21	45
038	206	11		123	220	18	15
042	016	36					
051	070	09	80				
053	010	15	25				

Table A-5: Fold hinge lines, axial surfaces, and interlimb angles

	hinge lines		axial surfaces				hinge lines		axial surfaces		
Station	trend	plunge	strike	dip	°ILA	Station	trend	plunge	strike	dip	°ILA
001	016	06	028	37	90	039	128	06			15
003	232	10			75	039	249	16	070	35	15
003	291	13			10	040	097	14	124	22	25
003	302	13	286	46	80	040	097	14	304	22	30
004	247	11	249	33	80	041	140	36			55
005	210	15			40	042	110	07			25
007	048	32	223	46	145	042	125	22			20
007	054	45	230	52	115	042	130	20			20
007	056	45	250	64	110	043	328	30	328	02	20
007	169	15			20	046	110	67	070	54	25
007	198	30	224	64	140	046	110	44	125	30	23
007	212	23			145	046	171	34	095	13	26
010	090	30			90	049	110	24	080	37	40
013	164	16	330	15	30	050	158	25			15
013	200	20			30	050	330	30			10
013	315	21	040	22	10	051	256	27	080	56	80
013	328	21	185	19	20	051	279	22	106	34	35
013	330	12	030	25	20	051	328	09	106	49	28
013	330	12	190	30	20	052	330	09	115	20	20
013	330	10			15	052	330	43	310	26	55
015	203	16			80	052	330	43			25
022	265	24	085	78	150	053	284	22	323	16	25
023	226	30	336	44	95	054	165	19			30
026	163	25			25	056	240	60			30
026	205	22	130	23	15	058	140	21	125	31	24
028	246	20	086	16	35	058	190	24			24
029	125	29			20	058	202	18			20
029	131	18	065	20	20	059	200	24	200	48	28
029	220	09			25	062	345	11	008	39	75
029	230	01			25	063	215	18	065	33	40
032	230	14	050	80	130	064	161	09	341	86	5
032	330	10			20	066	160	24	336	36	15
033	050	06	050	70	46	068	213	14	049	33	10
033	220	10	040	75	145	068	263	24	074	81	80
033	220	08	040	86	150	068	306	21	063	44	10
033	226	10	045	78	150	068	320	21			23
034	205	10	030	34	105	069	320	90	007	44	10
034	210	07	030	15	105	070	213	12	026	59	65
034	222	21	222	40	110	071	250	24			20
036	012	20	012	51	150	071	266	42	083	63	35
036	015	24	205	57	130	071	324	45	345	60	45
036	342	19	345	54	125	072	252	23	257	88	125
038	337	19	155	37	135	072	280	30	055	51	140

Table A-5: Fold hinge lines, axial surfaces, and interlimb angles, continued

	hinge lines		axial surfaces				hinge lines		axial surfaces		
Station	trend	plunge	strike	dip	°ILA	Station	trend	plunge	strike	dip	°ILA
072	295	27	157	87	20	117	194	15			45
072	320	40	096	50	20	118	340	08	195	35	10
073	215	8	245	41	25	119	157	21	195	35	10
077	354	11	144	30	20	120	160	22			10
078	043	11	045	45	23	123	127	10			15
078	350	30	159	24	25	123	168	08	357	36	45
080	169	05			20	123	175	16			15
081	130	07			30	123	240	36	240	61	50
083	240	36	049	50	20	124	145	28			10
084	144	22			15	124	240	09			170
086	140	35	041	36	35						
086	259	43	059	37	105						
086	330	35	155	39	25						
088	040	32			130						
090	067	08			140						
090	240	13			85						
090	331	16			20						
090	355	19			20						
091	230	35			40						
091	240	34			45						
091	300	36			20						
092	332	18			10						
093	146	36	146	24	10						
094	325	26	325	43	20						
095	061	30	056	51	70						
095	200	36	055	61	55						
095	205	37	041	45	50						
095	210	22			30						
096	160	29			15						
096	218	21	060	37	105						
096	241	21			85						
097	156	20			15						
098	241	21	036	46	150						
101	155	34	193	52	30						
102	057	31			50						
103	070	14			75						
107	315	16	168	60	20						
111	103	16			150						
112	071	22			100						
112	325	37			20						
114	143	37	010	26	15						
116	346	01	003	15	10						

VITA

Annie Walker was born in Charleston, South Carolina and raised in Liverpool and Rochester, New York. She is a 2008 graduate of Le Moyne College, where she earned a Bachelor of Science degree in Earth Systems Science and double minors in Biology and Chemistry. While at Le Moyne, she spent three field seasons studying pedogenesis of andic cryofluvients on recently exposed proglacial plains in southern Iceland, and one field season assisting an ongoing study of insect population recovery following hurricanes on San Salvador Island, Bahamas. During her final year at Le Moyne, Annie had the great opportunity to assist Dr. Lawrence H. Tanner in his research of iridium anomalies concentrated in Triassic–Jurassic boundary sediments of the Blomidon Formation, Fundy basin, Nova Scotia. Annie began her M.S. research with Dr. Hatcher at the University of Tennessee in December 2011; in June 2013, she accepted a position modeling basins with ION GeoVentures in Houston, Texas, where she now happily resides.